

# Design, manufacturing and experimental testing of a mechanical exit port mechanism for a solar reactor

**Joppe RUTTEN**  
**Jens VERSCHOREN**

Promotor(en): Prof. dr. ir. David Moens

Co-promotor(en): Prof. dr. ir. Nesrin Ozalp  
Ing. Cédric Ophoff

Masterproef ingediend tot het behalen van  
de graad van master of Science in de  
industriële wetenschappen: Elektromechanica  
optie Automotive Engineering

Academiejaar 2017 - 2018





©Copyright KU Leuven

Zonder voorafgaande schriftelijke toestemming van zowel de promotor(en) als de auteur(s) is overnemen, kopiëren, gebruiken of realiseren van deze uitgave of gedeelten ervan verboden. Voor aanvragen i.v.m. het overnemen en/of gebruik en/of realisatie van gedeelten uit deze publicatie, kan u zich richten tot KU Leuven Technologicampus De Nayer, Jan De Nayerlaan 5, B-2860 Sint-Katelijne-Waver, +32 15 31 69 44 of via e-mail [iw.denayer@kuleuven.be](mailto:iw.denayer@kuleuven.be).

Voorafgaande schriftelijke toestemming van de promotor(en) is eveneens vereist voor het aanwenden van de in deze masterproef beschreven (originele) methoden, producten, schakelingen en programma's voor industrieel of commercieel nut en voor de inzending van deze publicatie ter deelname aan wetenschappelijke prijzen of wedstrijden.



# Preface

We live in a world that is built around heavy reliance on energy by many sectors ranging from industrial to residential. The primary source of present energy conversion systems is fossil fuel based which has a negative environmental impact. Therefore, alternative and sustainable energy conversion technologies are essential. There have been many research groups searching for sustainable solutions that can provide clean alternatives to fossil fuels. One of the most promising alternative fuels is hydrogen which has a higher calorific value than presently used fossil fuels and would not emit hazardous gases like fossil fuel combustion. However, hydrogen is not readily available in nature like fossil fuels. It needs to be extracted from a feedstock which is mainly either water or natural gas. Extraction of hydrogen from water or natural gas has both challenges of their own. This thesis research focuses on hydrogen extraction from natural gas. As for the extraction method, a clean technology focusing on solar energy is selected to eliminate environmental concerns. Therefore, this thesis works on the challenges of hydrogen production method via natural gas cracking using solar energy with particular focus on solving the carbon clogging of the reactor.

There are some people that definitely deserve our gratitude. First of all, we would like to thank our Promotors Prof. Dr. Nesrin Ozalp and Prof. Dr. David Moens to give us the opportunity to work in this research team and try to make a change in the world by developing a new technology for clean energy. We are honoured to be able to work in such an important field of research and make our contribution. Prof. Dr. Nesrin Ozalp provided us close guidance for our research and helped us all the way to the finish line. She constantly gave us constructive feedback which pushed us to do even better and go even further. Her knowledge on the thermodynamic aspect was indispensable. Her enthusiasm and passion in this work have inspired and motivated us to give it our very best.

We are also very thankful to Prof. Dr. David Moens who guided us through our thesis and helped us in every way possible. With a thesis heavily focused on the mechanical aspect of engineering, we could not be happier with his knowledge and experience on this subject to complete our novel design.

Then we would like to thank to Ph.D. Researcher Cédric Ophoff extensively for his follow-up on a daily basis. He took his role as our mentor very seriously and was always ready to help us with problems or questions. We learned a lot from him in the field of thermodynamics, in the field of the

solar reactor, but also as engineers.

We would also like to thank Mr. Witse Volders. As the technician of the workshop at our Campus, he took his time to help us with the design process, the manufacturing of a great share of the parts of our mechanism, and the assembly of these parts.

Lastly, we would like to thank Ir. Ing. Julien Debontridder. He provided us with many Transmission Electron Microscope images that were very helpful in our thesis.

# Summary

In de volgende masterthesis *Design, manufacturing and experimental testing of a mechanical exit port mechanism for a solar reactor* wordt een ontwerp voorgesteld dat een oplossing vormt voor het probleem van het verstoppert van een zonnereactor door het neerslaan van koolstof. Het doel van deze thesis is om het volledig ontwerpproces te beschrijven en om te verduidelijken waarom bepaalde ontwerp keuzes zijn gemaakt.

De thesis start met een literatuurstudie waarbij eerst onderzoek wordt gedaan naar de algemene werking van het proces achter het thermisch kraken van methaan. Vervolgens wordt er dieper ingegaan op de aspecten van dit proces die belangrijk zijn om een werkend mechanisme te bekomen. Hierbij wordt onderzocht welke eigenschappen carbon black heeft en welke mechanismen verantwoordelijk zijn voor de neerslag ervan.

Aan de hand van deze literatuurstudie kunnen de ontwerp vereiste opgesteld worden die leiden tot het ontwikkelen van een concept. Dit concept zal in detail worden uitgelegd en verder ontwikkeld worden tot een functionerend mechanisme dat kan werken op de bestaande zonnereactor aanwezig in het STTL. Om de functionaliteit van het ontwerp zo goed mogelijk te voorspellen worden verschillende numerische analyses uitgevoerd. Hierbij wordt het last koppel berekend en wordt een statische krachtenanalyse, een dynamische trillingsanalyse en een analyse van de warmte overdracht van de koeling uitgevoerd. Technische tekeningen van de verschillende onderdelen werden doorgegeven aan de machine technicus zodat deze gemanufactured konden worden.

De experimentele fase wordt ingeleid door op zoek te gaan naar een alternatief poeder waarmee testen uitgevoerd kunnen worden zonder het werkelijk kraken van methaan. Ook wordt een testopstelling voorgesteld die het mogelijk maakt om te werking van het mechanisme te valideren.



# Abstract

## English

Solar thermal cracking of natural gas is a promising technology to produce hydrogen without damaging the environment. An added value of this process is the production of carbon black as the byproduct which is equally important for the industry. The basic principle of this process is simple: natural gas is fed into a solar reactor and concentrated solar energy heats up the natural gas to its decomposition temperature which produces hydrogen and carbon black. However, carbon black production during this process creates the major bottleneck for the commercialization of hydrogen production via solar thermal cracking method. The problem stems from carbon particles depositing at the exit port of the solar reactor. Once the solar reactor exit is completely blocked by the carbon particles, the pressure builds up inside the reactor and then the glass window of the reactor breaks which stops the production process.

In order to address the reactor clogging problem, this thesis focuses on a novel design to develop a mechanical cleaning mechanism at the exit port of the reactor. The design is compatible with the solar reactor at the Solar Thermal Technology Laboratory (STTL) at Campus De Nayer. The design features rotational motion of a scraper to provide the shear force required to overcome the particle-particle and particle-surface interactions which then removes the agglomerated carbon particles deposited at the exit port.

This thesis report covers the entire design process starting with the literature survey showing the works done in the field, followed by the novel design concept developed during the course of this thesis project, numerical analysis done to optimize the design concept, and finally the improvements made to the original concept. The thesis also covers the manufacturing of the design, and the experimental testing of the design.

**Keywords:** Solar reactor, Design, Carbon clogging, Mechanical cleaning, Motion analysis





---

## Nederlands

Het zonne-thermisch kraken van methaangas is een veelbelovende technologie die gebruikt kan worden voor de productie van waterstof zonder hiermee schadelijk te zijn voor het milieu. Een extra voordeel van dit proces is de productie van carbon black als bijproduct, wat even belangrijk is voor de industrie. Het algemeen principe van dit proces is eenvoudig: methaangas wordt gevoed aan een zonne-reactor waarin geconcentreerde zonne-energie het gas opwarmt tot zijn ontbindingstemperatuur om zo waterstof en carbon black te produceren. Hierbij zorgt de productie van carbon black wel voor een groot knelpunt om waterstofproductie via zonne-thermisch kraken van methaan te commercialiseren. Het probleem wordt veroorzaakt door het neerslaan van koolstof deeltjes aan de uitlaatpoort van de reactor. Zodra de uitlaat van de zonne-reactor volledig geblokkeerd is door koolstof deeltjes zal de druk in de reactor zodanig opbouwen dat het uiteindelijk zal leiden tot het breken van het glazen scherm wat het productieproces zal doen stoppen.

Om het probleem van het verstopping van reactor aan te pakken zal er in deze thesis gefocust worden op de ontwikkeling van een nieuw mechanisch schoonmaak mechanisme aan de uitlaatpoort van de reactor. Dit ontwerp moet compatibel zijn met de zonnereactor die aanwezig is in het Solar Thermal Technology Laboratory (STTL) op Campus De Nayer. Kenmerkend aan dit ontwerp is de rotatiebeweging van een schraper die een schuifspanning levert om zo de partikel-partikel en oppervlak-partikel interacties te overwinnen wat geagglomereerde koolstofdeeltjes die neerslaan aan de uitlaatpoort zal verwijderen.

Dit thesis verlag behandelt het volledige ontwerpproces startende met een literatuurstudie over wat hierover reeds bekend is, gevolgd door het nieuwe ontwerp dat ontwikkeld werd tijdens dit thesis project, numerische analyses uitgevoerd om het conceptueel ontwerp te verbeteren, en de verbeteringen die uitgevoerd werden op het originele ontwerp. Deze thesis behandelt ook de productie van het ontwerp, en het experimenteel testen van het ontwerp.

**Trefwoorden:** Zonnereactor, Ontwerp, Carbon clogging, Mechanisch schoonmaken, bewegingsanalyse



# Contents

<b>Preface</b>	<b>vi</b>
<b>Summary</b>	<b>vii</b>
<b>Abstract</b>	<b>xi</b>
<b>Contents</b>	<b>xv</b>
<b>List of Figures</b>	<b>xix</b>
<b>List of Tables</b>	<b>xxi</b>
<b>Nomenclature</b>	<b>xxiii</b>
<b>List of abbreviations</b>	<b>xxv</b>
<b>1 Introduction</b>	<b>1</b>
<b>2 Literature Review</b>	<b>5</b>
2.1 Carbon Black . . . . .	5
2.1.1 Commercial carbon black . . . . .	5
2.1.2 Carbon black from methane cracking . . . . .	7
2.2 Carbon Deposition . . . . .	8
2.2.1 Deposition mechanisms . . . . .	9
2.2.2 Adhesion to the surface . . . . .	11
2.2.3 Adhesion and aggregates of carbon black particles . . . . .	13
2.2.4 Exhaust clogging . . . . .	13
2.2.5 Deposit removal mechanisms . . . . .	14
2.2.6 Exhaust gas recirculation cooler . . . . .	15
2.2.7 Nanocoating . . . . .	17

---

<b>3</b>	<b>Design Methodology</b>	<b>19</b>
3.1	Constraints . . . . .	19
3.2	Preliminary design . . . . .	20
3.2.1	Exit port geometry . . . . .	20
3.2.2	Cleaning mechanism . . . . .	21
3.3	Design improvements . . . . .	22
3.3.1	Fixation of the scraper . . . . .	23
3.3.2	Exhaust cooling . . . . .	23
3.4	Motion mechanism . . . . .	25
3.4.1	Mechanical drive . . . . .	25
3.4.2	Magnetic drive . . . . .	27
3.4.3	Comparison . . . . .	30
3.5	Final Design . . . . .	32
<b>4</b>	<b>Numerical methodology</b>	<b>35</b>
4.1	Load torque analysis . . . . .	35
4.1.1	Tensile stress . . . . .	35
4.1.2	Torque . . . . .	36
4.2	Static analysis . . . . .	37
4.2.1	Governing equations . . . . .	37
4.2.2	Strategy . . . . .	38
4.2.3	Manual calculation . . . . .	39
4.2.4	Results of FEA . . . . .	40
4.3	Dynamic Analysis . . . . .	41
4.3.1	Governing equations . . . . .	41
4.3.2	Results . . . . .	41
4.4	Heat transfer analysis . . . . .	43
4.4.1	Strategy . . . . .	43
4.4.2	Governing equations . . . . .	44
4.4.3	Convective heat transfer coefficients . . . . .	48
4.4.4	Temperature dependent properties . . . . .	49
4.4.5	Results . . . . .	51
<b>5</b>	<b>Manufacturing</b>	<b>53</b>
5.1	Manufacturing of the parts . . . . .	53
5.2	Assembly of the mechanism . . . . .	60

---

<b>6</b>	<b>Experimental testing and results</b>	<b>63</b>
6.1	Powder selection . . . . .	63
6.2	Test set-up . . . . .	67
<b>7</b>	<b>Conclusion and future work</b>	<b>69</b>
<b>A</b>	<b>Technical drawings</b>	<b>77</b>
<b>B</b>	<b>Motor and reduction</b>	<b>89</b>
<b>C</b>	<b>Heat transfer analysis</b>	<b>93</b>
<b>D</b>	<b>Bill of Material (BOM)</b>	<b>105</b>
<b>E</b>	<b>Manufacturing and assembly</b>	<b>109</b>



# List of Figures

1.1	(a) steam reforming (b) solar reforming (c) solar cracking [1]	1
1.2	Solar reactor used to split methane in Hydrogen and solid Carbon using concentrated solar energy [2]	2
2.1	(a) Structure of graphite (b) Structure of carbon black [3]	6
2.2	Morphological structures of a nanoparticle of a commercial carbon black [4]	6
2.3	TEM images of commercial carbon black vs. solar carbon black [5]	8
2.4	Aero-shielded solar cyclone reactor [6]	9
2.5	(a) Cross-section of the first cyclic reactor [7] (b) cross-section of the second cyclic reactor using the natural tornado phenomenon [8]	10
2.6	Thermoforetic net force on a spherical particle	11
2.7	(a) Representation of the VDW potential energy for a spherical colloidal particle interacting with a flat surface (b) As a function of the particle-surface distance [9]	12
2.8	Schematic representation of cohesive powders containing spherical particles [10]	13
2.9	The complete process consists out of four phenomena [9]	14
2.10	Forces acting on a deposited particle in a fluid flow with $F_V$ the Van der Waals force, $F_W$ the weight force, $F_D$ the drag force and $F_L$ the lift force [11]	15
2.11	Condensate layer formed on the surface [12]	16
3.1	CAD-drawing of the preliminary design	20
3.2	Sketch of the conical shape with varying cross-sectional area	21
3.3	Scraper used to remove the deposited carbon black	22
3.4	Scraper used to remove the deposited carbon black	23
3.5	Wrapping of the exhaust with copper cooling channels	24
3.6	The joining parts with the bond	25
3.7	Schematic model of the magnetic drive (modified from [13])	28
3.8	Equivalent magnetic model circuit of the configuration shown in Figure 3.7	29
3.9	Simplified magnetic circuit	30

3.10	Overview of the design process evolution from preliminary design to final design . . .	32
3.11	Overview of the final design assembly with every component labelled . . . . .	33
4.1	Force $F$ exerted on the scraper surface at radius $r$ . . . . .	37
4.2	Resulting model that is used to perform the static analysis . . . . .	39
4.3	End constraints of the used beam model . . . . .	40
4.4	Results of the static analysis . . . . .	40
4.5	The mode-shapes at each of these modal frequencies . . . . .	42
4.6	(a) Complex spiral shape of the channels, (b) discretization to circular channels, (c) unfolding of these circular channels . . . . .	43
4.7	Schematic overview of the parameters used for each ring . . . . .	44
4.8	Heat transfer in a flat-plate solar collector (Modified from [14]) . . . . .	45
4.9	Results of a specific case using Matlab code . . . . .	52
5.1	Coordinate system of a 5-axis CNC milling machine . . . . .	53
5.2	Coordinate system of a CNC lathe machine . . . . .	54
5.3	Section view of backplate of the reactor . . . . .	55
5.4	Manufacturing process of the backplate . . . . .	55
5.5	Section view of the conical duct . . . . .	56
5.6	Milling process of the conical duct . . . . .	56
5.7	Turning process of the conical duct . . . . .	57
5.8	(a) Right hub: part of the cylindrical hub that has the opening for the belt, (b) left hub: part of the cylindrical hub that is connected to the conical duct . . . . .	57
5.9	Manufacturing process on the lathe of the housing . . . . .	58
5.10	Section view of the driven pipe . . . . .	58
5.11	Manufacturing process on the lathe of the driven pipe . . . . .	59
5.12	Milling proces of the scraper . . . . .	59
5.13	Connection welds between back-plate, conical duct and left hub . . . . .	60
5.14	Holder used to fixate the scraper to the driven pipe . . . . .	60
5.15	Different views of the manufactured assembly . . . . .	61
6.1	Electron microscope images of graphite . . . . .	65
6.2	Electron microscope images of vanilla powder . . . . .	66
6.3	Electron microscope images of sifted lactose . . . . .	67
6.4	Frontal view of the test set-up . . . . .	68
6.5	Test set-up . . . . .	68



---

7.1 Half-section view of the cleaning mechanism . . . . .	70
---	----



# List of Tables

2.1	Results of the Raman spectroscopy showing the level of graphitization of test specimen produced at different reactor temperatures compared to carbon black E250G. Modified from [5]	7
3.1	Comparison between the mechanical drive and magnetic drive	31
4.1	Physical properties of carbon black (modified from [15])	36
4.2	Material properties of AISI Type 316L Stainless Steel, annealed bar	39
4.3	Result of the dynamic analysis showing the first nine modes with their corresponding frequency	42
4.4	Temperature dependent thermal conductivities	50
4.5	Temperature dependent fluid properties	51
4.6	Design and geometry parameters for calculations	51
6.1	Summary of the observations from the initial test	64



# Nomenclature

Symbol	Use	SI-unit
<b>Lower case</b>		
$b$	Bond breath length	[m]
$c_p$	Specific heat	[J/(kgK)]
$d$	Diameter	[m]
$e$	Definitive axis distance	[m]
$e'$	Global axis distance	[m]
$f$	Frequency	[Hz]
$f$	Friction factor	[-]
$\{f\}$	Force vector	[-]
$h$	Convective heat transfer coefficient	[W/m <sup>2</sup> K]
$k$	Thermal conductivity	[W/(mK)]
$q$	Specific heat flux	[W/m <sup>2</sup> ]
$u$	Flow velocity	[m/s]
$u^*$	Friction velocity	[m/s]
$\{u\}$	Displacement vector	[-]
$\{\dot{u}\}$	Velocity vector	[-]
$\{\ddot{u}\}$	Acceleration vector	[-]
$\dot{x}$	Flow velocity	[m/s]
<b>Capitals</b>		
$A$	Cross-section area	[m <sup>2</sup> ]
$A_{D1}$	Area of D1 band	[m <sup>2</sup> ]
$A_G$	Area of G band	[m <sup>2</sup> ]
$A_H$	Hamakers constant	[J]
$B$	Flux density	[Wb/A]
$D$	Transient tube diameter	[m]
$F$	Fin efficiency factor	[-]
$F_D$	Drag force	[N]
$F_V$	Van der Waals force	[N]
$F_W$	Weigth force	[N]
$Gr$	Grashof number	[-]
$I_{D1}$	Peak intensity of D1 band	[-]

Symbol	Use	SI-unit
$I_G$	Peak intensity of G band	[-]
$K_l$	Leakage factor	[-]
$K_r$	Reluctance factor	[-]
$L_a$	Crystallinity length	[m]
$L_d$	Definitive belt length	[m]
$Nu$	Nusselt number	[-]
$P$	Permeance	[H]
$Pr$	Prandtl number	[-]
$\dot{Q}$	Heat flux	[W]
$R$	Reluctance	[H <sup>-1</sup> ]
$Ra$	Rayleigh number	[-]
$Re$	Reynolds number	[-]
$S$	Specific area	[m <sup>2</sup> /g]
$T$	Temperature	[K] or [°C]
$T$	Torque	[Nm]
$U_{cr, shear}$	Critical shear velocity	[m/s]
$U_L$	Heat transfer coefficient that describes heat losses	[W/m <sup>2</sup> K]
$\dot{V}$	Volumetric flow rate	[m <sup>3</sup> /s]
$W$	Energy required to separate 1 m <sup>2</sup> of adhering interface	[J/m <sup>2</sup> ]
$W$	Tube pitch	[m]
$X$	Conductive layer thickness	[m]
$Z_0$	Distance between particle and surface	[m]
<b>Greek lower case</b>		
$\alpha$ (alpha)	Scaling factor	[-]
$\beta$ (beta)	Coefficient of volumetric expansion	[1/K]
$\delta$ (delta)	Partial charge distribution	[-]
$\mu$ (mu)	Permeability	[H/m]
$\mu_g$	Dynamic gas viscosity	[kg/ms]
$\nu$ (nu)	Kinematic gas velocity	[m <sup>2</sup> /s]
$\rho_g$ (rho)	Density of the gas	[kg/m <sup>3</sup> ]
$\rho_p$	Particle density	[kg/m <sup>3</sup> ]
$\tau_w$ (tau)	Wall shear stress	[Pa]
$\phi$ (phi)	Magnetic flux	[Wb]
$\omega$ (omega)	Angular frequency	[rad/s]
<b>Greek capitals</b>		
$\Phi$	Volume of particles relative to the volume of aggregates	

# List of abbreviations

Cl SCC	Chloride Stress Corrosion Cracking
CAE	Computer Aided Engineering
CAM	Computer Aided Manufacturing
CNC	Computer Numerical Control
DLVO	Derjaguin, Landau, Verwey and Overbeek
DC	Direct Current
EDL	Electrostatic Double Layers
EDM	Electron Discharge Machine
EMF	Electromotive Force
EGR	Engine Gas Recirculator
EoM	Equation of Motion
FAE	Finite Element Analysis
ICE	Internal Combustion Engine
PM	Permanent Magnet
RPM	rotations per minute
rps	rotations per second
TEM	Transmission Electron Microscopy
TIG	Tungsten Inert Gas
VDW	Van der Waals
WIS	Weizman Institute of Science





# Chapter 1

## Introduction

Researchers have recently made considerable progress in the development of renewable energy systems to reduce the negative environmental impact of the emission of Greenhouse gasses. These new energy systems will eventually lead to a drastic reduction in the consumption of fossil fuels. Examples are wind turbines, solar panels, hydroelectric dams, etc...

Hydrogen is considered as one of these clean energy sources because it does not produce toxic gases when it is used as a fuel. The main drawback of this type of fuel is the way it is currently produced, which is primarily by methane steam reforming. Figure 1.1 (a) shows that the high temperature and energy needed for the reaction are achieved by the combustion of natural gas and air. This produces a lot of  $CO_2$ : the production of 1 ton of  $H_2$  produces 7 tons of  $CO_2$  [7]. Solar reforming, shown in Figure 1.1 (b), uses solar heat to achieve the high temperatures but also emits  $CO_2$  [1].

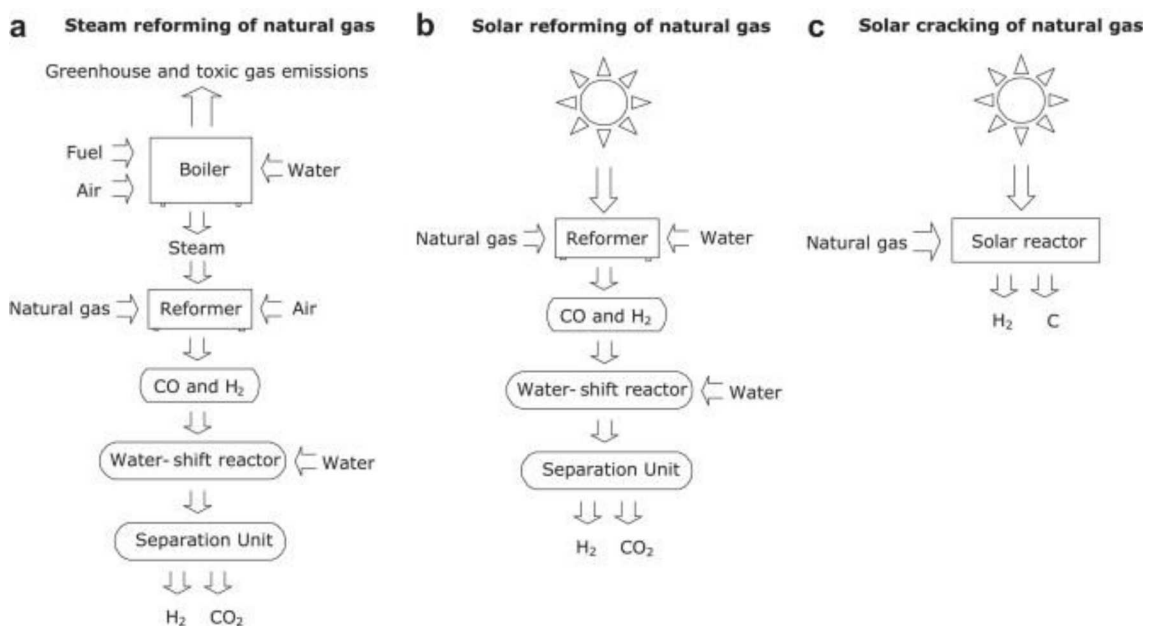
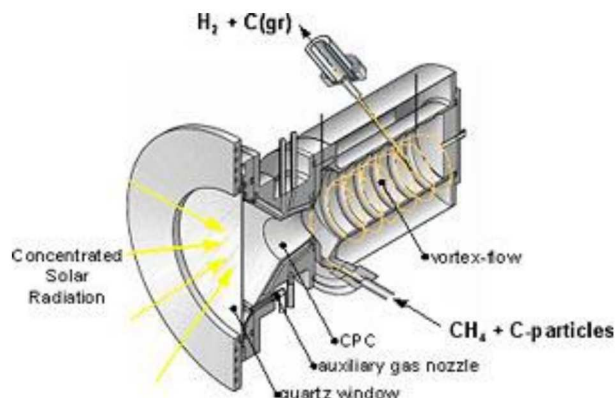
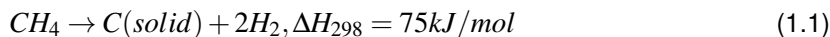


Figure 1.1: (a) steam reforming (b) solar reforming (c) solar cracking [1]

Figure 1.1 (c) shows a third way of producing Hydrogen called solar cracking of natural gas. This process uses concentrated solar energy and a solar reactor as shown in Figure 1.2 to produce the high temperature and energy needed to decompose  $CH_4$  according to the following reaction [16]:



**Figure 1.2:** Solar reactor used to split methane in Hydrogen and solid Carbon using concentrated solar energy [2]

Contrary to the combustion of natural gas with air in steam reforming, solar cracking uses no air or oxidizing medium. This means that there is no production of carbo-oxygen or nitro-oxygen based emissions. Temperatures of above 1800 K are needed to be able to decompose methane, although the  $H_2$  yield in this temperature region is strongly dependent on the residence time. Complete dissociation is achieved at above 2100 K [7]. These temperatures can be lowered without reducing the amount of decomposed methane by the use of carbon seeding as catalyst. Due to the seeding, particles with larger specific area are provided which act as nucleation sites for heterogeneous reactions. They also improve the heat transfer inside the reactor. When carbon seeding is used, decomposition starts at 600 K and nearly complete decomposition can already be achieved at 1500 K [17].

Besides the clean production of  $H_2$ , carbon black is also produced via solar cracking of methane. Carbon black is often used as additives for rubbers, inks, polymers and batteries. It can also be used for the production of carbon nanotubes. Presently, it is mainly produced by the furnace process. This process generates 5.9 kg  $CO_2$  per 1 kg of carbon black. Therefore, carbon production using solar cracking would provide an environmental-friendly alternative to the furnace process. Rodat et al. [5] researched if the properties of the carbon black produced by indirectly heated solar cracking are comparable to the properties of commercial industrial grade carbon black (E250G). They used Transmission Electron Microscopy (TEM) and Raman spectroscopy to determine the morphology and crystallinity of the particles. Various tests were performed in a temperature range between 1608 K and 1928 K and with varying flow rates of 10.5 to 21 NL/min. Results showed that, under the right circumstances (reactor temperature, flow rate,  $CH_4$  concentration), the properties of the produced carbon black could be comparable with the commercial grade carbon black in

terms of graphitization, specific area and conductivity. Given these results, solar cracking should be considered as a viable alternative production method for carbon black [5].

As can be seen, solar cracking of methane is a promising method for the production of hydrogen and the co-production of carbon black. While there are many advantages, there are also some problems that have to be solved before it can be used in practice. The main problems are [16]:

- The transient nature of solar energy
- Clogging of the reactor due to carbon deposition

Clogging occurs at the exit port due to agglomeration of the produced carbon particles, followed by deposition of these agglomerates on the reactor walls. When multiple layers of deposited carbon accumulate, the section through which the reactants flow decreases and eventually the outflow will be completely blocked [9]. The exit port therefore has to be cleaned during operation to allow for continuous functioning of the reactor.

The goal of this thesis is to find a solution for the clogging of the reactor. When the reactor outlet is blocked by carbon particles, there can be no outflow of the products and eventually the reactor window gets broken due to pressure build up. In this thesis, a rotary mechanism will be developed to prevent the exit port from clogging. It is important that this mechanism will not only clean the carbon deposition on the walls, but it will also capture carbon particles so that it can be separated from the gas in an additional process.



## Chapter 2

# Literature Review

## 2.1 Carbon Black

### 2.1.1 Commercial carbon black

Carbon black has its application in many different industries. 70% of the world production of carbon black is used as a reinforcement of rubber in the rubber tire industry. It is also used as black pigment for paint and for its electrically conductive properties. It is a fine powder with high surface area, primarily made up out of elemental carbon. This powder can be produced using a number of processes. Over 95% of the world production uses the oil-furnace process. However, processes like lampblack, impingement and the thermal decomposition of methane can also be used. Each of these processes produce different grades of carbon black with different characteristics. It can be characterized based on chemical composition, molecular structure, morphology and surface area [3].

#### 2.1.1.1 Chemical composition

The production processes mentioned above all produce carbon black with a high level of purity. Depending on the process used percentages between 97-99% of elemental carbon can be achieved [3]. Hydrocarbons are used to produce carbon black, which is why other elements like hydrogen, oxygen, sulphur, ash and volatiles are also present in small fractions between 0.00% and 1.5%.

#### 2.1.1.2 Molecular structure

Determining how the carbon atoms are arranged in carbon black structure is possible with an X-ray diffraction analysis. Results of this method shows that carbon black is composed of small crystallites which are structured as parallel graphitic layers. Even though carbon black becomes more graphitized when it is exposed for a long period of time to high temperatures of 2700-3000 °C, a fully graphite structure can never be achieved [18]. This is due to carbon black only having two-dimensional order, whereas graphite has three-dimensional order as shown in Figure 2.1. This

means that each layer in the carbon black can still rotate parallel to the other layers. As a result of this molecular structure, carbon black has electrically conductive properties [3].

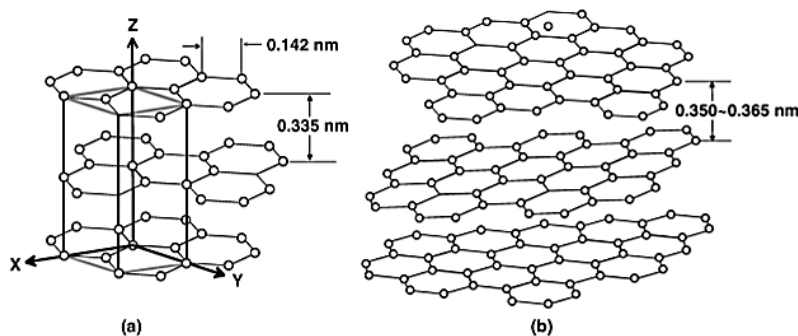


**Figure 2.1:** (a) Structure of graphite (b) Structure of carbon black [3]

### 2.1.1.3 Morphology

There are three morphological structures of carbon black: particle, aggregate and agglomerate. Figure 2.2 shows these different structures.

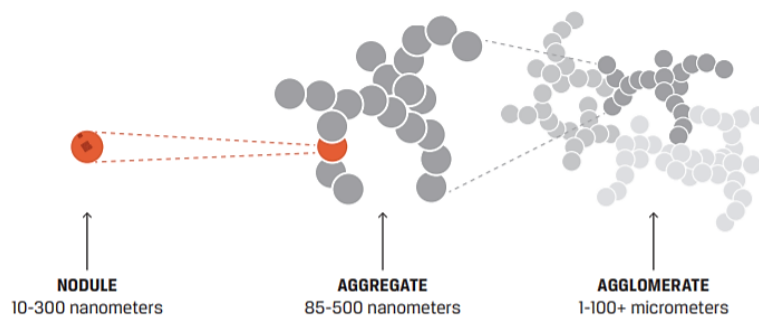


**Figure 2.2:** Morphological structures of a nanoparticle of a commercial carbon black [4]

The primary particle or Nodule is the smallest spherically shaped component. Although these particles almost never remain solitude, the characteristics of this morphological structure (diameter size and surface area) determine for which application the carbon black can be used. When these individual particles chemically bind, aggregates are formed. Separation of these aggregates can only be done by fracturing since they are chemically bound. It can be described as the chaining and clustering of carbon particles [3]. The last structures are the agglomerates. These consist of aggregates which are bonded by weak Van der Waals forces. Therefore, it is easy to overcome these forces and break the agglomerates back down in aggregates [18].

Another important aspect of the morphology is the specific area  $S$ . This area determines the interface chemistry between the carbon black particles and the medium in which it is dispersed. In tire industry, particles with specific area between 10-140  $\text{m}^2/\text{g}$  are needed, whereas for black pigments in paint they need fine particles between 9-16 nm [5].

### 2.1.2 Carbon black from methane cracking

Thermal cracking of methane is another possible production process for carbon black. Even though it is seen as a by-product in this application of clean hydrogen production, it can still provide an economical benefit. Since different production processes produce different grades of carbon black as mentioned above, it is important to determine whether the properties of carbon black produced by thermal cracking are comparable with the properties of commercial carbon black.

Rodat et al. [5] determined the properties of carbon black produced by cracking of methane using an indirectly heated solar reactor. They used Transmission Electron Microscopy (TEM), Raman spectroscopy and specific area measurements (BET) to determine the morphology and crystallinity of the particles. The results were compared with a sample of conductive carbon black E250 from Timcal Company. Various tests were performed in a temperature range between 1608 K and 1928 K and with varying flow rates of 10.5 to 21 NL/min. Results of the Raman spectroscopy are shown in Table 2.1. This method can determine the degree of graphitization represented by the graphitization index  $A_{D1}/A_G$ . A decreasing ratio means that the sample is more graphitized. The crystallinity length  $L_a$  can be derived from the peak intensity ratio  $I_{D1}/I_G$  using Eq. 2.1.

$$L_a = 4.4(I_{D1}/I_G)^{-1} \quad (2.1)$$

**Table 2.1** Results of the Raman spectroscopy showing the level of graphitization of test specimen produced at different reactor temperatures compared to carbon black E250G. Modified from [5]

Raman spectroscopy results				
Sample	Temperature of reactor (K)	$A_{D1}/A_G$	$I_{D1}/I_G$	$L_a$ (nm)
E250G	n.a.	3.7	1.6	2.8
Run 1	1608	3.8	1.6	2.8
Run 2	1693	3.6	1.6	2.7
Run 3	1778	3.6	1.6	2.7
Run 5	1928	3.4	1.7	2.6

Both the degree of graphitization and the crystallinity length of the four test samples are almost the same as the commercial sample. It can also be concluded that the difference of 320 K does not have a significant effect.

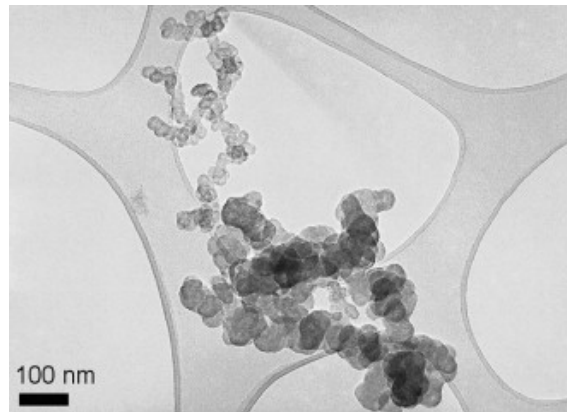
BET measurements revealed that the specific area of the test samples reached 100 m<sup>2</sup>/g. It was clear that the specific area increased with increasing temperature and decreased with increasing methane flow. Using the Electron Microscope Surface Area (EMSA) formula Eq. 2.2 the particle diameter can be calculated.

$$S = 6000/(\rho_p d_p) \quad (2.2)$$

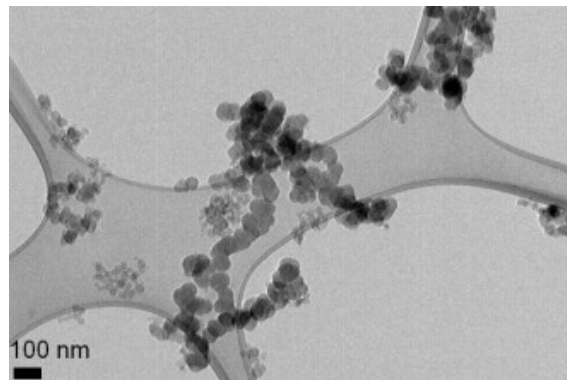
With  $S$  the specific area,  $\rho_p$  the density of the carbon particle (=1800 kg/m<sup>3</sup>) and  $d_p$  the particle

diameter. The mean particle diameter was calculated to be 33 nm.

Figure 2.3 shows Transmission Electron Microscopy (TEM) images of both commercial carbon black E250G and carbon black produced in a solar reactor by cracking methane. It shows that commercial carbon black has a more uniform and on average a larger particle size compared to carbon black from methane cracking.



(a) Commercial carbon black E250G



(b) Carbon black produced by solar reactor at 1778 K

**Figure 2.3:** TEM images of commercial carbon black vs. solar carbon black [5]

They concluded that, under the right circumstances (reactor temperature, flow rate,  $CH_4$  concentration), the properties of the produced carbon black could be comparable to the commercial grade carbon black [5].

## 2.2 Carbon Deposition

Carbon deposition is one of the main problems which withholds the solar reactor from commercial use [16]. The solid carbon particles deposit on the reactor window, the walls and the exit port. Carbon particles on the window (quartz) will cause it to overheat and will lead to thermal cracks. Due to the reactor outlet being much smaller in diameter than the reactor cavity, deposition of carbon here



causes interference with the outflow of the reaction products and will eventually completely block this outflow [7]. Carbon deposition can be reduced by changing flow parameters such as angle of injection, type of gasses, flow rates etc.

Another way of reducing the deposition is by changing the reactor design. Researchers have developed various different geometries. Jaya Krishna and Ozalp [6] developed an *aero-shielded solar cyclone reactor* shown in Figure 2.4. In addition to the main flow, they implemented a 'window-screening' and 'wall-screening' gas to create a vortex flow. The goal of the vortex flow was to keep the main methane flow in the center so that it would not interfere with the window and walls of the reactor, which might cause deposition of the produced carbon.

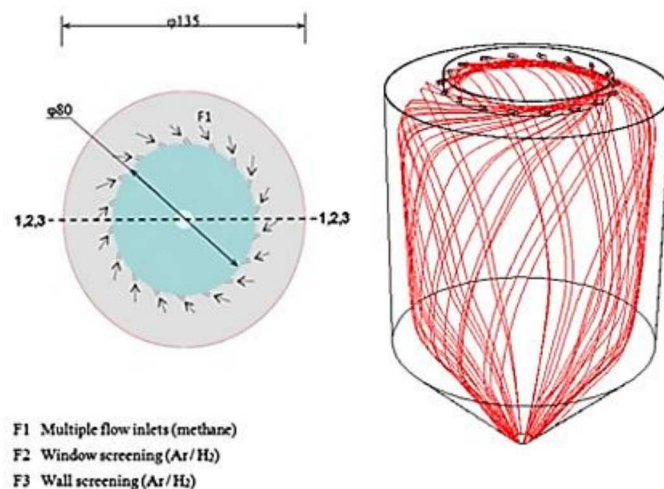


**Figure 2.4:** Aero-shielded solar cyclone reactor [6]

By changing the reactors' geometry, researchers at the Weizmann Institute of Science (WIS) used an inert auxiliary gas to produce the "natural tornado phenomenon". This enabled them to use low flow rates of auxiliary gas to create a curtain of gas flow to prevent carbon particles from depositing [7]. They later adjusted the design by adding in an third auxiliary gas flow to reduce the deposition near the exit port [8].

As demonstrated in Figures 2.4 and 2.5, different attempts have been made in order to try to reduce the amount of deposited carbon. Inert auxiliary screening gasses have proven to be an effective way of strongly reducing this amount on the reactor window and walls. However, the problem still remains at the exit port of the reactor.

### 2.2.1 Deposition mechanisms

Particle deposition in a gas flow is the result of interactions between gas-particle, particle-particle and particle-wall. Understanding the forces that contribute to these different interactions is important to get a better idea of how the carbon particles stick to the walls. It will also give an idea of the amount of force that is necessary to remove the particles from the surfaces. There are two key steps that have to be discussed to understand the deposition process. One of these is the trans-

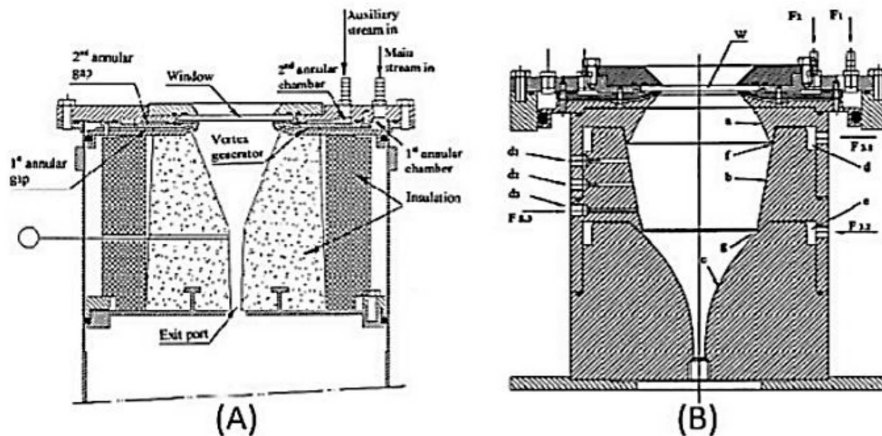


**Figure 2.5:** (a) Cross-section of the first cyclic reactor [7] (b) cross-section of the second cyclic reactor using the natural tornado phenomenon [8]

port step to bring the particle in the vicinity of a surface. The other is the attachment step which accounts for the interface-chemistry between particle-particle and particle-wall [9].

The transport step handles the gas-particles interactions and is generally due to several possible mechanisms. Depending on the parameters, each of these mechanisms has a different level of importance in the process. One of the parameters that is key is the average diameter of the particles [19]. In this section, we will briefly explain the various mechanisms that contribute to the deposition.

### 2.2.1.1 Gravitational settling

The magnitude of these forces is influenced by size and density of the particle. It becomes of more importance when the carbon particles agglomerate, for example, when a carbon feeder particle is added. This causes the particles to grow and become heavier. As a result, the gravitational force on the particles increases and will induce a downward motion to the bottom of the wall [9].

### 2.2.1.2 Eddy diffusion

Diffusion occurs when there are areas of high concentration and areas of low concentration in the gas stream. Particles will migrate from a higher concentration area to a lower one. Diffusion is more effective on particles with smaller diameters ranging between 10-50 nm. However, the deposition rate is still a lot less than the deposition caused by thermophoretic force [19].

### 2.2.1.3 Turbulent impaction

When transported in a gas, particles with larger diameter have more trouble with following the gas stream due to inertia. This causes them to collide with the walls. Particles with small diameters (1-200 nm), like carbon black, have almost no trouble following the gas stream and therefore have a low deposition velocity due to impaction [19].

### 2.2.1.4 Thermophoretic force

Due to the temperature gradient near the surface, the carbon particles migrate in the direction of decreasing temperature as shown in Figure 2.6. This thermophoretic force is caused by the differences in velocity of the particles because of the differences in kinetic energy. The hotter gas molecules have a higher velocity and therefore have a higher impact than cooler molecules. This creates a net force on the solid carbon particles towards the surface walls [20].

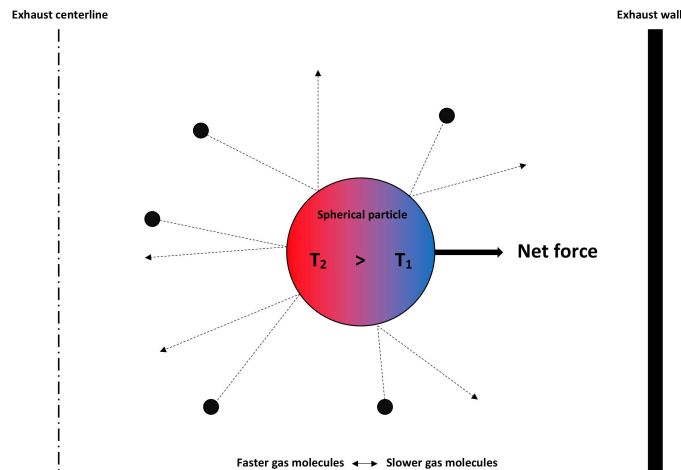


**Figure 2.6:** Thermophoretic net force on a spherical particle

It is clear that in this application, the thermophoretic force is the main reason for deposition of carbon black particles with diameters ranging between 10-70 nm. However, when carbon seeding particles are introduced in the reactor, the carbon particles agglomerate. This results in the formation of particles with substantially larger diameters. Gravitational settling and turbulent impaction therefore becomes of greater importance.

### 2.2.2 Adhesion to the surface

The particles being brought in the vicinity of the wall due to the forces mentioned in the section above, attach to the walls or to deposited particles. This is the attachment step in which interface-chemistry plays an important role. This interface-chemistry for deposition is often explained using the DLVO-theory. It combines Van der Waals forces and Electrostatic Double Layer (EDL) forces to explain the interface-chemistry between particle-wall and particle-particle when they are within the range of a few nanometers of each other.

#### Van der Waals

Van der Waals forces are often attractive forces induced by the polarizations of dipoles. Three different types of dipoles exist and depend on the kind of dipoles that induces the force [21]:

- *Keesom interactions*: between two permanent dipoles

- *Debye interactions*: between a permanent dipole and an induced dipole
- *London dispersion interactions*: between two induced dipoles

The London dispersion forces contribute often the most, since they even occur between neutral atoms, and therefore the Keesom and Debye interactions are negligible. The induced dipoles are the result of the continuously changing position of the electron cloud around the nucleus of the atom. This creates a partial charge distribution  $\delta$ . These instantaneous dipoles will then induce another dipole in a nearby atom leading to an attractive force between them [22].

Figure 2.7 shows the Van der Waals (VDW) potential in function of the distance  $h$  between a spherical colloidal particle and a flat surface. It shows that when the distance between them becomes smaller, the VDW interactions increase. This is until the minimum distance is reached, also known as the Bohr-limit. The repulsive forces between the electron clouds will prevent the particles to come any closer.

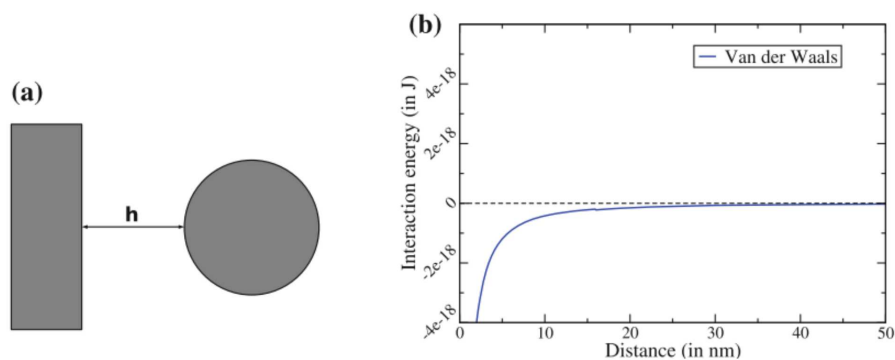


**Figure 2.7:** (a) Representation of the VDW potential energy for a spherical colloidal particle interacting with a flat surface (b) As a function of the particle-surface distance [9]

### Electrostatic double layer

The electrostatic double layer (EDL) force has to be taken in consideration when the particles or the wall surface is electrically charged. Since surfaces are usually only charged in a liquid medium the EDL forces will have no effect on the particle-wall interactions. The DLVO-theory for an application in a gaseous medium is therefore only described by the Van der Waals force [23].

The main limitation of this DLVO-theory is that it does not take into account the influence of the surface roughness. This influence is not negligible when it comes to adhesion to the surface due to the Van der Waals force being a short-range interaction force [24, 9]. These surface heterogeneities increase the separation distance between the particles which in return reduces the interaction energy as it is seen in Figure 2.7. Even nanometer scale roughness can have significant reduction of adhesion as a result [25]. This means that, when a reduction in the force necessary to remove the adhering particles from the surface is desirable, this surface should have a certain level of roughness.

### 2.2.3 Adhesion and aggregates of carbon black particles

Adhesion of particles and aggregates to each other is very similar to the adhesion to the surface discussed in the previous section: the inter-particle short-range Van der Waals force between the particles surfaces is mainly responsible for the interaction when the particles are smaller than  $100 \mu\text{m}$  [15]. The ratio surface area to volume influences the adhesive force between the particles. As a result, a powder with smaller particles will have significantly higher adhesive interactions [26, 27]. However, there are other factors that determine the cohesiveness of the powder. Kendall and Stainton [10] concluded that the strength of the aggregates was not only determined by this adhesion, but also by the particle diameter, the packing fraction  $\Phi$ , shape and how the aggregate is formed. This is important to eventually determine the tensile stress that is required to separate the aggregates from each other: the flaws and cracks in the aggregates that are associated with the previously mentioned factors will reduce the total required stress. Figure 2.8 shows the most important factors:  $W$  is the energy required to separate one  $\text{m}^2$  of adhering interface which is linked to the Van der Waals force,  $D$  the particle diameter and  $\Phi$  the volume of particles relative to the volume of aggregates. Eq. 2.3 uses these parameters to calculate a realistic value for aggregate strength [10].

$$\sigma = 15.6 \frac{\Phi^4 R}{(Dc)^{1/2}} \quad (2.3)$$

However, in this equation  $R$  is used which is the non-equilibrium value of  $W$  and the flaw length  $c$  is also taken into consideration.

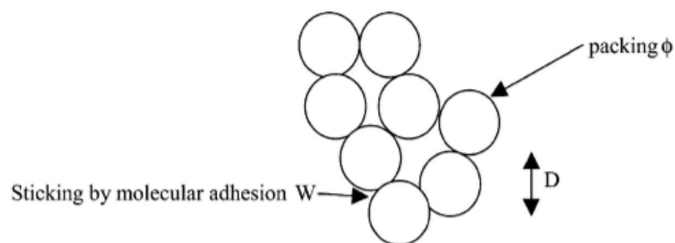


**Figure 2.8:** Schematic representation of cohesive powders containing spherical particles [10]

### 2.2.4 Exhaust clogging

Clogging at the exhaust occurs when multi-layered deposits accumulate on the walls. This decreases the sectional area and will eventually block the exit port. It is the end result of four phenomena represented in Figure 2.9 [9].

The deposition mechanism was explained in-depth in previous section. Another important phenomena is resuspension which is the detachment of the particle from to wall due to shear forces being able to overcome the particle-wall interactions. This makes the particle re-enter the gas stream. Agglomeration occurs when the repulsive forces between particles can be overcome by attractive

Van der Waals forces. This will eventually lead to clogging.

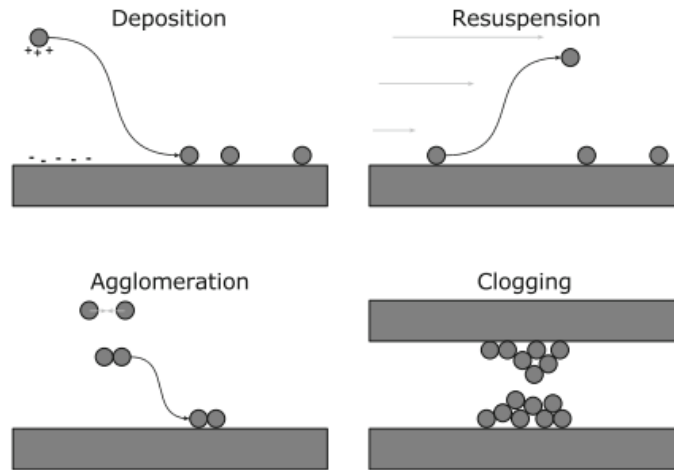


**Figure 2.9:** The complete process consists out of four phenomena [9]

Tests performed by various research groups show that the carbon clogging will inevitably lead to blocking the outflow of the reaction products. Kogan and Kogan [7] performed numerous tests using different geometries. Their longest test lasted for 37 minutes. In that test, the exit port was only partially blocked by deposited carbon. In the other tests, which did not last as long, it was almost always the clogging of the exit-port due to the carbon particles that led to termination of the tests.

## 2.2.5 Deposit removal mechanisms

Particle deposition can be found in a wide variety of applications and mechanisms which can be studied to find a possible solution. Similarities and differences can be examined to optimize and enhance these existing designs to solve the problem at hand.

### 2.2.5.1 Shear Force

A particle deposited on a surface experiences different forces acting on it in a fluid flow. Figure 2.10 shows a simplified representation of these forces.

The Van der Waals force  $F_V$  is responsible for the adhesion between the particle and the flat surface as discussed in subsection 2.2.2. It is defined as

$$F_V = \frac{A_H d_p}{12Z_0^2} \quad (2.4)$$

where  $A_H$  is the Hamaker constant and  $Z_0$  is the distance between the particle and the surface [11].

The shear flow of the gas creates a drag force  $F_D$  on the particle. According to Yung et al. [28] the

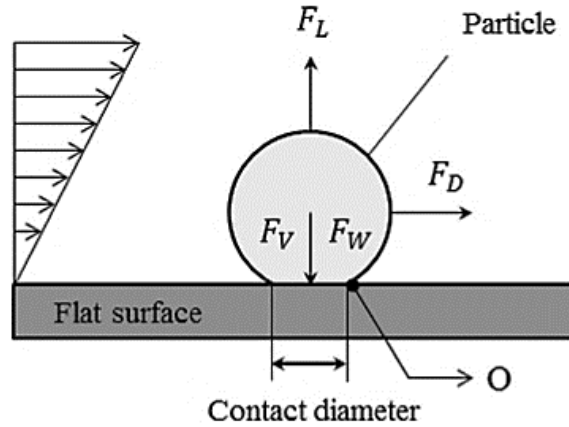


**Figure 2.10:** Forces acting on a deposited particle in a fluid flow with  $F_V$  the Van der Waals force,  $F_W$  the weight force,  $F_D$  the drag force and  $F_L$  the lift force [11]

drag force can be calculated using

$$F_D = 8\rho_g(u^*d_p)^2 \quad (2.5)$$

with  $\rho_g$  the density of the gas and  $u^*$  the friction velocity given by

$$u^* = \sqrt{\frac{\tau_w}{\rho_g}} \quad (2.6)$$

with  $\tau_w$  is the wall shear stress.

Abarham and Hoard [19] demonstrated that the lift force and weight force are negligible for submicron particles. This means that only the adhesive Van der Waals force  $F_V$  and the drag force  $F_D$  due to the shear flow of the gas are relevant for particle re-entrainment.

When the Van der Waals force is equal to the drag force, particles will be removed from the surface. Combining Eq. 2.4 and Eq. 2.5 delivers a criterion for the critical shear velocity  $U_{cr, shear}$  necessary for this removal [28]:

$$U_{cr, shear} = \left[ \frac{A_H}{12Z_0^2(0.316)\left(\frac{\rho_g D}{\mu_g}\right)^{-0.25}\rho_g d_p} \right]^{\frac{1}{1.75}} \quad (2.7)$$

where  $\mu_g$  the dynamic gas viscosity and  $D$  the transient tube diameter.

Abarham and Hoard [19] concluded that the shear force would not be an effective way of removing particles with particle diameters smaller than 400 nm of surfaces because the mean gas flow velocity would have to be too high.

## 2.2.6 Exhaust gas recirculation cooler

When looking for applications that work at high temperatures with similar chemical elements such as hydrocarbons; internal combustion engines (ICE) cannot be overlooked. In particular, there is one specific apparatus used commonly in diesel engines that has comparable soot deposition problem: the exhaust gas recirculation (EGR) cooler. The main goal of the EGR cooler is to reduce  $NO_X$

emissions by mixing a portion of the exhaust gas with the incoming fresh air. Recirculated exhaust gases get cooled by the engine coolant, however, as discussed before, the cold surfaces trigger deposition of the soot particles. Deposited soot hinders the efficiency of the EGR cooler, therefore, removal of this layer is important. However, the question is whether these removal mechanisms are also applicable to the exhaust of a solar reactor.

### 2.2.6.1 Large particle bombardment

There are certain observations in the EGR cooler of deposition removal due to large particle bombardment onto the deposition layers [12]. In this case, the larger particles hit the deposition layer with such a force that flakes come off the layer. While this could be a very elegant and simple solution, it certainly is not suitable for the solar reactor exhaust. To recreate this large particle bombardment, another reactor flow would have to be induced which could interfere with the existing flows and possibly also with the actual cracking of the natural gas. It is also not a stable and predictable process.

### 2.2.6.2 Water condensation

Abarham and Hoard [19] discussed a removal mechanism tested in EGR coolers that uses water condensation to remove the deposit layer. As seen on Figure 2.11, the vapor condensates instead of the soot particles and that way the surfaces stay clean. Enough water vapor has to be used at the right pressure and the cooled surfaces need the right temperature. Just like the previous example this mechanism needs another substance in the reactor which is not recommended as this could have negative results for the reactor effectiveness. It could also cause chemical reactions that are not desired.



Figure 2.11: Condensate layer formed on the surface [12]

### 2.2.6.3 Kinetic energy

As previously described, the main force that keeps the soot particles attached to the surface is the Van der Waals force. There is a hypothesis that with a force larger than this one, deposited particles could be removed from the surface. As previously described, the main force that keeps the soot particles attached to the surface is the Van der Waals force. There is a hypothesis that with a force larger than this one, the deposited particles could be removed from the surface [19]. This



can be done by having the kinetic energy of the particles bigger than the Van der Waals potential energy. This high kinetic energy could be reached by bringing the surfaces on higher temperatures and that way the thermal forces can negate the Van der Waals forces.

### **2.2.7 Nanocoating**

Nanocoating is a microscopic surface finish to improve durability and/or properties of the surface material. This technique could possibly be used to hinder the carbon particles from depositing on the walls. There are many coating possibilities which require careful attention in selecting the right one to avoid adverse effects due to chemical conflict. For example, stainless steel surface finish product cannot contain any chlorides. Because chloride ions, in combination with tensile stresses and elevated temperatures, could cause cracking of the stainless steel [29]. This process is called chloride stress corrosion cracking (Cl SCC). Similarly, coating the critical parts of the solar reactor to avoid carbon particle deposition would have such risks. This requires an extension of research in materials science, which is out of the scope of this thesis.



## Chapter 3

# Design Methodology

Based on the literature survey, a clear understanding of the physical properties of the deposited carbon black and the physical mechanisms that cause the deposition has been achieved. This, in addition with researching already existing mechanisms that are used in the industry for particle deposition removal, has led to the development of a new design. The CAD-models and -drawings are made using the CAD-software SolidWorks. This software also has a rendering tool that can make the models look more realistic.

### 3.1 Constraints

The first step of the design process is to define the main goal, which is to develop a mechanism that can achieve efficient carbon cleaning or carbon deposition removal. The next step is to outline the design constraints:

- The mechanism must not interrupt the gas flow
- Material of the mechanism should withstand high temperatures
- Hydrogen leakage should be minimal and monitored by sensors
- The mechanism must be compatible with the back-plate of the existing reactor
- Compact
- Possibility to be coupled with carbon black collection
- Cost effective
- Manufacturable design

The cleaning mechanism has to be built in a way that it should not interrupt the gas flow to prevent pressure build-up inside the reactor. Therefore, the best approach is to set for continuous cleaning without interchanging of parts. Because the gas flow through the mechanism is at high temperatures, the heat can damage the components of the mechanism. The gas temperature in the reactor at STTL can reach up to around 500 °C. Since hydrogen is extremely flammable when it comes in contact with oxygen, it is important that the leakage is as small as possible. For easy implementation to the existing reactor, the exit port mechanism has to fit on the back-plate of the reactor and

should be as compact as possible. Due to the economic benefit of the carbon black particles, it should be possible to collect them which means that they cannot be chemically removed or burned like in Diesel engines. A simple design will grant smooth manufacturing of most components at the machine shop of campus De Nayer while others can be purchased. This reduces the total cost of the exit port.

## 3.2 Preliminary design

Several design ideas were discussed during the course of brainstorming to develop a novel concept that could function well with the set-up of the solar reactor. Figure 3.1 shows the initial design concept that was developed. The large disk on the left-hand side of the figure is the back-plate of the reactor. This part had to be included to the design because it had to undergo some changes. In this back-plate a hole is fit which functions as the exhaust of the reactor. The exhaust gases then travel through the exhaust where the deposition of carbon black takes place. A scraping mechanism is included to remove this deposition and counteract the clogging of the exhaust. The scraper is driven by the gear on the right-hand side of the figure.

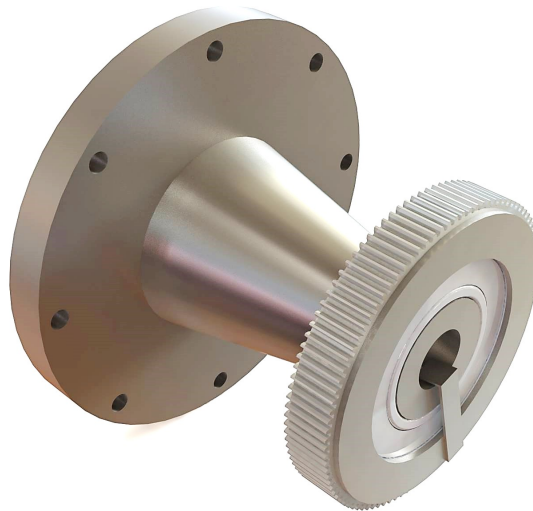


Figure 3.1: CAD-drawing of the preliminary design

### 3.2.1 Exit port geometry

Geometric shape of the exit port determines the cleaning devices that can be used to clean it. Most exit ports used in today's solar reactors are tubular. However, since a gradually increasing gas flow velocity  $u$  can have a positive influence on the re-suspension of particles (see subsection 2.2.5), the shape of the exit port can be used to accelerate the gas flow. A higher resuspension rate means that there will be less overall deposition of particles.

The volumetric flow rate  $\dot{V}$  can be calculated using

$$\dot{V} = uA \quad (3.1)$$

with  $u$  the flow velocity and  $A$  the cross-section area.

The mass flow  $\dot{m}$  is assumed to be constant which means that the volumetric flow rate is also constant. Therefore, the flow velocity can be changed by varying the the cross-sectional area.

$$u_o = u_i \frac{A_i}{A_o} \quad (3.2)$$

with  $u_o$  the outlet velocity,  $u_i$  the inlet velocity,  $A_i$  and  $A_o$  the inlet and outlet cross-sectional area, respectively.

By evaluating Eq. 3.2 and taking into consideration that a higher gas flow rate  $u$  helps with the deposition problem, it is clear that a conical shaped exit port with larger  $A_i$  than  $A_o$  is more suitable than a tubular shaped exit port.

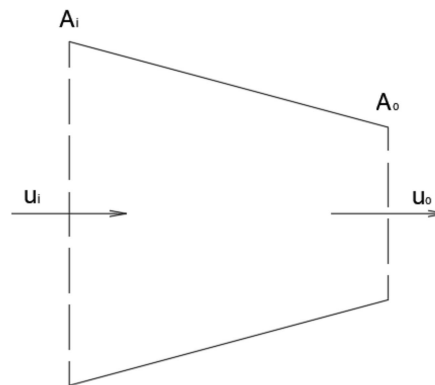


**Figure 3.2:** Sketch of the conical shape with varying cross-sectional area

Although Abarham and Hoard [19] concluded that the critical flow velocity  $U_{cr, shear}$  to provide enough shear force to remove particles would be too high to be efficient as described in sub-section 2.2.5, it will still increase the re-suspension rate of particles and therefore have a positive impact on the removal.

Therefore, it is decided that the final design concept should have this conical shaped exit port attached to the back plate of the existing reactor. This conical part will be placed at the back-plate of the reactor with an angle so that the bottom part of the horizontally placed exit port does not have an incline. This is to prevent the larger particles from falling back down into the reactor and settling at the bottom due to gravity.

### 3.2.2 Cleaning mechanism

Removal of deposited carbon black particles is possible when the Van der Waals force is overcome by an externally applied force. This force can be the drag force  $F_D$  due to gas flow, but this

was proven to be inefficient. Alternatively, mechanically applied force can work. For example, a rotational motion of a solid beam-like component can scrape the deposited layer of carbon black by providing large enough shear force  $F_s$  which can overcome the Van de Waals force. A scraper design that was developed for removal of deposited carbon particles is shown in Figure 3.3. As it is seen, the scraper is a rectangle with a triangular shaped shave on top. This shaving is to push particles that have been removed towards the exit of the reactor.

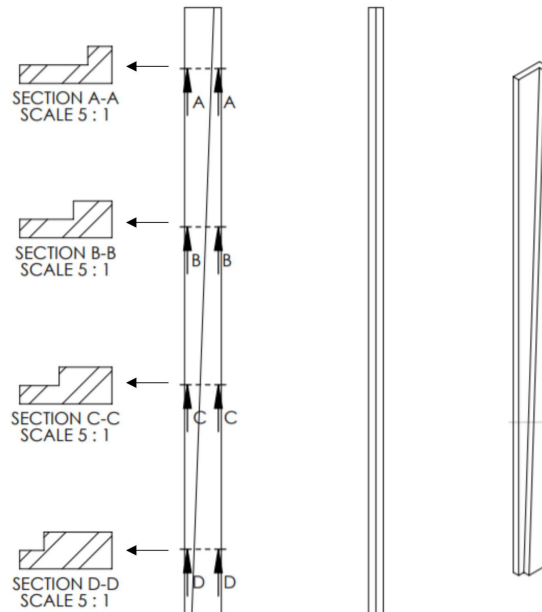


**Figure 3.3:** Scraper used to remove the deposited carbon black

The scraping surface will rotate with a spacing of 0.5 mm from the wall of the conical exit port. By doing this, the lubricant properties of carbon black can be utilized to prevent wear on the scraper due to friction with the wall. This means that a layer of 0.5 mm of carbon black will be formed before the scraper starts removing the particles, however this layer is too thin to block any reactant outflow and will therefore not have a negative impact on the functioning of the device. Additional benefits are that it makes it easier to assemble it and that it leaves room for possible manufacturing errors.

### 3.3 Design improvements

Although the preliminary design shown in Figure 3.1 is able to function when it is independent from the reactor, it is not yet possible for this mechanism to operate within the complete set-up of the existing reactor (i.e. attached to the back of the reactor and followed by a subsequent outlet system). Several improvements, which will be discussed in this section, had to be made to allow for correct functioning of the design

### 3.3.1 Fixation of the scraper

Taking the design specification from section 3.1 into account, the rotational movement of the scraper should not interrupt the gas flow and should operate with minimal leakage. It should also be possible to attach other components to the back of the mechanism like a filter or a tubing. This is accomplished by attaching the scraper to a tube, through which the hydrogen gas can continuously flow. The tube is driven by a motion system inspired part as explained later. It rotates inside a static housing as shown in Figure 3.4, and is supported by two bearings. This housing can be welded

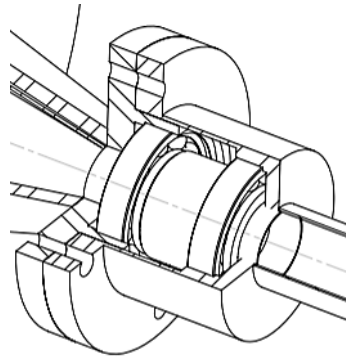


**Figure 3.4:** Scraper used to remove the deposited carbon black

to the conical shaped exit port described in subsection 3.2.1 on one end, while the other end can be used to attach a subsequent system. The two bearings are used to make it possible for the tube to rotate inside the housing and keep it in place. Depending on which driving method is used, additional sealing components, like rotating seals, have to be added to keep this housing airtight. Also, the placement of the components can vary.

### 3.3.2 Exhaust cooling

Exposure to high flux radiation increases the temperature of the gas flowing through the mechanism which escalates carbon deposition. Therefore, cooling of the cleaning mechanism is one of the design considerations covered in this thesis.

In section 2.2, physics behind the carbon deposition was explained in detail. In summary, the fundamental reason is the condensation which is driven by thermophoretic forces and Van der Waals forces. Cooling of the exit port will increase the condensation of carbon particles and force its condensation. This seems contradictory but will be an effective method to increase the efficiency of the apparatus. The cooling mechanism is implemented in conical part of the rotary cleaning mechanisms. In this part the deposited carbon black will be removed, and thus clogging of the exhaust further downstream is prevented. The cooling effect will be also helping in reducing the high temperature related risks of crucial auxiliary parts such as the fittings and bearings as well as the rotary shaft seals to prevent hydrogen leak.

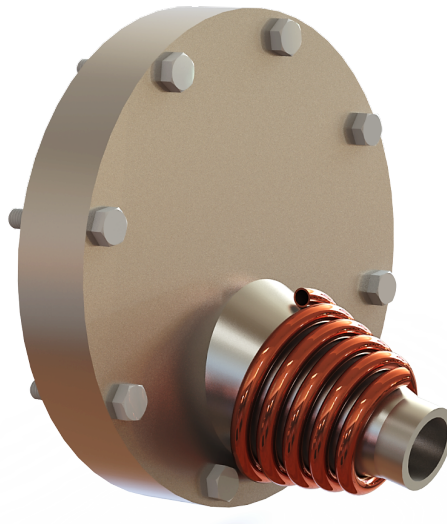


**Figure 3.5:** Wrapping of the exhaust with copper cooling channels

During the brainstorming of the cooling mechanism design, several concepts were inspected and judged on their viability, but most of them were too complicated or too time consuming. Therefore, a more practical solution was selected by simply wrapping copper tubes around the conical exhaust, shown on Figure 3.5. Copper has a high thermal conductivity which could provide sufficient heat transfer to cool down the exhaust gases. It is important to note that simply wrapping the copper tubes will result in a very thin contact area for heat transfer. Introducing bonds of added material between the cooling channels and the exhaust cone will improve this heat transfer. In this case, copper is used as added material for its high thermal conductivity. It is molten at the contact point of the copper tubes and the stainless-steel cone wall. This principle is shown in Figure 3.6.

Different processes can be used to join the bonding material with the cooling channels and the exhaust wall. The high temperatures of most of these processes can weaken or even damage the stainless steel so that it loses critical properties, like its corrosion resistance for example. Therefore, another process is suggested: MIG brazing. It works at lower temperatures so the stainless steel is not damaged [30]. The filler material melts and accounts for the joining of the parts. Any other welding processes would need much higher temperatures. Another advantage of the MIG Brazing is its simple execution. The geometry and placement of the conical exhaust are rather complex, but with this process the copper tube can be attached gradually over its entire length, with little working room.

Although an overview of the cooling mechanism and how it works have been described, several design parameters are still unknown. For example, the diameter of the cooling channels and their wall-thickness, the insulation material and thickness, the width and thickness of the bond, the spacing between the windings, etc. These parameters and the effectiveness of this cooling mechanism are evaluated via numerical evaluation which is explained in section 4.4. Another notable remark



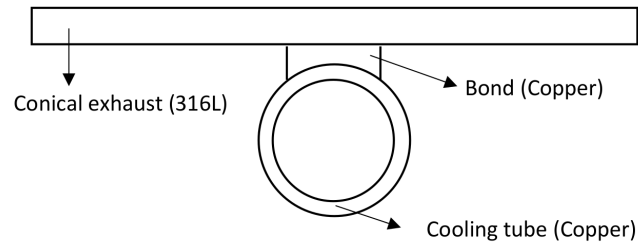


**Figure 3.6:** The joining parts with the bond

is that this thesis will contain only a theoretical realization of this cooling mechanism, because only limited time is available and no actual high-temperature experiments can be done. This is also why cooling channels and bonds will not be visible in further CAD-drawings and manufacturing figures.

### 3.4 Motion mechanism

There are several ways to generate rotational motion of the scraper inside the outlet. Two motion mechanisms have been selected as suitable options for this application: (1) a mechanical drive, and (2) a magnetic drive. Both have advantages and disadvantages over each other and they will therefore be compared to find the best possible solution.

#### 3.4.1 Mechanical drive

##### Power component

The first motion mechanism features an external motor and a transmission to deliver predetermined velocity. The Silverpack 17C from Lin Engineering was chosen to meet the power needs of the design. This integrated motor with controller and driver might not be the most efficient for the calculated torque and power demands. It is also too specific with a step angle of  $1.8^\circ$  and resolutions up to  $1/256$ . However, it is a good stepper motor which is easily controlled, and can be used at different rotational velocities. Because it was available in the lab to use, that made it a good choice to save budget.

The Silverpack 17C includes a few different components:

- NEMA 17,  $1.8^\circ$  stepper motor of type CO 4118L-07S
- R256 Single Axis Controller with driver
- DB-9 cable with white 3-pin connector
- USB to RS485 converter card with USB cable

The parts were connected as described in the data-sheet, found in Appendix B, using a 24 V DC power supply and connecting the correct cables of the DB-9 cable. With the Lin Engineering-software Lin Command the stepper motor can be programmed for use.

### Transmission

The velocity for the scraper rotation will be around one rotation per minute. Higher velocities are not necessary and would only increase power demands and wear. They will be varied slightly in the experimental and testing phase to find an optimal angular velocity. To keep smooth operation with minimal vibrations and thus noise, the stepper motor should be running at higher speeds than 1 RPM. Therefore, a reduction will be added between the rotating tube and the shaft of the motor. The first part of this transmission is a planetary gearbox type PM42 from IMS. This gearbox is easily mountable on the motor and is very compact. This gearbox has a gearbox ratio  $i_{gb}$  of 50.

Second part of the reduction is handled via belt-pulley system. The shaft of the planetary gearbox drives a small pulley, which drives a larger pulley using a timing belt. Both the belt and the pulleys are from SKF and have a pitch of 5 mm. The small pulley has a pitch diameter  $d_{dk}$  of 19.10 mm and the larger pulley has a pitch diameter  $d_{dg}$  of 38.20 mm. The belt width is 9 mm and the belt length can be determined as follows. Using Eq. 3.3, the margins for the axis distance of both pulleys can be calculated [31].

$$0.5(d_{dg} + d_{dk}) + 15\text{mm} \leq e' \leq 2(d_{dg} + d_{dk}) \quad (3.3)$$

If the global axis distance  $e'$  lies between 43.65 mm and 114.58 mm the pulleys have enough spacing in between while unwanted belt vibrations are avoided. To protect the motor from heat, this axis distance will be taken as large as possible while still observing the calculated limits. The definitive belt length  $L_d$  can be calculated by rearranging Eq. 3.4 [31].

$$e = \frac{L_d}{4} - \frac{\pi}{8}(d_{dg} + d_{dk}) + \sqrt{\left[\frac{L_d}{4} - \frac{\pi}{8}(d_{dg} + d_{dk})\right]^2 - \frac{(d_{dg} + d_{dk})^2}{8}} \quad (3.4)$$

The definitive axis distance  $e$  is chosen as close as possible to the upper limit of 114.58 mm as discussed before, while ensuring the resulting belt length  $L_d$  is a round value which can be bought from the SKF catalogue. The final value for the belt length is thus 300 mm.

The total speed reduction of this transmission line can be calculated using Eq.3.5:

$$\omega_{out} = \frac{\omega_{in}}{i_{pulleys} i_{gb}} \quad (3.5)$$

with  $\omega_{out}$  the output radial velocity and thus the velocity of the scraper,  $\omega_{in}$  the radial velocity of the stepper motor,  $i_{pulleys}$  the ratio  $\frac{d_{dg}}{d_{dk}}$  and  $i_{gb}$  the gearbox ratio. This gives a total reduction of 100, which means the motor should run at around 100 RPM. With a stepping angle of  $1.8^\circ$ , the motor takes 200 steps for one full rotation. The maximum resolution of 1/256 was chosen for effortless stepping, meaning it now takes 51 200 steps for a rotation. The software used to program the stepper motor is called LinCommand, from Lin Engineering, and needs a value in steps per second. With a reduction of 100 this value would be 51 200 000 for 1 rps. Divided by 60 for a velocity of 1 RPM this equals approximately 85 333 steps per second.

The total torque amplification of this transmission line can be calculated using Eq.3.6

$$T_{out} = i_{pulleys} i_{gb} T_{in} \quad (3.6)$$

with  $T_{out}$  the output torque and thus the torque available at the scraper and  $T_{in}$  the torque of the stepper motor. This means that the torque delivered by the stepper motor will be amplified by a factor 100.

### Supporting parts

The large pulley at the end of the transmission drives a small tube inside the housing. This set-up limits hydrogen leak drastically. However, this also means that a very precise alignment is needed. Therefore, two bearings are introduced in the housing to support this tube and ensure smooth rotating motion. To avoid problems with the fittings in the set-up, the material of the bearings will also be stainless steel with a similar thermal expansion coefficient. A shield was also added to protect its working from dust and other impurities from the outside. Two W6204-2Z bearings were chosen to support the rotating tube.

### Sealing

This motion mechanism design is quite simple, but an opening in the housing is unavoidable when the power source is on the outside of this housing while the torque is needed inside. A sealing solution is needed to reduce the hydrogen leakage as much as possible. For this application, a radial shaft seal from SKF would be ideal. The 20x47x7 HMSA10 V has the right dimensions and is manufactured from a fluoroelastomer with operating temperatures ranging from -20 to 200 °C.

## 3.4.2 Magnetic drive

The magnetic drive features a permanent magnet motor (PM-motor) to drive the hollow tube with the scraper attached to it. The stator will be placed on the outside of a cylindrical hub, while the rotor will be placed on the inside of this hub. By using a keyed connection, the tube can be connected to the rotor of the PM-motor so that it rotates with it.

A permanent magnet motor has surface-mounted magnets on its rotor. These magnets can be seen as flux sources. They interact with the magnetic fields that are induced by the poles on the stator. These poles have solenoid windings that are isolated from each other in which current flows and are wound around a magnetic core. For PM-motors, steel is often used as material of the stator. The windings produce a magnetic field in the core material by inducing a north- and south-pole. These poles can be switched by inverting the current that flows through the solenoid windings. Due to the attractive or repulsive forces between respectively unlike poles and like poles, a rotary motion can be achieved by controlling which pole of the stator is electrified.

Figure 3.7 shows the schematic model of how the permanent magnet motor will be used in this application. The stator is placed on a cylindrical hub made out of 316L Stainless Steel. The stator windings are not shown for simplicity. Since the magnetic flux produced by the stator is able to flow through the material and the small air gap, the permanent magnets still experience the flux and a rotary motion can still be achieved as described above. This makes it possible for the hollow tube with the scraper attached to it to be driven inside a fully closed cylindrical hub. Therefore, the

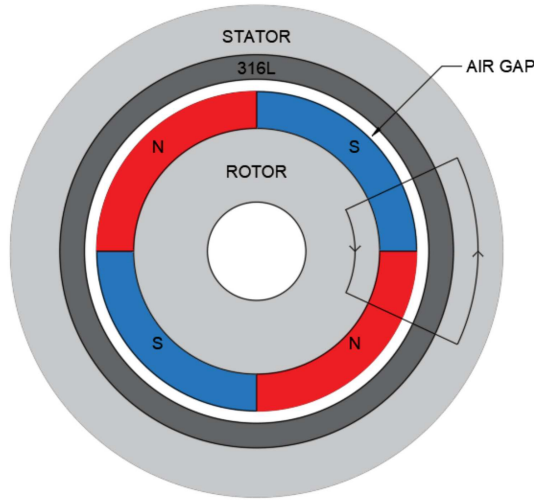


**Figure 3.7:** Schematic model of the magnetic drive (modified from [13])

hydrogen gas that may leak through the stationary cone and the rotating tube will not come into contact with the outside air. This is the main advantage over the mechanically driven design where a gap in the cylindrical hub has to be provided so that the belt can be externally driven. This means that additional rotary seals have to be added to keep the hydrogen leakage below the dangerous values. This will not be necessary in this design.

Hanselman [13] uses a magnet circuit model to determine the parameters in the design of a PM-motor. The most important parameters of a permanent magnet motor are mutual torque and back EMF. These parameters can be numerically determined by using the magnetic circuit model of the configuration. This model shows the flux flow for half of a north pole and half of a south pole.

The concepts of a magnetic circuit model will first be briefly explained. It is an analogy with electronic circuit models using reluctance  $R$  and flux  $\phi$  instead of resistance and current. Every material through which the flux has to flow has a certain reluctance  $R$  depending on the material properties. This represents a certain storage of energy of the magnetic field and can be determined using

$$R = \frac{l}{\mu A} = \frac{1}{P} \quad (3.7)$$

with length  $l$ , permeability  $\mu$  and the cross-sectional area  $A$  of the material and permeance  $P$ .

When the flux density  $B$  is constant over the cross-section  $A$ , the flux can be calculated using

$$\phi = BA \quad (3.8)$$

Using the electric model analogy, the schematic model of Figure 3.7 can be translated in the following magnetic circuit model shown in Figure 3.8

The rotor and stator have reluctances  $R_r$  and  $R_s$ . The magnets also have a reluctance  $R_m$  and act as a flux source  $\phi_r$ . Most of the flux passes through the air gap and is called the air gap flux  $\phi_g$  with the reluctance of the air gap being  $R_g$ . This air gap flux passes through the 316L Stainless

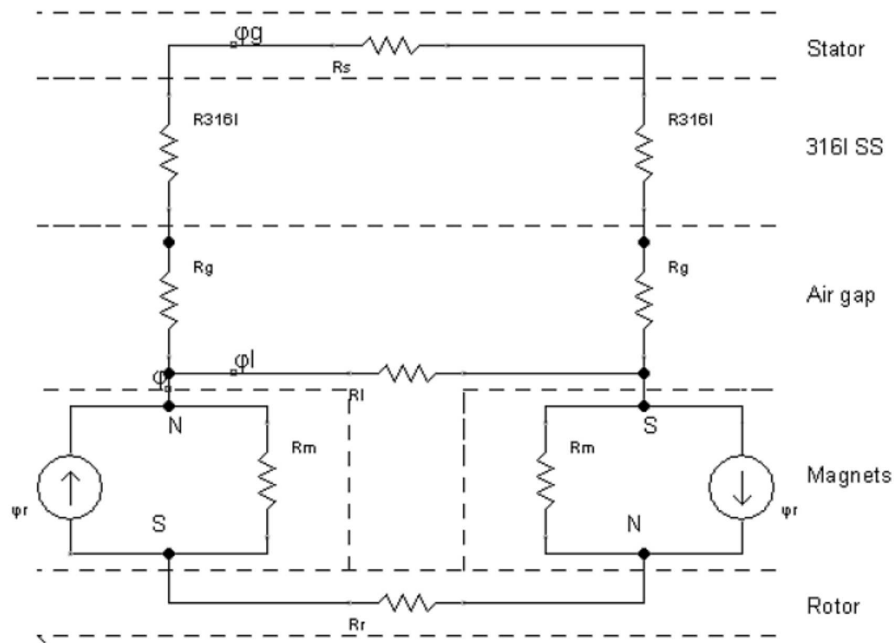


**Figure 3.8:** Equivalent magnetic model circuit of the configuration shown in Figure 3.7

Steel with reluctance  $R_{316L}$  and afterwards through the stator. There is also a small leakage flux  $\phi_l$  between the magnets.

This model can be further simplified by applying the following assumptions [13]:

- (i) The right magnet and rotor reluctance can be swapped because they are in series
- (ii) The air gap flux can be calculated as  $\phi_g = K_l \phi_r$  with  $K_l$  the leakage factor typically between  $0.9 \leq K_l \leq 1.0$
- (iii) The magnets can be combined as one
- (iv) The reluctance of the rotor and the stator is low compared to the other reluctances. They can be eliminated by using a reluctance factor  $K_r$  which increases the air gap- and 316L reluctance, with  $K_r$  typically between  $1.0 \leq K_r \leq 1.2$

Which equates to the simplified magnetic circuit shown in Figure 3.9. Using the electrical circuit analogy, this circuit can be solved with current division between resistors. The solution of this circuit is

$$\phi = \frac{2R_m}{2R_m + 2K_r(R_g + R_{316L})} \phi_r = \frac{1}{1 + K_r \frac{R_g + R_{316L}}{R_m}} \phi_r \quad (3.9)$$

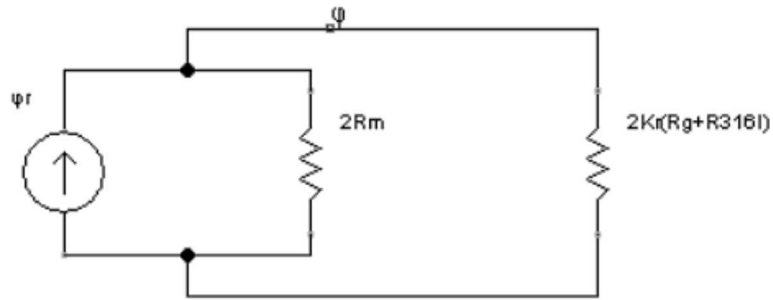


**Figure 3.9:** Simplified magnetic circuit

where

$$\left\{ \begin{array}{l} \phi_g = K_I \phi_r \quad (3.10a) \\ R_m = \frac{l_m}{\mu_R \mu_0 A_m} \quad (3.10b) \\ R_g = \frac{g}{\mu_0 A_g} \quad (3.10c) \\ R_{316L} = \frac{l_{316L}}{\mu_{316L} \mu_0 A_{316L}} \quad (3.10d) \end{array} \right.$$

with  $l_m$ ,  $g$ ,  $l_{316L}$  being the lengths of the magnet, air gap and 316L respectively.

Combining Eq. 3.7, 3.8, 3.9 and 3.10 the air gap flux density can be calculated with

$$B_g = \frac{K_I \frac{A_m}{A_g}}{1 + K_r \frac{\mu_R}{\mu_0}} B_r \quad (3.11)$$

After determining the air gap flux density  $B_g$  for one half of a north pole and one half of a south pole using the magnetic circuit, the amplitude of the torque  $|T|$  can be calculated using Eq.3.12.

$$|T| = 2NB_g L_{st} R_{r0} i \quad (3.12)$$

This expression determines the torque produced by a current  $i$  flowing through the coils. With  $B_g$  the air gap flux density,  $L_{st}$  the axial length of the motor and  $R_{r0}$  the air gap radius.

### 3.4.3 Comparison

The two motion methods are compared in Table 3.1. This comparison helps in choosing the most optimal method.

**Table 3.1** Comparison between the mechanical drive and magnetic drive

	Mechanical drive	Magnetic drive
Propulsion	Belt and pulley	PM-motor
Required load torque	0,017 Nm <sup>1</sup>	
Motor RPM	300 min <sup>-1</sup>	1-10 min <sup>-1</sup>
Gearbox	Yes (100:1)	No
Efficiency	50-70%	low
Exit port shape	Conical	
Maximum working temperature	200 °C	150 °C
Limiting component	Bearings	Magnets
Number of bearings	2	
Airtight	Sufficient	
Sealing	Radial shaft seals	Closed housing
Total length	140 mm	110 mm
Estimated cost additional components	€100	€900
Estimated cost material	€150	€130
Total	€250	€1030

As you can see there are some similarities and some differences between both driving methods. The most important differences are discussed because they determine which method is the most suitable for this application:

- *Efficiency*: The efficiency of the mechanical drive is between 50-70%. This is mainly due to the use of a gearbox. This use of a gearbox is not possible in the magnetic drive configuration. This means that the PM-motor, a servo-motor, itself has to rotate at very low velocities which has a low efficiency as a result.
- *Sealing*: The rotational motion of the mechanical drive on the inside of the static housing is driven by a belt and pulley with a motor placed on the outside of the hub. Therefore, a gap in the housing must be provided to allow the belt to drive the mechanism. Consequently, the housing is not airtight anymore and requires sealings to prevent excessive Hydrogen leakage. This is not necessary with the magnetic drive because a fully closed housing is possible.
- *Total estimated cost*: This is the defining factor for the selection of the propulsion method. The estimated cost of the magnetic drive is a lot higher than the cost of the mechanical drive. This is mainly due to the cost of the actual PM-motor and a stepper motor being already present in the lab.

As a result of this comparison it is clear that the mechanical drive is the most suitable to use as the propulsion method for the application and thus will be considered in this thesis.

<sup>1</sup>See section 4.1 for this calculation

### 3.5 Final Design

The design first proposed in section 3.2 underwent a lot of improvements and optimizations to eventually evolve into a final design. An overview of the different stages in the design process is shown in Figure 3.10. In stage 1 of the design process, the design could not operate in the entire set-up of the reactor due to not being able to attach subsequent components at the end of the mechanism. This was improved in stage 2 by introducing a tube that would rotate inside two fixed components, making it possible to attach other components downstream. However, these two fixed components were not connected to each other which would lead to alignment issues. In stage 3 this was optimized by rigidly connecting these fixed components, while in the meantime two motion methods to drive the hollow tube were simultaneously developed: a magnetic drive and a mechanical drive. After comparing these, the mechanical driven was chosen as motion method. This was then further optimized in stage 4 of the design process to eventually come to the final design.

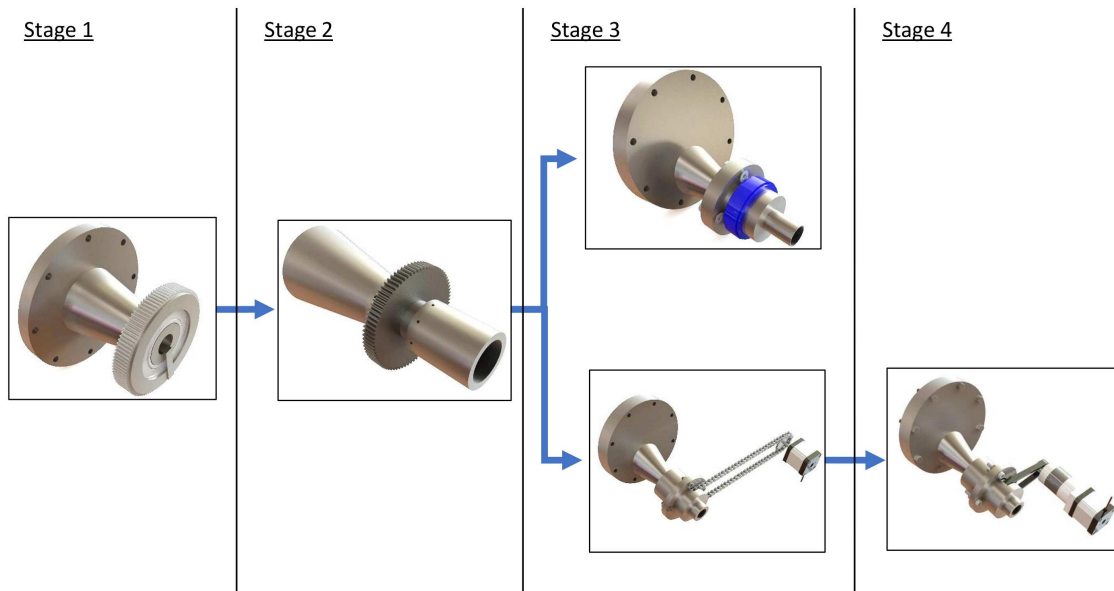


**Figure 3.10:** Overview of the design process evolution from preliminary design to final design

A detailed view of this final design is shown in Figure 3.4. The figure shows a half section-view of the assembly so that the components that are inside of the housing are visible.



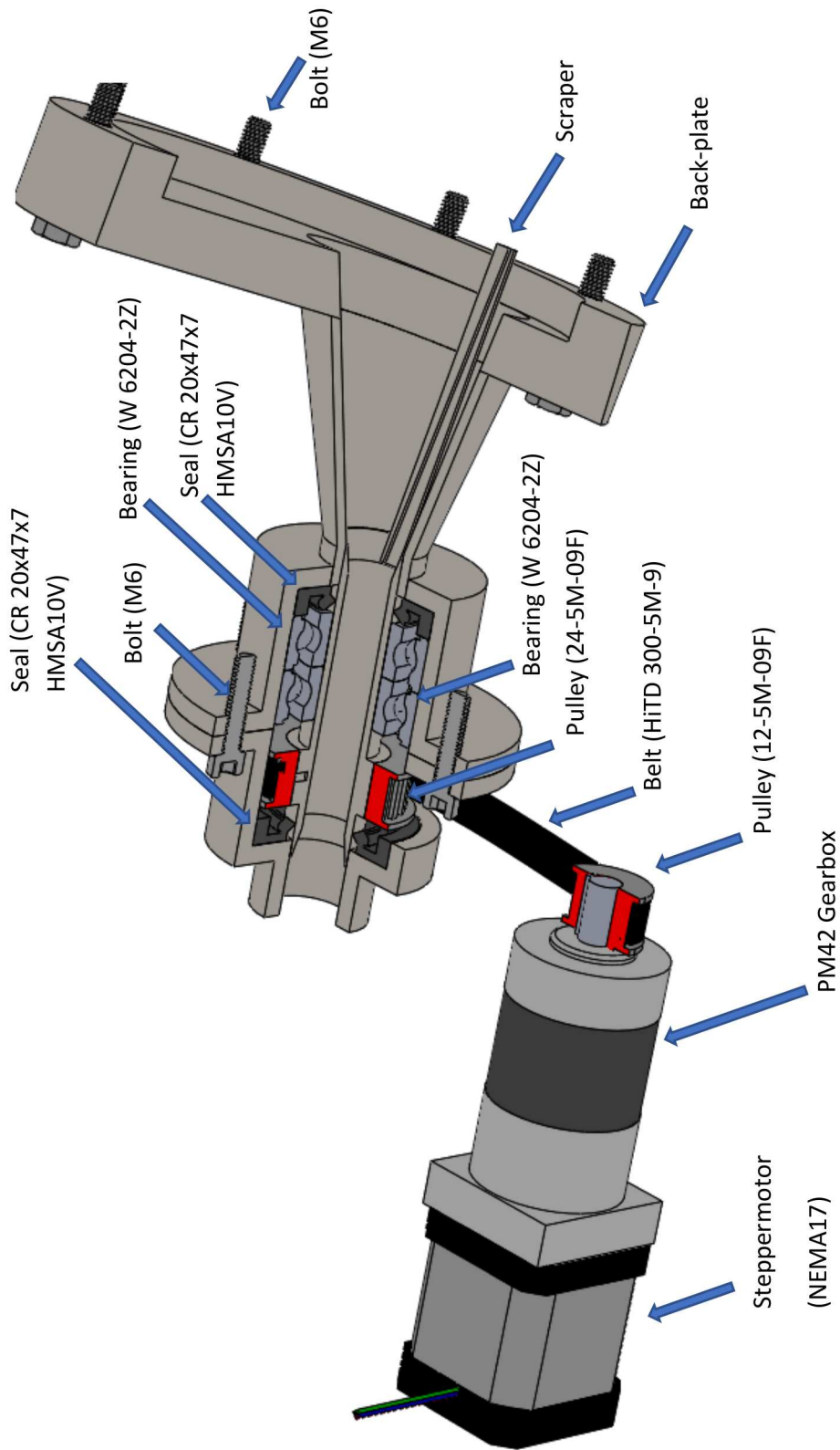


Figure 3.11: Overview of the final design assembly with every component labelled



## Chapter 4

# Numerical methodology

To determine the dimensions of the elements in the transmission line such as the motor, the belt and pulley, there are several parameters that must be known. These analysis are done manually, or with the help of numerical Computer Aided Engineering (CAE) software packets.

### 4.1 Load torque analysis

Starting from the end of the transmission line, the first calculation is to determine the cutting force needed to remove the actual deposit layer. Because there is little information about the actual carbon black powder on nano-scale, some simplifications have to be made, and will be included as some sort of safety factors. This means that the transmission line and power supply will be over-dimensioned.

#### 4.1.1 Tensile stress

Hartley et al. [15] developed a method for calculating the tensile stress of carbon black powder layers, with the Van der Waals force as main acting inter-particle force and factors like the packing density included. Many of the parameters used in their formula are not known for carbon black powder on nano-scale, produced by a solar reactor. And because no actual solar reactor is available, there are also no samples of carbon black with similar structure accessible for experiments in this thesis work.

However, in their paper, Hartley et al. [15] provide a lot of data about tensile stresses of commercial carbon blacks. Using that data, an approximate value of the tensile stress can be used for further calculations. By looking for powders with the same particle diameters and surface energy, the estimate can be made as accurate as possible. Rodat et al. [5] experimented on actual samples of carbon black from a solar reactor and concluded that the resulting surface energy  $S$  was between  $60 \text{ m}^2/\text{g}$  and  $100 \text{ m}^2/\text{g}$  and the mean particle diameter of carbon black produced by a solar cracking process should then be between  $33.3 \text{ nm}$  and  $55.6 \text{ nm}$  (see subsection 2.1.2).

Hartley et al. [15] mentioned a few commercial carbon blacks in their paper that lie between both

the limits of particle diameter and those of surface area, listed in Table 4.1. Those include: Regal 300 R, Regal 300 I, Elftex 8 and Vulcan 3.

**Table 4.1** Physical properties of carbon black (modified from [15])

Material	Source	Form	Surface area [m <sup>2</sup> /g]	Particle diameter [μm]	DBPA [cm <sup>3</sup> /100g]
Regal 300 R	Cabot Corp.	fluffy	69.7	0.037	84
Regal 300 I	Cabot Corp.	pelletized	74.5	0.043	71
Elftex 8	Cabot Corp.	fluffy	59.9	0.043	101
Monarch 900	Cabot Corp.	fluffy	257	0.018	69
Sterling R	Cabot Corp.	fluffy	27.9	0.069	73
Vulcan 3	Cabot Corp.	pelletized	77.5	0.047	106
N299	Huber Corp.	pelletized	111	0.028	105
N650	Huber Corp.	pelletized	38	0.075	86
N660	Huber Corp.	pelletized	34	0.071	73
AR060	Huber Corp.	pelletized	24	0.1	55

Referring to these four types of commercial carbon black, Regal 300 I has the largest tensile stress for a certain packing density [15]. While it is unknown which packing density should be considered in the case of solar thermal methane cracking, it is safest to take this maximum value and have an extra safety factor covered. Also, with the values and the resulting forces so small, the over dimension of the power should not be an issue. The tensile stress  $\sigma$  then becomes 225.4 g/cm or 0.02254 N/mm<sup>2</sup>.

#### 4.1.2 Torque

The torque needed to remove a layer of carbon deposition can be found from the tensile stress. According to Mohr's circle, the maximum shear stress  $\tau$  is half the tensile stress, which comes at 0.01127 N/mm<sup>2</sup>. The exact thickness of the deposit layer being removed is variable, but for safety reasons the maximum possible will again be considered. This means the area of the attacking side of the scraper can be multiplied by the shear stress to find the force acting on this surface, or rather the force that has to be created to remove the deposit layer. With a length  $l$  of 80 mm and a height  $h$  of 1 mm the area thus becomes 80 mm<sup>2</sup> by solving Eq. 4.1. The resulting force  $F$  on the entire surface area of the scraper is 0.9016 N.

$$F = \tau lh \quad (4.1)$$

The necessary torque to provide this force is found with Eq. 4.2. The radius  $r$  from the circular motion to the centerline of the motion increases for a conical shape. In Figure 4.1, a sketch of the cone is drawn with the scraper included. Force  $F$  is working in or out the plane in the middle of its surface. Diameter of the motion of the center of the area varies from 8.50 mm to 28.50 mm. Because the force will work in the middle of the area, a radius  $r$  of 18.50 mm is chosen. Solving

Eq. 4.2 results with Torque  $T$  of 0.0166796 Nm.

$$T = Fr \quad (4.2)$$

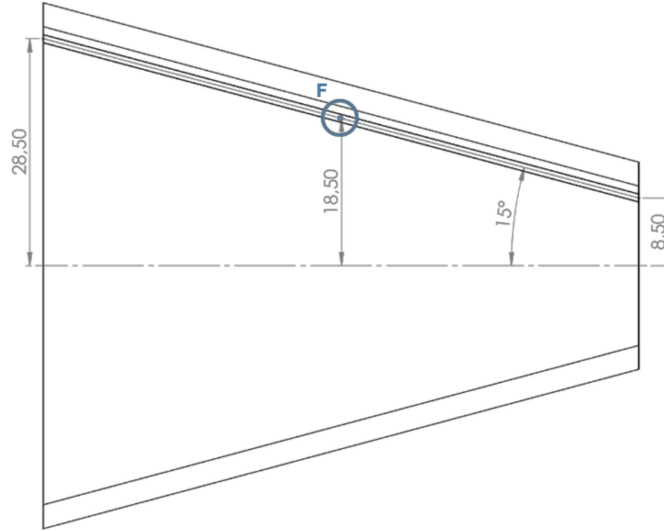


Figure 4.1: Force  $F$  exerted on the scraper surface at radius  $r$

## 4.2 Static analysis

The static analysis is performed on the scraper. The scraper is considered as a critical part in the assembly due to its dimensions and the load that acts on it: it is a long and slim beam-like structure on which the force that is necessary to remove the carbon particles from the walls acts. The static analysis is performed to check if the displacement of the scraper is within acceptable limits and that the stresses do not exceed the elasticity limits. The analysis will be performed using the software Siemens NX12. The software provides tools for finite element modelling and result visualization that can be used to perform initial design validation studies. The Solution Type chosen for this analysis was SOL 101 Linear Statics- Global Constraints.

### 4.2.1 Governing equations

Finite element method (FEM) is used to perform structural analysis on complex structures. Governing equations are approximated using a set of simultaneous algebraic equations. These structures are also discretized in a finite number of small and simple elements such as 1D: beams; 2D: triangles, quadrilaterals; 3D: tetrahedrons, hexahedrons, pentahedrons. For one element this algebraic equations can be represented as [32]

$$\{f^E\} = [K^E]\{u^E\} \quad (4.3)$$

where  $\{f^E\}$  is the force vector acting on the node,  $[K^E]$  the elemental stiffness matrix and  $\{u^E\}$  the displacement vector of the node. The elemental equations can then be combined using continuity

equations (the material does not tear or overlap) to form the master stiffness matrix for the entire structure

$$\{f\} = [K]\{u\} \quad (4.4)$$

where  $[K]$  is the symmetric global stiffness matrix consisting of the stiffness coefficients. For elastic structural analysis this matrix is considered constant, it can however be a singular equation, i.e. it has no matrix inverse. This is solved by applying boundary conditions to the structure so that  $[K]$  becomes non-singular [32]. In Eq. 4.4  $\{f\}$  is an action (force) and  $[K]$  is a property (stiffness) which are both known. The unknown behaviour (the displacement vector  $\{u\}$ ) can be calculated using

$$\{u\} = [K]^{-1}\{f\} \quad (4.5)$$

due to  $[K]$  being a non-singular matrix. Using the stress-strain relations for linear elastic materials it is now possible to calculate the stress and strain of the nodes from the displacement vector.

### 4.2.2 Strategy

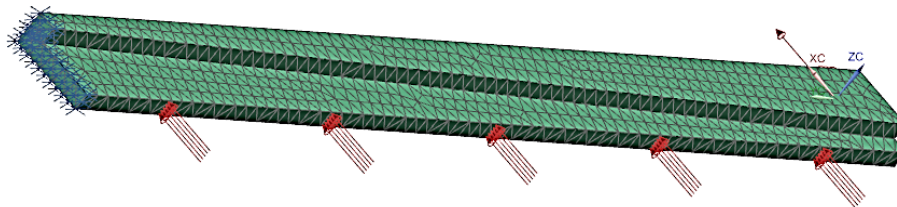
The simulation must be set-up in a way that it accurately represents how the part functions in real life. To do so, four parameters have to be defined:

- (a) *Constraints* - The constraints applied to the model should represent how the movement of the scraper is limited in reality. In this application, the scraper is welded to the driven pipe by welding each side of the scraper to the rectangular flat face present on the driven pipe. This can be simulated by removing the first 5 mm (length of the rectangular flat face) of the scraper that is rigidly connected to the pipe and fixing the surface.
- (b) *Loads* - The main load that acts on the scraper is the force that is necessary to remove the carbon particles from the walls. This was calculated in subsection 4.1.2 to be a distributed load of 0.9016 N over the surface.  
The effects of gravity due to the mass of the scraper can also be implemented in the simulation. The worst-case scenario is when both the load and the gravitational force act in the same direction on the scraper. This occurs when the scraper is rotating upwards and is at a 90° angle.
- (c) *Material* - The material that is used in this simulation is AISI Type 316L Stainless Steel, annealed bar. The necessary properties of this material are given in Table 4.2
- (d) *Mesh* - A 3D tetrahedral mesh with element size of 1 mm is chosen to discretize the model so that it can be used for finite element analysis.

**Table 4.2** Material properties of AISI Type 316L Stainless Steel, annealed bar

Material properties	
Density	8 g/mm <sup>3</sup>
Modulus of Elasticity	193 GPa
Tensile Strength, Yield	205 MPa
Tensile Strength, Ultimate	515 MPa
Poisson Modulus	0.28
Shear Modulus	78 GPa

Figure 4.2 shows the resulting model that can now be used to perform the static analysis. The length of this model has been reduced with 5 mm to account for the rigidly welded part of the scraper to the driven pipe. The constraints are represented by the blue arrows, the loads (removal force and gravity) are represented by the red arrows and the mesh distribution is visible.

**Figure 4.2:** Resulting model that is used to perform the static analysis

### 4.2.3 Manual calculation

Because the Finite Element Analysis (FEA) package is like a black box that generates results regardless whether these results are possible in practice, a manual calculation is performed prior to the FEA. Although the formulas used require a lot of simplifications of the actual structure, they will provide an approximation of the magnitude of the results that are to be expected from the computational analysis. Manual calculation also ensures in-depth understanding of the physics behind and builds foundation to technically judge the quality of FEA results.

In this application, the scraper can be simplified to a clamped beam with a distributed load  $w_a$ . The simplified beam has the following dimensions:  $L = 77$  mm to account for the welded part,  $b = 1.5$  mm and  $h = 5$  mm. In Roark et al. [33] equations for the maximum value of deformations of a beam can be found. The end constraints of this structure are left end free, right end fixed (cantilever) as represented in Figure 4.3. For a uniform load on an entire beam ( $a = 0$  and  $w_a = w_l$ ) the maximum deformation  $y_a$  can be calculated using

$$y_a = \frac{-w_a L^4}{8EI} \quad (4.6)$$

where  $E$  the elasticity modulus (see Table 4.2) and  $I$  the moment of inertia of the beam. This equation yields a maximum deformation of 0.017 mm.

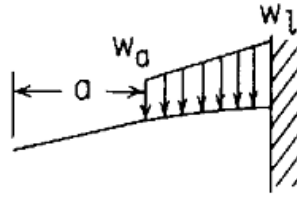


Figure 4.3: End constraints of the used beam model

#### 4.2.4 Results of FEA

The maximum displacement and maximum stress were calculated using this simulation. Figures 4.4a to 4.4c show the obtained results for the displacement in magnitude, along the x-axis and along the z-axis. The maximum values were respectively 0.036 mm, 0.024 mm and 0.027 mm. The maximum displacements are very small as expected due to the small force, and well within acceptable limits for this application.

Figure 4.4d shows the Von Mises stress with a maximum value of 11.8 MPa at the base of the scraper. This stress is also well below the elasticity limit. Based on this structural analysis it can be concluded that the mechanical properties of the scraper are appropriate for this application.

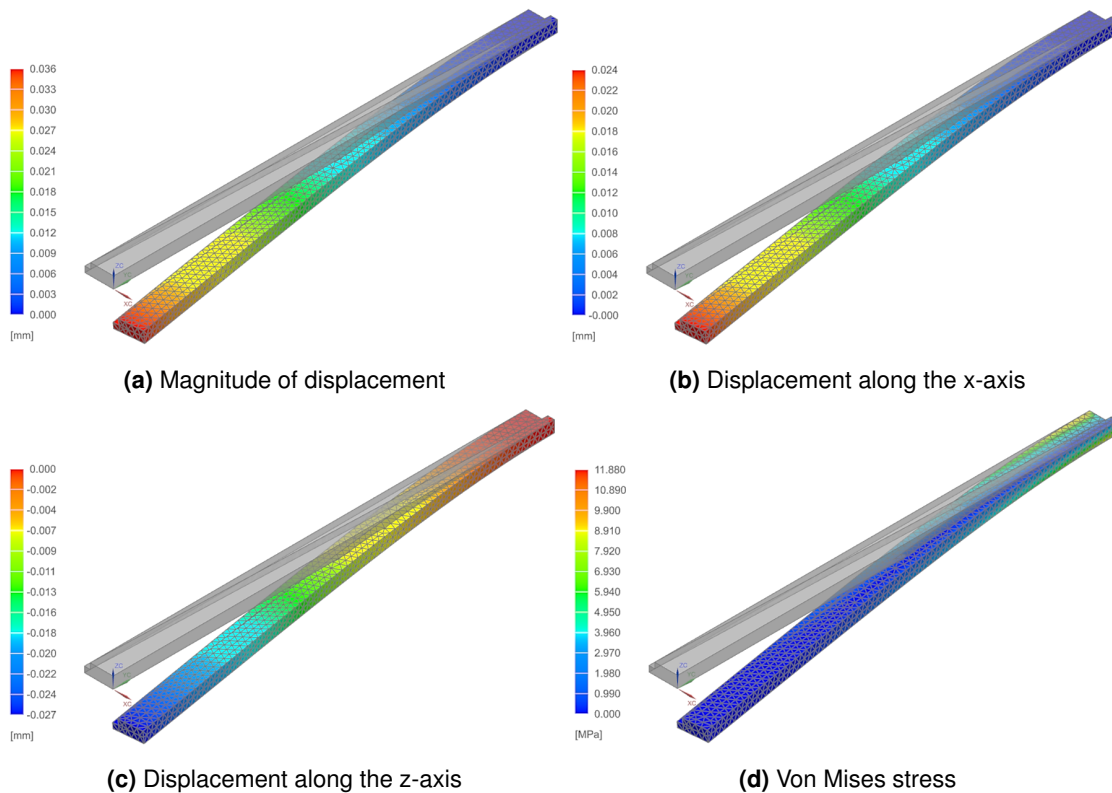


Figure 4.4: Results of the static analysis



### 4.3 Dynamic Analysis

The dynamic analysis is also performed on the scraper. Again, due to its shape it is vulnerable to vibrations caused by the rotational motion of the scraper. The software Siemens NX12 is used with solution type SOL 103 Real Eigenvalues. This solution type allows to find the frequencies that should be avoided during operation due to the large excitations of the structure, even with minimal force. It also tells how the structure will deform at these natural frequencies (mode-shape) and where the structure is straining the most at that frequency.

#### 4.3.1 Governing equations

A dynamic analysis takes the mass of the structure into consideration. When the structure can be considered linear, the starting point to investigate the response is the Equation of Motion (EoM) for the dynamic behavior of a structure given by Eq.4.7 [34].

$$[M]\{\ddot{u}\} + [C]\{\dot{u}\} + [K]\{u\} = \{f\} \quad (4.7)$$

where  $[M]$  is the mass-matrix,  $[C]$  is the damping-matrix and  $[K]$  the stiffness matrix. In linear dynamics, these three matrices are considered constant.  $\{\ddot{u}\}$ ,  $\{\dot{u}\}$ ,  $\{u\}$  and  $\{f\}$  are respectively the acceleration vector, the velocity vector, the displacement vector and load vector, respectively, which are a function of time.

To find out how a structure wants to respond, the eigenvalue problem has to be solved. This will give the eigenvalues or natural frequencies of the structure. It is solved by considering undamped free vibrations. Eq.4.7 now becomes

$$[M]\{\ddot{u}\} + [K]\{u\} = 0 \quad (4.8)$$

Solutions of Eq. 4.8 have the form

$$\{u\}(t) = \{U\}.e^{j\omega t} \quad (4.9)$$

with  $\{U\}$  being a constant vector and  $e^{j\omega t}$  representing the time-response.

Knowing this, Eq. 4.10 is obtained

$$([K] - \omega^2[M])\{U\} = \{0\} \quad (4.10)$$

By solving this equation to find the non-trivial solution (i.e.,  $U \neq 0$ ) a value for  $\omega^2$  is obtained with a corresponding vector  $\{U\}$ . This vector can be scaled by any real number (i.e.,  $\alpha\{U\}$ ) and will still be a solution to Eq. 4.10. This vector  $\{U\}$  therefore solely represents the mode-shape of the structure at frequency  $\omega$  and not the actual magnitude of the vibration response (the magnitude depends on the applied force) [34].

#### 4.3.2 Results

The result of this dynamic analysis are the different mode shapes with their frequency of the structure. The modal frequencies are shown in Table 4.3. These frequencies should be avoided at all

cost during operation because the structure will oscillate even in the absence of an external force.

**Table 4.3** Result of the dynamic analysis showing the first nine modes with their corresponding frequency

Mode	Frequency (Hz)
1	192.62
2	602.52
3	1381.76
4	3828.37
5	3984.58
6	4468.89
7	7834.86
8	10592
9	12837.9

The mode-shapes corresponding with each of the modal frequencies are shown in Figures 4.5a to 4.5i. As you can see the first modal frequency is at 192.62 Hz.

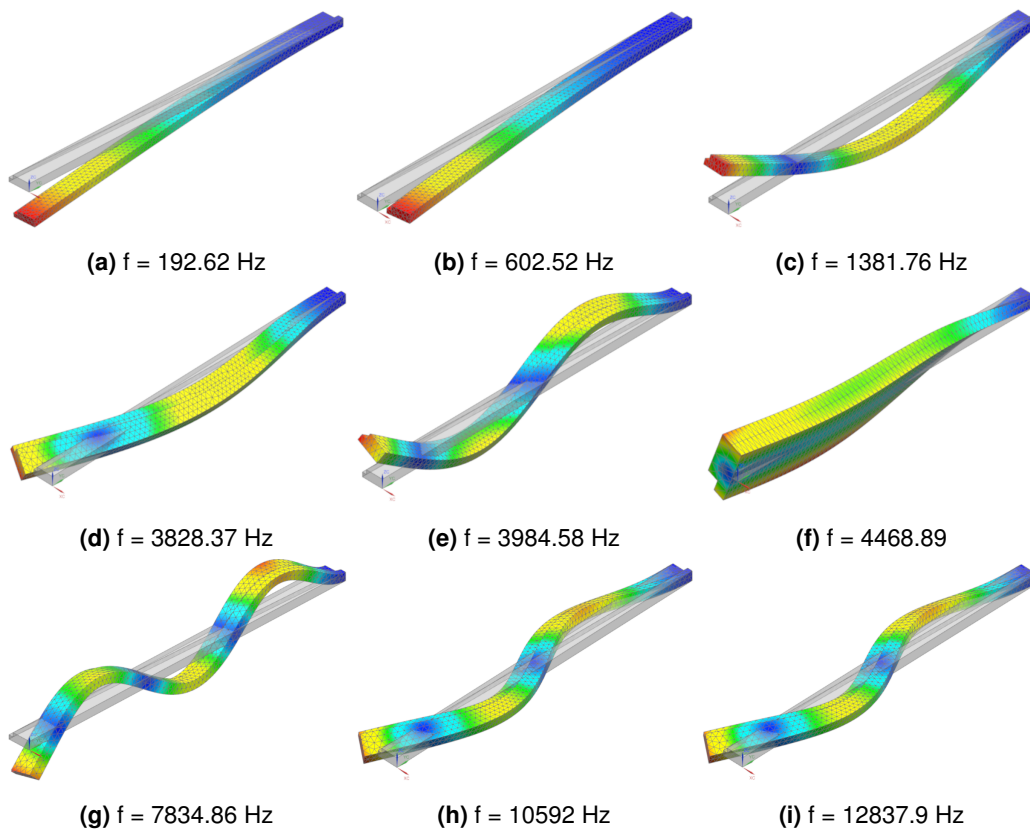


**Figure 4.5:** The mode-shapes at each of these modal frequencies

Since the rotational velocity is only around 1 RPM, the results of this analysis show that there will be no problem during operation with the natural frequencies of the scraper.

## 4.4 Heat transfer analysis

As discussed in subsection 3.3.2 a cooling mechanism is a necessity in this design. It was made clear that a simple solution is required because of the complexity of the previously designed parts. Therefore, a set-up was chosen where simple copper tubes are wrapped spirally around the conical exhaust, and if necessary even the housing. To increase heat transfer from the exhaust to the cooling canals, a copper bond was added in between via a process called 'MIG brazing'. This section includes the numerical calculations to explore this cooling solution and its viability. Also, certain parameters from the cooling fluid and dimensions from the set-up will be determined for this specific case.

### 4.4.1 Strategy

To calculate the heat transfer from the reactor exhaust to the cooling fluid as accurate as possible without using any CFD software, a slightly simplified model will be used. The complex spiral shape of the cooling canals shown in Figure 4.6 (a) are approximated by multiple closed circular channels. The conical exhaust is then split up in the same number of cylindrical rings. The result can be seen in Figure 4.6 (b). This simplifies the model to a heat transfer problem for multiple cylindrical exhausts or pipes. To account for the small contact area between the outer exhaust wall and the cooling channel wall, this part of the calculations will be based on flat-plate solar collectors. This is accomplished by unfolding the separate rings with the accompanying cooling channel, which can be seen on Figure 4.6 (c).

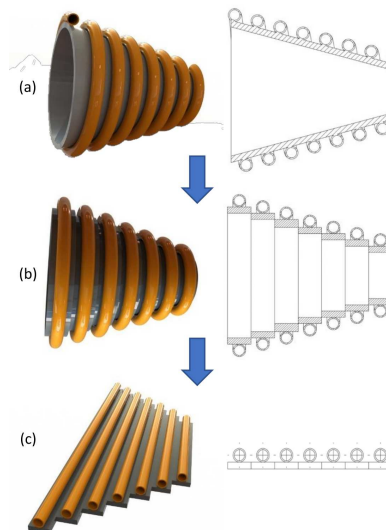


**Figure 4.6:** (a) Complex spiral shape of the channels, (b) discretization to circular channels, (c) unfolding of these circular channels

Calculations are done separately for every ring where the resulting values of the previous ring are used for the next. This is done to keep the model as close as possible to the reality. In Figure

4.7, one of these steps is shown where the temperature of the outgoing cooling fluid and the temperature of the outgoing hydrogen gas are used for the next iteration. Another consequence of this iterative approach is that some constants and design parameters will have to be re-determined for every ring. For example, the velocity of the hydrogen gas will change throughout the different cylinders, because the mass flow is constant but the cross section of the cylindrical rings is smaller for every iteration.

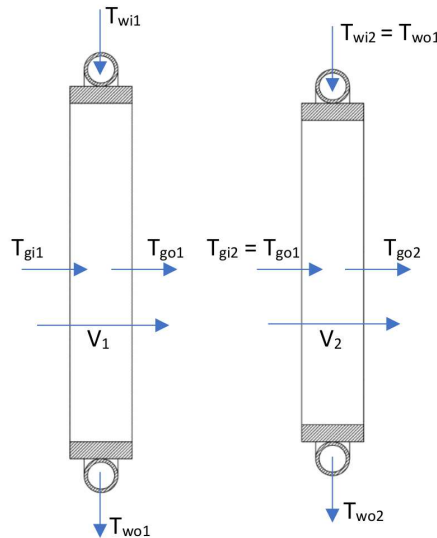


**Figure 4.7:** Schematic overview of the parameters used for each ring

It is important to note that for the entirety of these calculations, the exhaust gas will be considered as a stream of pure hydrogen. In real circumstances, the exhaust gases will exist of not only hydrogen, but also small volumes of remaining natural gas and of course also carbon black quantities. Taking the other substances into account would highly increase the complexity of the problem and are therefore neglected in this calculation.

#### 4.4.2 Governing equations

Before covering the analysis for this exact case, the governing equations for this strategy are discussed. In Figure 4.6 (c) the similarity of this problem with heat transfer in flat-plate solar collectors was shown. This means an equal method can be used to calculate the actual heat transfer through the different layers. When considering only one of the exhaust rings which is then unfolded into a flat plate with a single straight cooling tube, the situation can be portrayed as in Figure 4.8. Arvind and Shyam [14] used a similar method in their book for the flat-plate solar collector from which the used equations and formulas are derived.

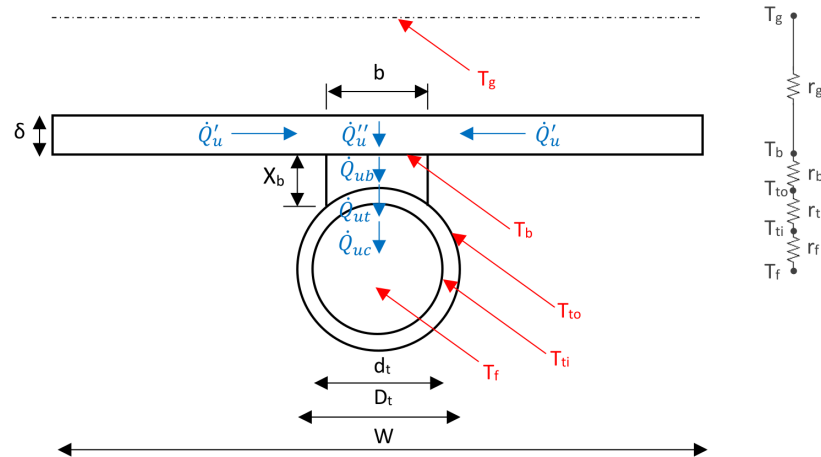


Figure 4.8: Heat transfer in a flat-plate solar collector (Modified from [14])

Firstly, the heat transfer  $\dot{Q}'_u$  is determined through the flat plate up to the part of the cross section where the cooling channel is attached via the bond. Heat input on this plate only includes convective heat from the exhaust gases. Heat losses are the conductive heat loss to the insulation material followed by the convective heat loss to the ambient air. This all is brought together in Eq. 4.14, used for flat-plate solar collectors where a fin efficiency is considered as well. This fin efficiency factor is given as

$$F = \frac{\tanh \frac{m(W-D_t)}{2}}{\frac{m(W-D_t)}{2}} \quad (4.11)$$

and

$$m^2 = \frac{U_L}{k_e \delta} \quad (4.12)$$

where  $W$  is the tube pitch,  $D_t$  is the copper tube's outer diameter,  $U_L$  is the heat transfer coefficient that describes the heat losses,  $\delta$  and  $k_e$  are respectively the plate thickness and the thermal conductivity coefficient of the plate, or exhaust wall in this instance. The plate thickness in this case will be the wall thickness of the exhaust. The loss coefficient  $U_L$  is the sum of the losses from the top of the plate, the edges of the plate and the back of the plate. Both the top and the edge losses are not present for this application which means that  $U_L$  consists only of the back losses  $U_b$  through the insulation which is calculated by

$$U_L = U_i = \left[ \frac{X_i}{k_i} + \frac{1}{h_i} \right]^{-1} \quad (4.13)$$

where  $X_i$  and  $k_i$  are respectively the thickness and thermal conductivity of the insulation material wrapped around the exhaust with cooling canals, and  $h_i$  is the convective heat transfer coefficient between the insulation material and the ambient air. The calculation of the latter coefficient will be discussed in subsection 4.4.3, together with other convective heat transfer coefficients.

A few important assumptions had to be made to come to this fin efficiency factor [14]:

- (i) the bottom surface of the absorber plate and tubes are perfectly insulated;
- (ii) the tubes are brazed onto the plate as discussed in subsection 3.3.2;
- (iii) the bond has thermal conductivity  $k_b$ , which also accounts for a poor joint;
- (iv) the thermal inertia effects can be neglected under steady-state conditions.

Taking these assumption into account, now the heat transfer trough the plate up to the bond area can be calculated using the fin efficiency factor with

$$\dot{Q}'_u = (W - b)L_c F [q_c - U_L(T_b - T_a)] \quad (4.14)$$

where  $b$  is the bond breadth,  $q_c$  is the convective heat input from the exhaust gases,  $T_b$  is the bulk temperature of the base of the fin, and  $T_a$  is the temperature of the ambient air. The characteristic length  $L_c$  for this specific instance is simply the circumference of the middle of the exhaust ring cross section. The convective heat input  $q_c$  from Eq. 4.14 is the heat transfer from the hot exhaust gases to the exhaust cone wall and is calculated by

$$q_c = h_g(T_g - T_b) \quad (4.15)$$

where  $h_g$  is the convective heat transfer coefficient from the exhaust gas to the exhaust wall, and  $T_g$  is the bulk temperature of the exhaust gases at a distance far enough from the exhaust walls. Eq. 4.14 considered the convective heat input on the plate except for the region where the cooling canals are joint with the bonds. The rate of heat transfer through the part of the fin directly above the bond is calculated by

$$\dot{Q}''_u = bL_c [q_c - U_L(T_b - T_a)] \quad (4.16)$$

with the same expression for the characteristic length as used in Eq. 4.14. The total rate of heat transfer  $\dot{Q}_u$  from the hot exhaust gases up to the bond is now simply calculated as the sum of Eq. 4.14 and Eq. 4.16.

$$\dot{Q}_u = \dot{Q}'_u + \dot{Q}''_u = L_c [(W - b)F + b] [q_c - U_L(T_b - T_a)] \quad (4.17)$$

or when including Eq. 4.15

$$\dot{Q}_u = L_c [(W - b)F + b] [h_g T_g + U_L T_a - (h_g - U_L) T_b] \quad (4.18)$$

or

$$\dot{Q}_u = \frac{[h_g T_g / (h_g - U_L) + U_L T_a / (h_g - U_L) - T_b]}{r_g} \quad (4.19)$$

where

$$r_g = \frac{1}{L_c [(W - b)F + b] (h_g - U_L)} \quad (4.20)$$

The heat transfer through the bond itself can be found by

$$\dot{Q}_{ub} = (T_b - T_{to})bL_c\left(\frac{k_b}{X_b}\right) = (T_b - T_{to})/r_b \quad (4.21)$$

where  $T_{to}$  is the temperature at the border of the bond and the outside wall of the cooling tube,  $L_c$  and  $X_b$  are respectively the characteristic length and the mean thickness of the bond. Here, the characteristic length equals to the length of the bond, which is the circumference of it around the exhaust ring. The heat conduction through the copper tube wall is

$$\dot{Q}_{ut} = (T_{to} - T_{ti})\pi A_{mw}L_c\left(\frac{k_t}{X_t}\right) = (T_{to} - T_{ti})/r_t \quad (4.22)$$

where  $T_{ti}$  is the temperature at the inner wall of the copper cooling tube,  $k_{Cu}$  and  $X_t$  are respectively the thermal conductivity and the thickness of the copper wall of the cooling canal, and  $A_{mw}$  is the mean wall area to account for the heat transfer happening only on one side of the tube. The characteristic length  $L_c$  for this case is the circumference of the center of the cooling tube or just the length of the tube. This mean wall area is determined by

$$A_{mw} = \frac{D_t - d_t}{\ln \frac{D_t}{d_t}} \quad (4.23)$$

where  $d_t$  is the inner diameter of the copper cooling tube.

Lastly, the convective heat transfer from the cooling tube to the cooling fluid can be calculated from

$$\dot{Q}_{uc} = (T_{ti} - T_f)\pi d_t L_c h_f = (T_{ti} - T_f)/r_f \quad (4.24)$$

where  $T_f$  is the bulk mean fluid temperature of the cooling fluid, and  $h_f$  the convective heat transfer coefficient from the tube wall to the cooling fluid.  $L_c$  is the same here as for Eq. 4.22.

Combining Eq. 4.19 with Eq. 4.21, Eq. 4.22 and Eq. 4.24 results in

$$\dot{Q} = \frac{\frac{h_g}{h_g - U_L} T_g + \frac{U_L}{h_g - U_L} T_a - T_f}{(r_g + r_b + r_t + r_f)} \quad (4.25)$$

The value for  $\dot{Q}$  gives the total value of heat transferred from the exhaust gas to the cooling fluid, and represents the heat lost from the exhaust gas. This means the final gas temperature at the outlet of each exhaust ring can be calculated with

$$\dot{Q} = \dot{m} c_p \Delta T \quad (4.26)$$

which can be rearranged to

$$T_{go} = T_{gi} - \frac{\dot{Q}}{\dot{V} \rho c_p} \quad (4.27)$$

where  $\dot{m}$  is the mass flow rate. The same principle can be used to determine the outlet temperature of the cooling fluid.

### 4.4.3 Convective heat transfer coefficients

For the calculation of heat transfer from hydrogen exhaust gas to cooling fluid, only conduction and convection are considered. The external radiative heat losses are negligible in contrast to the high temperatures of the hydrogen gas, meaning only thermal conductivity coefficients and convective heat transfer coefficients must be determined. The thermal conductivity can be found in data tables or temperature dependent expressions and polynomials, discussed further in subsection 4.4.4. Convective heat transfer coefficients however are more complex to determine, thus the overall strategy will be discussed in this paragraph. Cengel and Ghajar [35] described several formulas and equations in their book that will be used to calculate the needed coefficients.

Three different convective heat transfer coefficients are needed. There are two for the forced internal convective heat transfer from the hydrogen gas to the 316L stainless steel walls of the conical exhaust and from the cooling fluid to the copper cooling channels. A third one is needed for the natural convection between de ambient air and the insulation on the outside of the conical exhaust. In convection studies these coefficients are usually determined by evaluating the following equation for the convective heat transfer coefficient  $h$ :

$$Nu = \frac{hL_c}{k} \quad (4.28)$$

where  $Nu$  is the dimensionless Nusselt number,  $k$  is the thermal conductivity of the fluid, and  $L_c$  is the characteristic length. The characteristic length and the Nusselt number depend on the specific case of convection and thus will be discussed separately.

#### Forced internal convective heat transfer in the exhaust

Two cases of forced internal convection can be distinguished. The first one handles the heat transfer from the exhaust gas to the exhaust walls, while the second case covers the heat transfer from the cooling tube to the cooling fluid. For both instances the characteristic length  $L_c$  equals the inner diameter of the corresponding tube. The temperature at which the constants and coefficients needed to calculate the convective heat transfer coefficient is the bulk mean fluid temperature. This is the arithmetic average of the mean temperature at the inlet and outlet given by  $T_b = (T_i + T_o)/2$ . The mean temperatures for both inlet and outlet are a compensation for the temperature difference between the center of the cylinder and the wall. Because this temperature difference is very small over the film layer, the mean temperatures will be approximated by the temperature at the center of the tube, and thus  $T_b$  will determine the constants.

Although calculating the Nusselt number happens in a similar way for both cases, the parameters and constants used will be different. To determine the Nusselt number for forced internal convection, information is needed about the flow conditions. The flow can be turbulent or laminar, which can be defined by determining the Reynolds number. For flow in a circular tube this can be found from

$$Re = \frac{\dot{x}d}{\nu} = \frac{\rho\dot{x}d}{\mu} = \frac{4\rho\dot{V}d}{\mu d^2\pi} = \frac{4\rho\dot{V}}{\mu d\pi} \quad (4.29)$$

Where  $\dot{x}$  is the flow velocity,  $d$  is the inner diameter of the tube or exhaust,  $\nu = \mu/\rho$  is the kinematic viscosity with  $\mu$  de dynamic viscosity and  $\rho$  the density, and  $\dot{V}$  the volumetric flow rate. When the



Reynolds number is below  $10^3$ , the flow is considered laminar and the Nusselt number is then found to be constant and equal to 4.36 for internal convection in a circular tube.

For turbulent forced internal flow however, a modified version of the more complex but accurate relation called the second Petukhov equation will be used to evaluate the Nusselt number

$$Nu = \frac{(f/8)RePr}{1.07 + 12.7(f/8)^{0.5}(Pr^{2/3} - 1)} \quad (4.30)$$

where  $Pr$  is the Prandtl number and  $f$  is a friction factor that can be calculated with the first Petukhov equation expressed as

$$f = (0.792 \ln Re - 1.64)^{-2} \quad (4.31)$$

Important to note is that Eq. 4.30 is only valid for  $0.5 \leq Pr \leq 2000$  and for  $10^3 \leq Re \leq 5.10^6$ . The dimensionless parameter Prandtl number is defined as

$$Pr = \frac{\mu c_p}{k} \quad (4.32)$$

where  $c_p$  is the specific heat at constant pressure.

The convective heat transfer coefficient can now be calculated by evaluating Eq. 4.30 and using this result in Eq. 4.28.

#### Natural convective heat transfer in the exhaust

Calculating the convective heat transfer coefficient for the natural convection from the insulation material to the ambient air differs slightly from the previous cases. The average Nusselt number over the entire surface of the isothermal horizontal cylinder is found from

$$Nu = \left\{ 0.6 + \frac{0.387 Ra^{1/4}}{\left[ 1 + \left( \frac{0.559}{Pr} \right)^{9/16} \right]^{4/9}} \right\} \quad (4.33)$$

where  $Ra$  is the Rayleigh number portraying the ratio of buoyancy forces and thermal and momentum diffusivities, given by  $Ra = GrPr$ . For Eq. 4.34 to be valid, the Rayleigh number has to be below or equal to  $10^{12}$ . The Prandtl number  $Pr$  is again calculated by using Eq. 4.32. The Grashof number  $Gr$  is given by

$$Gr = \frac{g\beta(T_s - T_a)L_c^3}{\nu^2} \quad (4.34)$$

where  $g$  is the gravitational acceleration,  $\beta$  is the coefficient of volume expansion given by  $1/T$  for ideal gases,  $T_s$  is the temperature of the surface and  $T_a$  is the temperature of the ambient air. The characteristic length  $L_c$  equals the diameter of the specific exhaust ring. By first evaluating Eq. 4.33 and then Eq. 4.28, the convective heat transfer coefficient can be determined.

#### 4.4.4 Temperature dependent properties

High temperature differences and multiple iterations certainly add to the complexity of this problem. Material and substance properties have to be evaluated at several points and even more temperatures. Working with temperature dependent expressions for those properties will prove to be very

useful. If no simple temperature dependent expression or polynomial function was available, then property tables were used for linear interpolation. However, many of the properties do not show linear behavior. Though by only using large tables with small temperature steps, the error is reduced as much as possible.

### Thermal conductivity coefficient

Thermal conductivity coefficients of the copper tubes, copper bond, the stainless steel 316L, and the glass wool insulation must be known for conductive heat transfer through these materials. This constant is also used in the calculation of convective heat transfer, thus must also be known for water, air and hydrogen. Table 4.4 shows an expression for every thermal conductivity, or a reference to the table if no expression was used.

**Table 4.4** Temperature dependent thermal conductivities

	Thermal conductivity [W/(mK)] for temperature T [K]	Source
Air	$k_a$ (Appendix C.2)	[36]
Cooling fluid	$k_f = 0.80201\left(\frac{T}{300}\right)^{-0.32} - 0.25992\left(\frac{T}{300}\right)^{-5.7} + 0.10024\left(\frac{T}{300}\right)^{-12} - 0.032005\left(\frac{T}{300}\right)^{-15} + 0.10024\left(\frac{T}{300}\right)^{-12} - 0.032005\left(\frac{T}{300}\right)^{-15}$	[37]
Copper	$k_t = k_b$ (Appendix C.4)	[38]
Isolation	$k_i$ (Appendix C.3)	[39]
Hydrogen	$k_g$ (Appendix C.1)	[40]
316L	$k_e = \left(0.1333 + 0.1727\left(\frac{T-273}{1000}\right) - 0.04335\left(\frac{T-273}{1000}\right)^2 + 0.0332\left(\frac{T-273}{1000}\right)^3\right) 10^2$	[41]

### Other fluid properties

Apart from the thermal conductivity and the convective heat transfer coefficient, there are a few more fluid properties that are needed at various temperatures. For all three fluids considered in this heat transfer problem, the density, the dynamic viscosity and the heat capacity are to be known. Water will be considered as the cooling fluid for this case, but can be changed for other cooling fluid if necessary. Needless to say, both hydrogen and air are invariable for this application. The properties are shown in Table 4.5.

**Table 4.5** Temperature dependent fluid properties

Density [kg/m <sup>3</sup> ] for temperature [K]		Source
Air	$\rho_a$ (Appendix C.2)	[36]
Cooling fluid	$\rho_f = 999.84 \left( \frac{1+1.46(\frac{T-273}{100})-0.02(\frac{T-273}{100})^2-0.03(\frac{T-273}{100})^3}{1+1.46(\frac{T-273}{100})+0.06(\frac{T-273}{100})^2} \right)$	[42]
Hydrogen	$\rho_g$ (Appendix C.1)	[40]
Dynamic viscosity [kg/ms] for temperature T [K]		
Air	$\mu_a$ (Appendix C.2)	[36]
Cooling fluid	$\mu_f = \left( 280.68(\frac{T}{300})^{-1.9} - 511.45(\frac{T}{300})^{-7.7} + 61.13(\frac{T}{300})^{-19.6} - 0.46(\frac{T}{300})^{-40} \right) 10^{-6}$	[37]
Hydrogen	$\mu_g$ (Appendix C.1)	[40]
Heat capacity [J/kgK] for temperature [K]		
Air	$c_{p,a}$ (Appendix C.2)	[36]
Cooling fluid	$c_{p,f} = \frac{10^3}{18.02} \left( -203.61 + 1523.29(\frac{T}{10^3}) - 3196.41(\frac{T}{10^3})^2 + 2474.46(\frac{T}{10^3})^3 + \frac{3.86}{(\frac{T}{10^3})^2} \right)$	[43]
Hydrogen	$c_{p,g} = \frac{10^3}{2.02} (29.11 - 0.19 * 10^{-2}T + 0.40 * 10^{-5}T^2 - 0.87 * 10^{-9}T^3)$	[44]

**Table 4.6** Design and geometry parameters for calculations

Parameter	Value
$T_{gi}$	773
$T_{fi}$	283
Amount of rings	7
Length of exhaust canal l	0.0447707 <sup>1</sup>
$W = l/r$	0.0064 <sup>1</sup>
$D_e$	0.0476 <sup>1</sup>
$u = W \tan(15^\circ)$	0.0034 <sup>1</sup>
$\delta$	0.003
$D_t$	0.006
$X_t$	0.0006
b	0.0048
$X_b$	0.0024
$V_g$	$1.667 \cdot 10^{-4}$
$V_f$	$5 \cdot 10^{-5}$

#### 4.4.5 Results

This section will cover an actual case of the cooling mechanism and evaluate the temperature of the exhaust gas and water at their corresponding exit port. Because no physical version has been manufactured, some geometry and design parameters will be chosen to get an overall idea of the

<sup>1</sup>These values can be determined using simple geometry concept

temperature drop throughout the exhaust. The case-specific parameters are given in Table 4.6.

This specific case of seven windings is calculated with the software packet MATLAB®. The scripts and function that were written to make this happen are added in Appendix C. Another simplification was done by eliminating the heat loss  $U_L$  through the isolation material. This loss will be negligible and not taking it into account will reduce the computing time considerably. The results are shown in Figure 4.9. An optimization loop is used so that for every ring the error converges to zero. For both the exhaust gas and the cooling fluid the temperature drops are visible for every ring iteration, after the values settle.

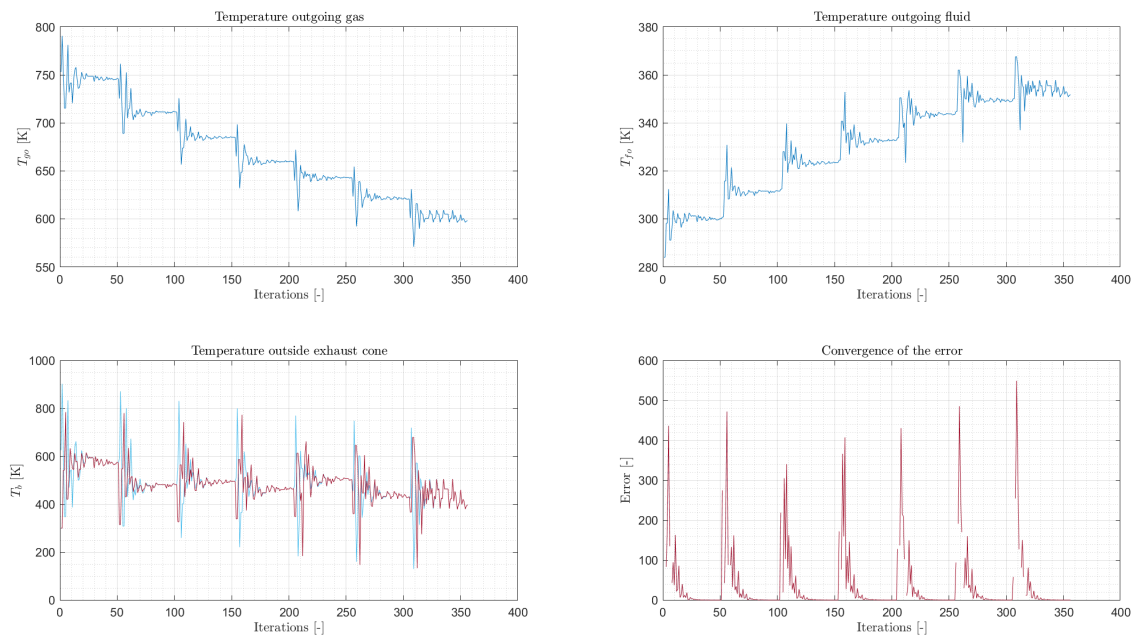


**Figure 4.9:** Results of a specific case using Matlab code

The final exhaust gas temperature leaving the exhaust is 598 K, which means that it is cooled less than expected. This can have a negative impact on some of the mechanical components because some only work in a certain temperature range (i.e., bearings and seals). However, the temperature at the wall of the exhaust is considerably lower at 397 K, which means the goal of implementing a focus point for carbon black condensation can still be accomplished. By keeping the exhaust gas temperature high and the exhaust wall temperature low, the high gradient will strongly increase the thermophoretic phenomena and thus carbon black deposition. Nevertheless, if stronger cooling is necessary to protect the fragile components, various changes can be made to optimize the system. Probably the most effective one would be to use a better cooling fluid than water. The water temperature heats up to 352 K and is thus usable in energy recuperation systems. If the water could be converted to steam for example, a steam generator could provide electricity for the electric motor driving the cleaning mechanism.

## Chapter 5

# Manufacturing

Now that the design and optimization of the cleaning mechanism is finished, the actual manufacturing can begin. This chapter will describe how each of these parts are made and how they have to be assembled to form a functioning mechanism. The technical drawings of these parts can be found in Appendix A. Additional pictures of the manufactured parts and the assembly can be found in Appendix E.

### 5.1 Manufacturing of the parts

All the parts made out of 316L Stainless Steel were designed so that they could be manufactured at the workshop present at De Nayer. In this workshop, the following machines will be used to manufacture the design:

- DMU 50: It is a 5-axis CNC milling machine that allows the manufacturing of complex shapes. 5-axis means that in addition to the three orthogonal axes (x,y,z), two additional movements are possible: rotation of the table and rotation of the head, this is represented on Figure 5.1 by C and B respectively.

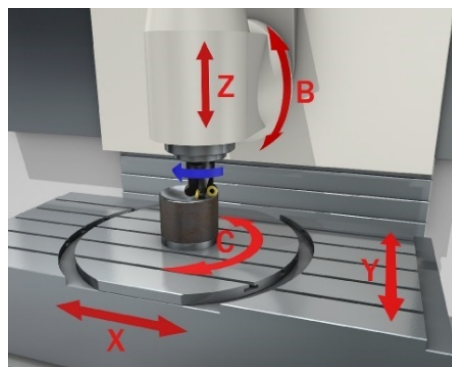


**Figure 5.1:** Coordinate system of a 5-axis CNC milling machine

- Romi C 420: It is a CNC lathe used to manufacture workpieces that have symmetry around their axis. The workpiece is clamped into spindle that makes it rotate. This machine has the ability to drive a cutting tool over two axes: the X-axis and the Z-axis as shown in Figure 5.2.

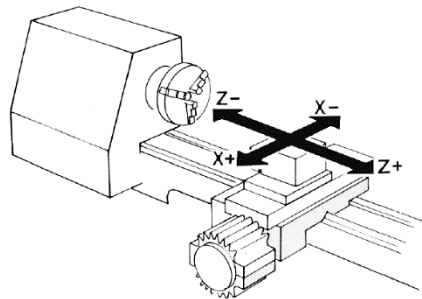


**Figure 5.2:** Coordinate system of a CNC lathe machine

These machines are all CNC driven which means that Computer Aided Manufacturing can be used to program the path that the cutting tool or mill has to follow. A more common name for this language is G-Code.

316L SS was chosen due to its excellent corrosion resistance, good formability, good weldability and toughness due to the austenitic structure of the steel. However, it is considered as a difficult-to-cut material. This is because of a high work hardening tendency, high ductility and low thermal conductivity [45]. This causes high tool wear and made it difficult to determine the right parameters, cutting conditions and toolpaths. The same material should also be used for each part of the assembly because different parts rotate inside each other with only small tolerances. Due to the elevated operating temperatures, the thermal expansion coefficient of all parts should be the same to prevent clamping of these rotating parts.

To manufacture these parts, most of the material has to be purchased. Two round bars of inox 316L with dimensions 90x300 mm and 150x30 mm are ordered from the company Testas NV. There were also some left-over bars and plates of 316L at the machine shop. The machines mentioned above will remove excessive material so that the desired dimensions of the parts can be accomplished.

### **Backplate**

The backplate is manufactured using the DMU 50 milling machine. It is made out of the 150x30 mm inox 316L bar. This 5-axis milling machine is necessary due to the complex shape of the conical hole shown in Figure 5.3. This conical hole is an extension of the conical duct and was implemented in the design so that the scraper could have a larger reach. The outer wall is also elongated to make sure that scraper only rotates inside the parts that were manufactured for this design. This would prevent obstruction of the rotation of the scraper due to possible misalignment with the existing reactor. Eight holes are added to connect the backplate to the reactor with M6 bolts. These holes have a diameter of 7 mm and a spacing of 45° in between. No thread is used in the holes of the backplate because thread is already present in the holes of the reactor. This will

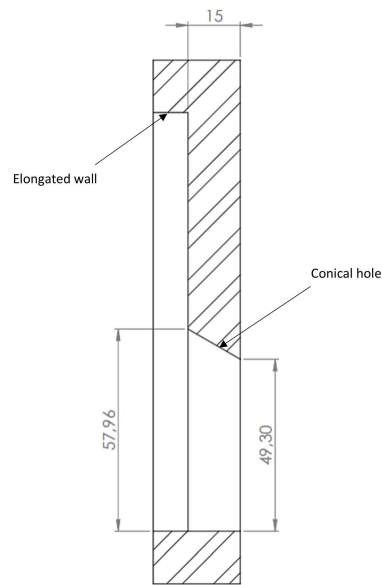


**Figure 5.3:** Section view of backplate of the reactor

provide a better sealing between the two.

The manufacturing process is shown in figure 5.4. It starts with the leveling of one of the sides to remove unevenness. The inside is then pocket milled for a depth of 10 mm. This is followed by milling the  $15^\circ$  hole in steps of one 1 mm. These steps of 1 mm are afterwards leveled using helical movements. After this, a center drill is used to drill small holes positioned at the center of where each connection hole has to be placed to assure the accuracy of these holes. This is followed by the actual drilling of the connection holes. The final manufacturing step is to turn over the back-plate and clamp it again to level the other side of the back-plate.

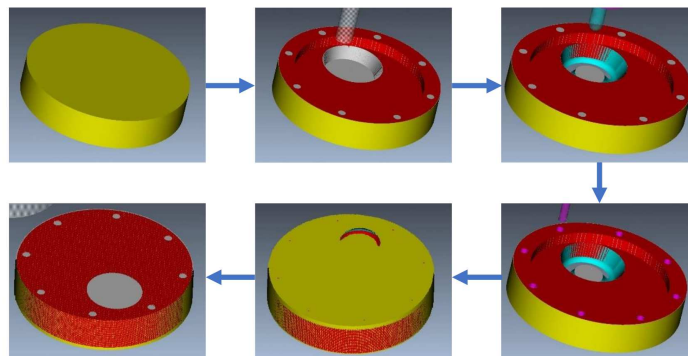


**Figure 5.4:** Manufacturing process of the backplate

### Conical duct

The conical duct is also manufactured with the DMU 50 and also requires the ROMI C 420. It has a

complex shape that would not be possible to manufacture with a 3-axis milling machine. It is made out of the 90x300 mm inox 316L bar. As you can see on Figure 5.5, the conical duct ends with a cylindrical part. This is provided to ease the assembly of the subsequent parts. The inner diameter of this cylindrical part is manufactured with a tolerance H8 according to the ISO-norm ISO 286. This is important because the driven pipe rotates inside so friction is unwanted. Together with the tolerance on the outer diameter of the driven pipe these tolerances result in a loose fit.

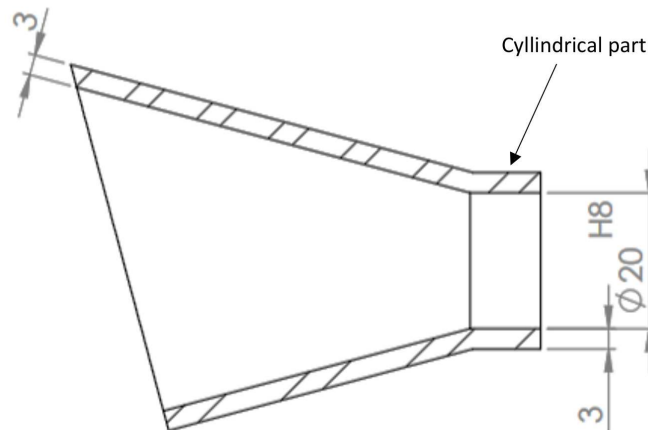


**Figure 5.5:** Section view of the conical duct

The milling process on the DMU 50 is shown in Figure 5.6. It starts with milling of the cylindrical block to just under the chamfered part of the cone. This chamfered part is then leveled using a milling tool. A center hole is drilled so that it can be clamped on the lathe.

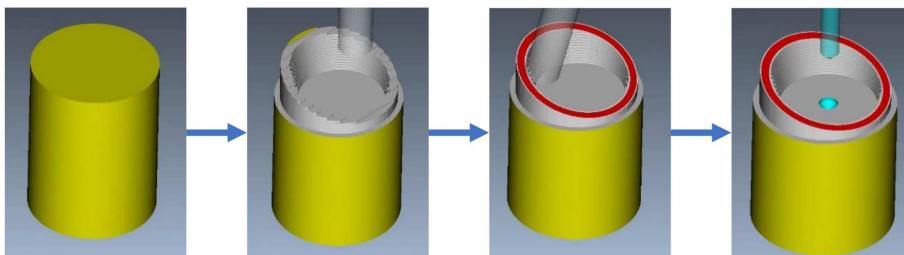


**Figure 5.6:** Milling process of the conical duct

On the lathe, a boring tool is used to remove material on the inside in steps of 1 mm. These steps are then leveled using a parting tool. A turning tool is used to remove the material on the outside in steps of 1 mm and is also leveled using a parting tool. Figure 5.7 shows the production process on the lathe.

### Cylindrical hub

The two parts of the cylindrical hub are manufactured with the DMU 50 and the Romi C 420. It is made out of the purchased 90x300 mm inox 316L bar. Most of these parts can be manufactured



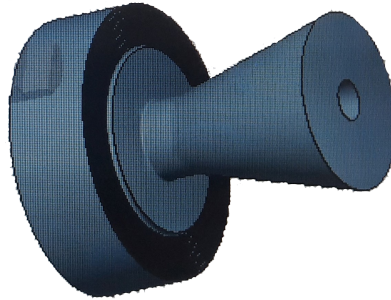


**Figure 5.7:** Turning process of the conical duct

using the lathe machine due to the symmetry around their axis. However, in one of these parts an opening of  $180^\circ$  has to be made to allow for the belt to go outside the housing so that it can be connected to the external pulley. An opening of  $180^\circ$  is chosen so that there is some flexibility in the placement of the external stepper motor. The two parts, shown in Figure 5.8, are connected to form the cylindrical hub using a M6 bolt and nut. For this reason, four connection holes of diameter 6.5 mm are added with a  $90^\circ$  spacing in between. This makes the entire design easy to assemble and disassemble when maintenance is necessary. Both the bearings and the seals have to fit in these parts. These components require a different tolerance fit: a tolerance of H8 on the inside diameter of both parts is necessary for the seals and a tolerance of K7 on the inside diameter of the part connected to the conical duct. It is possible to apply thread to the right hub. This thread can be used to attach the subsequent system to the cleaning mechanism.

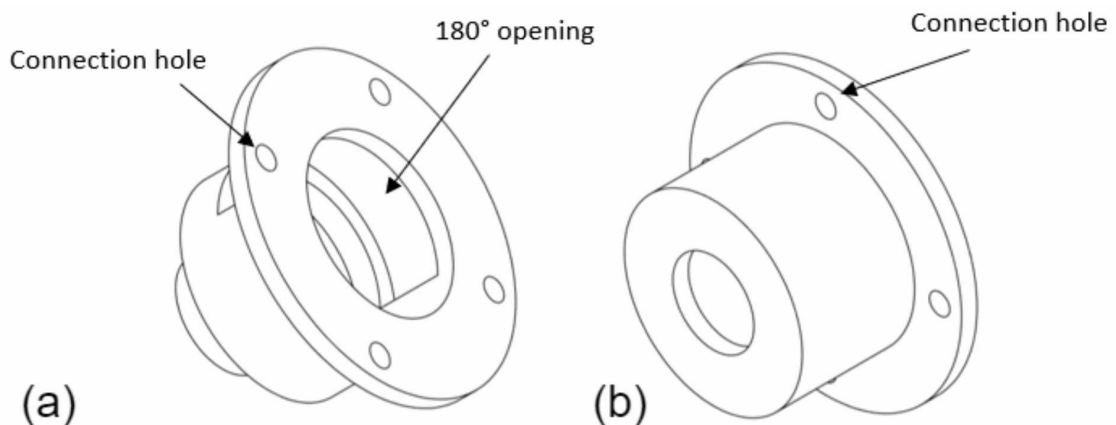


**Figure 5.8:** (a) Right hub: part of the cylindrical hub that has the opening for the belt, (b) left hub: part of the cylindrical hub that is connected to the conical duct

The manufacturing process is shown in Figure 5.9. It starts with the removal of the material on the outside to the correct diameter using a turning tool. The cylindrical bar is then sawed in two pieces to make the individual parts. Figure 5.8 (b) is made by first removing the material on the inside with

the correct tolerances for the seals and the bearing. It is then unclamped so that it can be put in the DMU 50 milling machine. The mill drills the four connection holes. Figure 5.8 (a) undergoes the same steps, with an additional step on the 5-axis milling machine to create the slot.

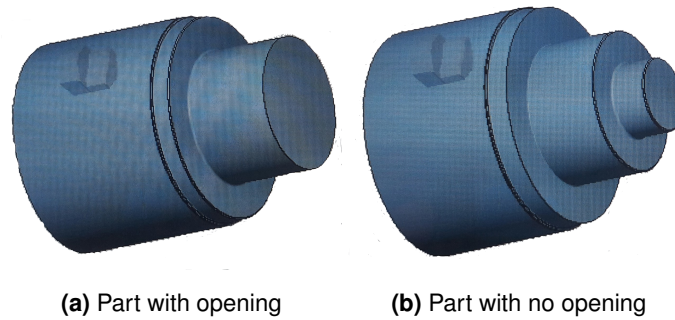


**Figure 5.9:** Manufacturing process on the lathe of the housing

### Driven pipe

This is the rotating part of the assembly and therefore has to be accurately manufactured. Any manufacturing flaws might impede the rotational motion. The part can be manufactured using the Romi C 420 lathe due to its symmetry around the axis. Figure 5.10 shows the section view of this part. There are a lot of parts and components connected to this pipe so different tolerances are required. The tolerance f8 is chosen so that together with the tolerance on the inner diameter of the cylindrical part of the conical duct and the inner diameter of the cylindrical hub (both H8) a loose fit is possible. Tolerance h11 and j6 are the required shaft tolerances for respectively the seals and the bearings. As you can see on Figure 5.10, a hole with thread for an M3 bolt is added. This is used to connect the pulley from the driving mechanism to this pipe.

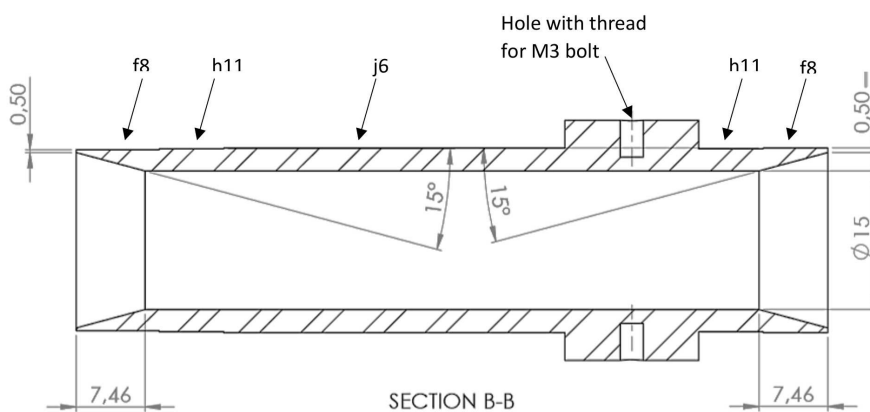


**Figure 5.10:** Section view of the driven pipe

Due to the length of the workpiece, it has to be clamped twice as shown on Figure 5.11. This means that the first part of the outside can be removed with a turning tool and part of the inside can

be removed using a boring tool. The workpiece is then turned around and these steps are repeated on the other side. The last step is to drill the M3 holes using a pillar drill.

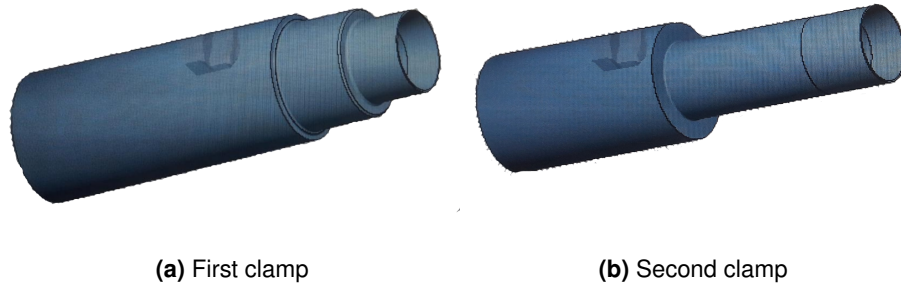


**Figure 5.11:** Manufacturing process on the lathe of the driven pipe

### Scraper

The scraper is manufactured out of a left-over flat plate of 316L and is made using the DMU 50 and a Electron Discharge Machine (EDM). The basic shape with the triangular shaving on top is cut out using the milling machine without cutting through the entire flat plate, this is shown in Figure 5.12. Due to the scrapers long and thin shape, it is not possible to further cut away the material with the milling machine because this might damage the component. Therefore, the EDM is used to cut out the rectangular circumference of the scraper and remove the material on the back to get the correct thickness.

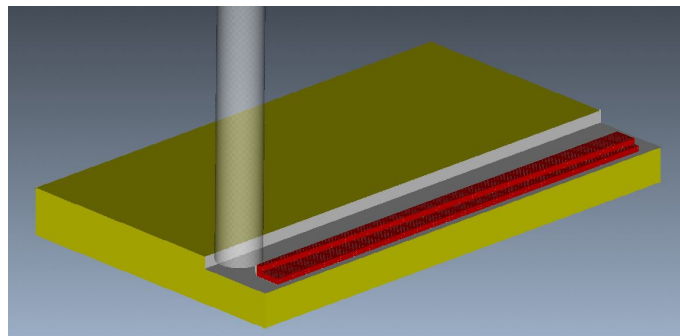


**Figure 5.12:** Milling proces of the scraper

## 5.2 Assembly of the mechanism

The back-plate of the reactor is used as the base component to further attach the other components to. The conical duct is connect to this part using a Tungsten Inert Gas (TIG) weld around the entire conical hole. This conical hole of both parts has to be perfectly aligned to make sure that the rotating scraper will not come into contact with the back-plate. The next step is to attach the left hub to the conical duct. This is also done with a TIG weld around the entire, now cylindrical, hole. Both of these welds are visible in Figure 5.13.



**Figure 5.13:** Connection welds between back-plate, conical duct and left hub

Welding the conical duct to the left hub caused the diameter of the cylindrical part (shown in Figure 5.5) to shrink, which means that the tolerance fit for the driven pipe was not correct anymore and there was too much friction to smoothly rotate the driven pipe. This was fixed by using a hand drill with Tungsten Carbide burrs to slightly increase the diameter. This has no effect on the alignment of the pipe because the bearings are responsible for this.

To attach the scraper to the driven pipe, some sort of holder has to be foreseen. This holder, shown in Figure 5.14, can be made using the Electron Discharge Machine (EDM) available at the campus. It is then welded using spot-welding on the inside of the conical part of the driven pipe. It was however not possible to manufacture this part within the given time-frame.

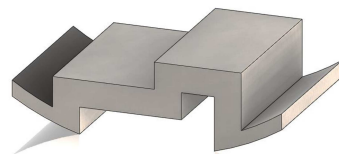


**Figure 5.14:** Holder used to fixate the scraper to the driven pipe

Now that the left hub is assembled, the different components that have to be put inside the hub can be added. It starts with adding the seal inside the hub. Next, the two bearings are pressed on the

driven pipe and the large pulley is connected to it using M3 bolts. The bearings with the driven pipe are then pressed in the left hub.

Finally, the right hub with the seal can be connected to the left hub using the M6 bolts and nuts to complete the housing and the belt is added to connect the large pulley to the stepper motor. The manufactured assembly of the mechanism is shown in Figure 5.15

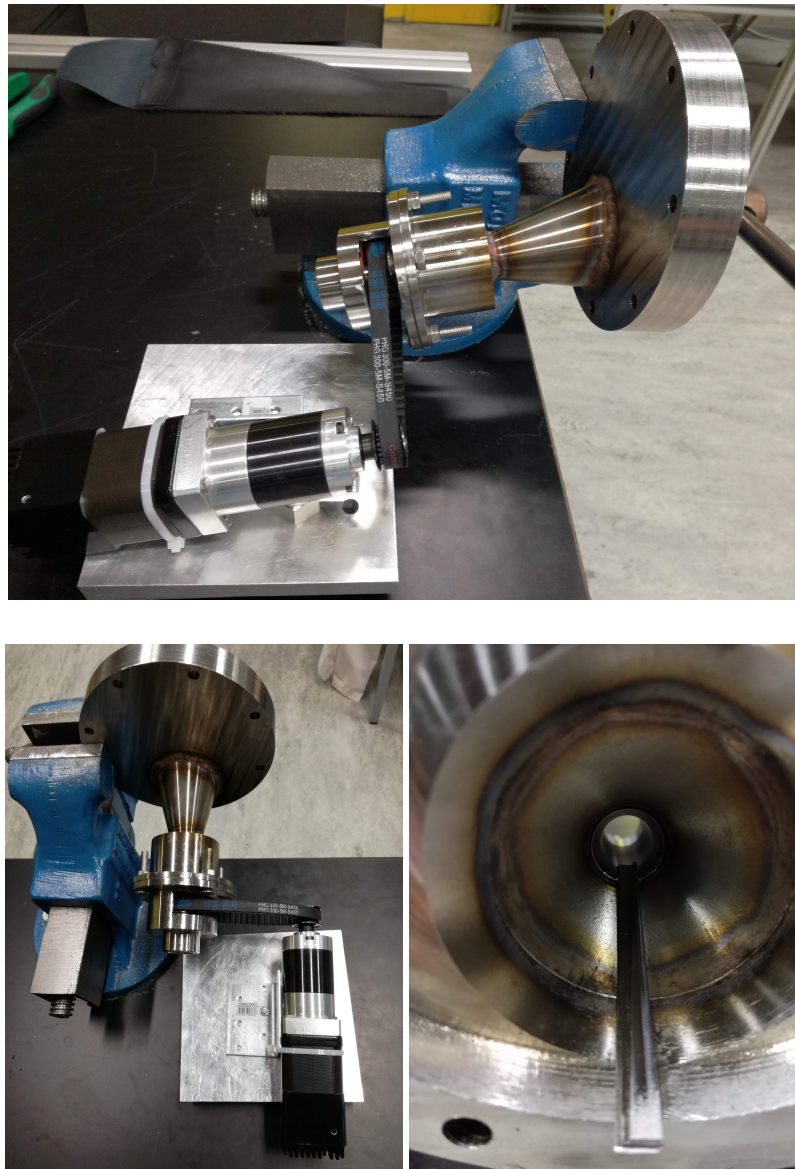


**Figure 5.15:** Different views of the manufactured assembly



## Chapter 6

# Experimental testing and results

The reactor that is available at the STTL is unable to crack methane and therefore can not produce carbon black. In order to validate the design, the deposition process on the exit port walls has to be simulated separately from the reactor. This means that there is no large temperature gradient or gas flow. A well thought-out test set-up has to be developed to take this into account. Nanoscale carbon black also comes with various health hazards due to it being easily dispersible. This is in particular a problem because without attaching the back-plate to the reactor, there is no closed of reactor cavity that can contain the carbon particles. For this reason, an alternative powder to carbon black has to be found that is representative to how carbon black would behave inside the reactor.












### 6.1 Powder selection

Since it is not possible to use nanoscale carbon black to perform tests with, an alternative has to be found to determine whether the mechanism works or not. To do so, various powder production companies and Professors with more knowledge and experience in this field of expertise were contacted. Professor Dewil and Professor Baeyens from the Department of Chemical Engineering, Professor Vleugels from the Department of Material Science and Professor Moens from the department of Mechanical Engineering all suggested different powders and substance that might work.

These powders are tested with a basic test set-up that included a flat surface of 316L stainless steel that was placed at a  $15^\circ$  angle. The powder is then pressed and flattened against the surface, to determine how much of the powder remains on the surface and how thick this layer could be. Afterwards some powder was sprinkled on the surface to see if it sticks or just falls down. This is necessary because sprinkling additional powder on the surface is required to test if continuous cleaning by the mechanism is possible. The final step was to slightly touch the powder to simulate the movement of the scraper. The tests were performed under two conditions: (a) with a dry surface, and (b) with a slightly wetted surface. The observations of these test with some of the powders is summarized in Table 6.1.



**Table 6.1** Summary of the observations from the initial test

Powder	(a) Observations (dry surface)	(b) Observations (wetted surface)
Cement (Prof. Dewil)	<ul style="list-style-type: none"> <li>• Thickness: <math>\approx 1</math> mm</li> <li>• Layer holds against gravity and soft blowing</li> <li>• Peels completely off with slight touch</li> </ul> 	<ul style="list-style-type: none"> <li>• Thickness: <math>&gt;2</math>mm</li> <li>• Sprinkled powder sticks</li> <li>• Peels completely off with slight touch</li> </ul> 
Calcium Carbonate (Prof. Dewil)	<ul style="list-style-type: none"> <li>• Thickness: <math>&gt;1</math>mm</li> <li>• Sprinkled powder does not stick</li> <li>• Peels completely off with slight touch</li> </ul> 	<ul style="list-style-type: none"> <li>• Thickness: <math>\approx 2</math>mm</li> <li>• Sprinkled powder sticks</li> <li>• Peels completely off with slight touch</li> </ul> 
Corn-starch (Prof. Dewil)	<ul style="list-style-type: none"> <li>• Thickness: /</li> <li>• Powder falls straight down</li> </ul> 	<ul style="list-style-type: none"> <li>• Thickness: 2-3mm</li> <li>• Sprinkled powder sticks</li> <li>• Peels completely off with slight touch</li> </ul> 
Nutrilon (Prof. Dewil)	<ul style="list-style-type: none"> <li>• Thickness: /</li> <li>• None of the powder sticks when pressed or sprinkled</li> </ul> 	<ul style="list-style-type: none"> <li>• Thickness: /</li> <li>• Almost none of the powder sticks when pressed or sprinkled</li> </ul> 
Talc powder (Prof. Dewil)	<ul style="list-style-type: none"> <li>• Thickness: 3mm</li> <li>• Some sprinkled powder sticks</li> <li>• Peels completely off with slight touch</li> </ul> 	<ul style="list-style-type: none"> <li>• Thickness: 3mm</li> <li>• Some sprinkled powder sticks</li> <li>• Peels completely off with slight touch</li> </ul> 
Graphite (Prof. Vleugels)	<ul style="list-style-type: none"> <li>• Thickness: <math>&lt;1</math>mm</li> <li>• Slightly blowing reduces the thickness to a very thin layer</li> </ul> 	/



From these observations, it is clear that none of these powders are suited. For most, the layer thickness was sufficient ( $> 0.5$  mm) but they completely peeled off with the slightest touch. This should not happen because it does not represent how the carbon black inside the reactor behaves and thus gives no representative results.

This basic test also showed that graphite was not a suitable replacement because it only formed a thin layer. This was unexpected due to the similarities it has with carbon black in terms of chemical composition and, to a more limited extent, in molecular structure as discussed in the literature survey. To find out the reason for this, electron microscope images of the graphite powder were taken. These are shown in Figure 6.1

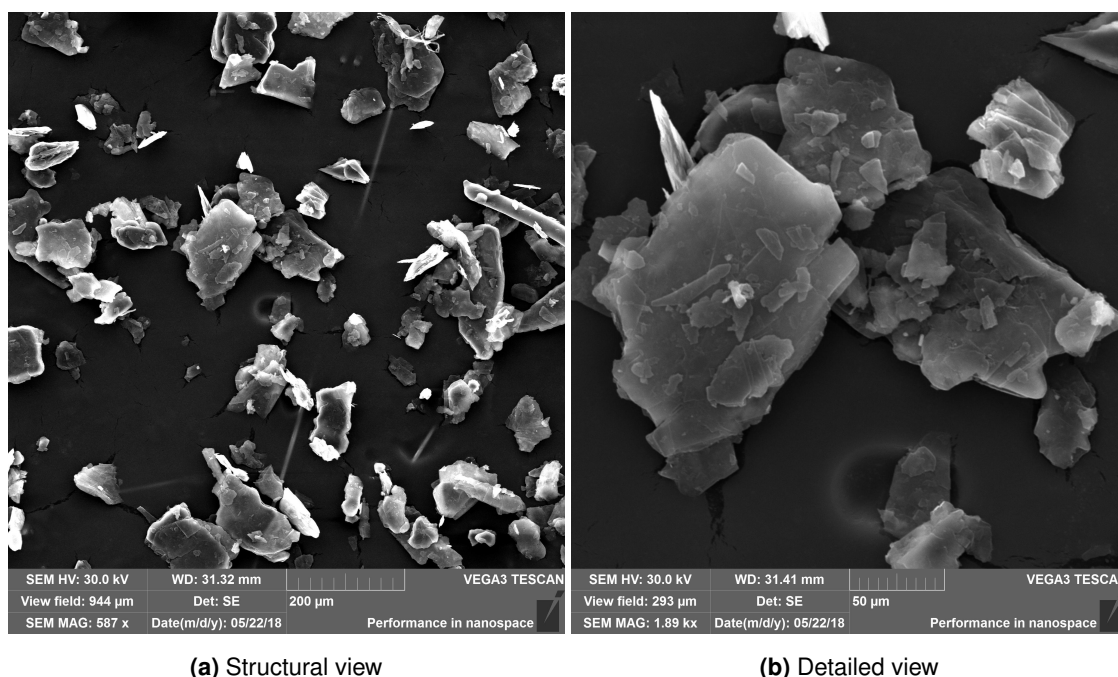


**Figure 6.1:** Electron microscope images of graphite

Based on the literature survey it can be concluded that adhesion between both particle-surface and particle-particle is caused by the Van der Waals force. This interaction force is mainly influenced by the surface-to-volume ratio. The strength of powders is additionally influenced by particle diameter, shape and packing density according to Eq. 2.3. The microscopic images can be used to give an idea of some of these characteristics. Figure 6.1 shows that the graphite particles are non-spherical and quite flat. They have a non-uniform size where most of the particles are larger than  $100 \mu\text{m}$ . When compared to TEM-images of carbon black (Figure 2.3b) the powder does not have similar powder structure or particle shape. This explains why graphite does not act in the same way as carbon black in terms of cohesiveness of the powder despite the similarities in chemical composition and molecular structure

There were however, two other powders suggested. These powders are: Lactose powder sieved to a particle diameter of  $63 \mu\text{m}$  suggested by Professor Baeyens, and Vanilla powder suggested by Professor Moens. They behave much more like how the carbon black is expected to behave when

tested with the previous tests. For this reason, more in-depth tests will be performed to determine which one of these two powders is the most suitable.

Figure 6.2 shows electron microscope images of vanilla powder. Based on these images, the particle diameter can be estimated to be around  $15\ \mu\text{m}$ . It is also clear that the powder consists out of uniform sized, spherical primary particles that form small aggregates. When compared to carbon black produced by a solar reactor (Figure 2.3b), the vanilla powder has a similar shape and structure. However, the particle diameter is still three orders of magnitude larger.

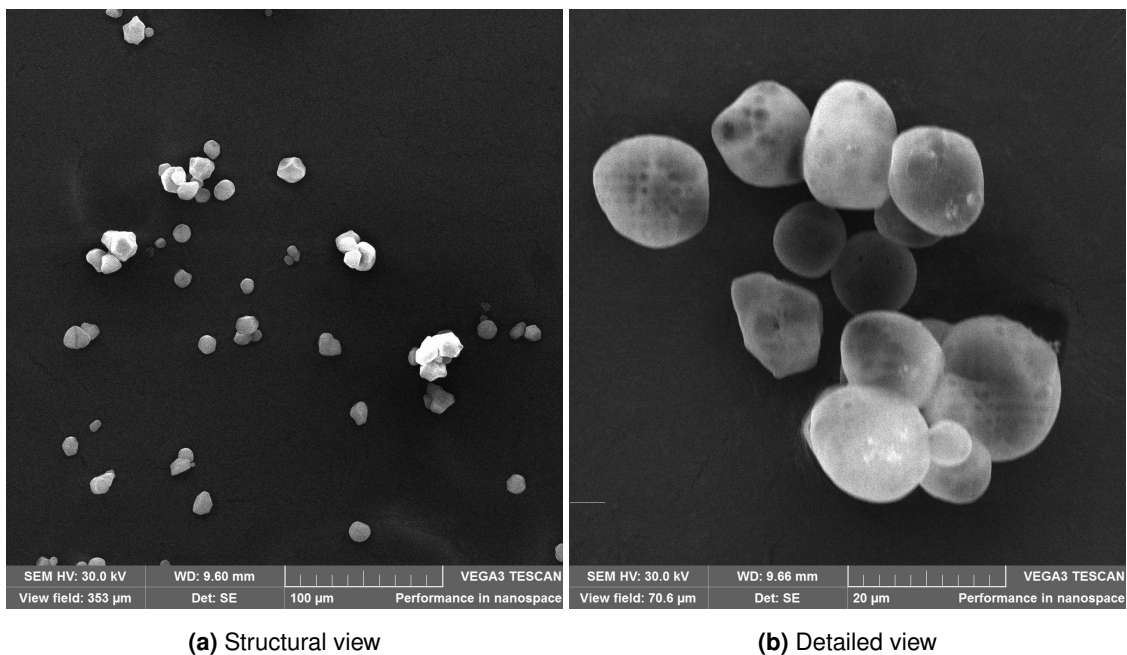
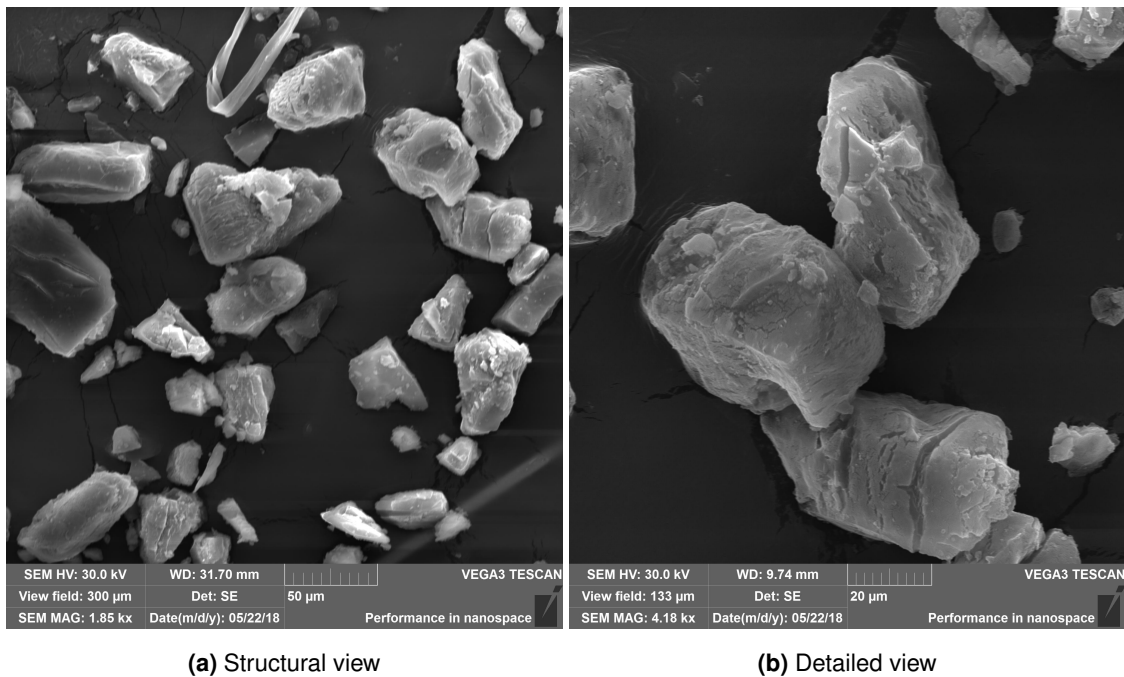


**Figure 6.2:** Electron microscope images of vanilla powder

Figure 6.3 shows electron microscope images of sifted lactose powder. These images show that the particles are non-spherical, making it harder to determine an estimated particle diameter. It is clear however that these particles have non-uniform size and are larger than the particles of vanilla powder ( $20\text{-}70\ \mu\text{m}$ ). When compared to carbon black produced by a solar reactor (Figure 2.3b), the sifted lactose does not have a similar structure nor similar shape and the particles are also three orders of magnitude larger.

Based on these images and what is known from the literature survey (in particular Eq. 2.3), it can be concluded that vanilla powder is the most suitable option to replace carbon black during the experimental phase of this thesis. This result is also in line with the basic test that is mentioned above: the vanilla powder stucked better to the wall and the particles than the sifted lactose. It is important to mention that although this powder has similar shape, structure and the smallest diameter of the tested powders, this diameter is still three orders of magnitude larger than carbon black. It is expected that the adhesion of carbon black particles will be greater than vanilla powder and therefore will be harder to remove.



(a) Structural view

(b) Detailed view

**Figure 6.3:** Electron microscope images of sifted lactose

## 6.2 Test set-up

As previously discussed, there is no actual reactor available to attach the cleaning mechanism onto. An alternative set-up will be described here so that certain experiments can be done, testing the efficiency of this solution. This set-up will contain the cleaning mechanism itself in combination with a simple construction to support it. Other elements include an extension to the exhaust, a container to collect the powder and some covers to keep the experiments in a relatively closed surrounding. The first problem that needs fixing is the lack of an actual gas flow. The hydrogen flow in an actual reactor carries the carbon black particles into the conical exhaust where these particles will deposit rapidly due to the cooling. When this gas flow is not present, the powder cannot get to the cone to deposit, and the scraped powder cannot be removed from it. A simple and easy solution was found by rotating the entire mechanism, from back-plate to motor, for 90 degrees. This means the backplate will be placed horizontally instead of vertically, and the exhaust will be hanging under an angle of 15 degrees from the vertical axis instead of the horizontal axis. This can be seen on Figure 6.4.

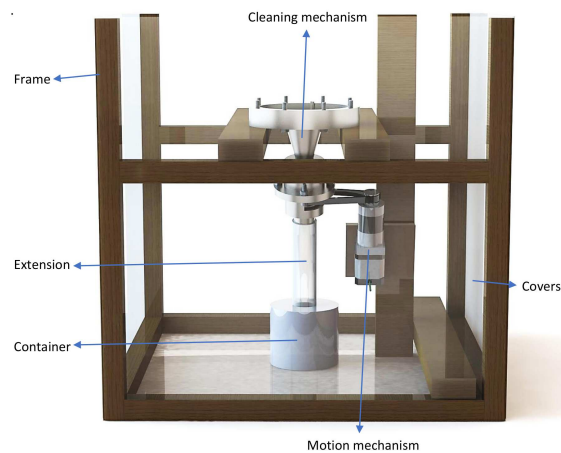
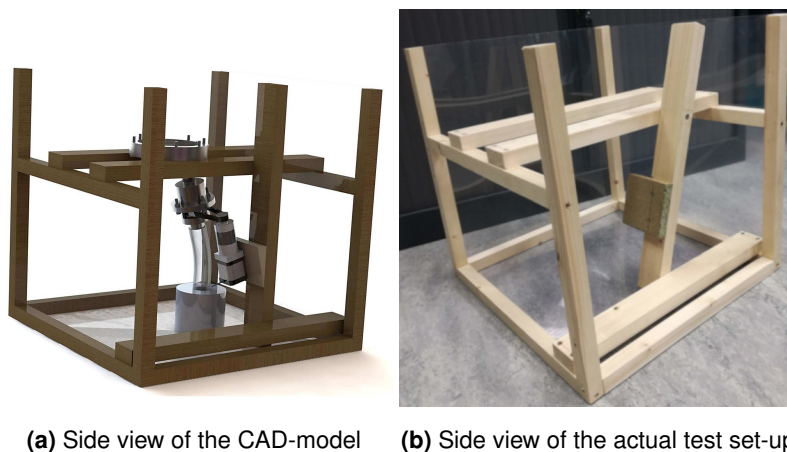


**Figure 6.4:** Frontal view of the test set-up

Previously in section 6.1, a powder was chosen to replace the deposited carbon black. Because of the characteristics of this powder, there is no need for high temperatures to get it sticking to the surface, like carbon black does. This means the materials that are being used do not need a temperature resistance threshold. For the frame simple wooden boards are used, and the covers consist of see-through PVC plates. These plates are first fixed to the frame with screws for positioning. Then they are accurately glued and sealed with silicones, so that there is no powder leakage out of the test set-up. For the exhaust extension and collecting container simple and cheap materials can be chosen as well



(a) Side view of the CAD-model      (b) Side view of the actual test set-up

**Figure 6.5:** Test set-up

As shown on Figure 6.5, this set-up also includes a wooden ramp with a 15 degree angle. Placing this ramp vertically on the framework ensures a good support for the motor. This is important because both pulleys of the mechanism need to be in the same plane, and the motor should then be placed perpendicular to the driving pulley. Otherwise, the belt can encounter forces outside its working plane which it is not designed for.

## Chapter 7

# Conclusion and future work

To tackle the negative effect of carbon deposition at the exit port of a solar reactor, a novel mechanical cleaning mechanism is proposed. The design features the rotational motion of a scraper to provide the shear force required to remove the agglomerated carbon particles deposited at the exit port. This allows a continuous operation of the solar reactor.

Chapter 1 gives a brief explanation of the general working principle that is used to crack methane. It is clear that solar thermo-chemical cracking of methane using concentrated solar energy and a solar reactor provides an environmentally-friendly alternative to the processes that are currently used to produce both Hydrogen and carbon black. This is mainly due to the absence of carbo-oxygen and nitro-oxygen emissions during production. However, the clogging of the exhaust port remains one of the major problems that has to be solved to allow for this novel process to be used in practice.

In Chapter 2, an in-depth literature survey is performed to get a thorough understanding of the physical properties that determine the characteristics of carbon black in general: chemical composition, molecular structure, morphology and surface area are used to characterize the different grades of carbon black. Research done by Rodat et al. [5] concluded that the properties of carbon black produced by a solar reactor could be comparable to the properties of commercial grade carbon black under the right circumstances. The physical mechanisms that cause the deposition were also researched. There are two key steps in the deposition process that eventually leads to clogging: (a) the transportation step that bring the particles in the vicinity of the wall, mainly due to the thermophoretic force caused by a temperature gradient, and (b) the interaction between particle-wall and particle-particle that causes adhesion, mainly due to the attractive Van der Waals forces, particle diameter and shape. It is clear that the Van der Waals force has to be overcome by an externally applied force in order to remove particles. It is important to note that this interaction force is physical, which means that the force that is required to remove particles will not be high in comparison with for example chemically bound structures.

Chapter 3 describes the development process of the novel cleaning mechanism to prevent the

clogging of the reactor. A half-section view of the final design is shown in Figure 7.1 with a design constraints checklist on the right.

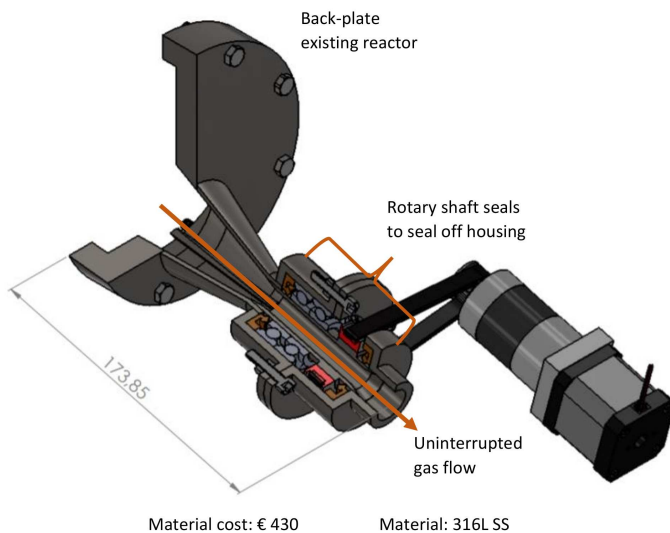


**Figure 7.1:** Half-section view of the cleaning mechanism

- ✓ The mechanism must not interrupt the gas flow
- ✓ Material of the mechanism should withstand high temperatures
- ✓ Hydrogen leakage should be minimal and monitored by sensors
- ✓ The mechanism must be compatible with the back-plate of the existing reactor
- ✓ Compact
- ✓ Possibility to be coupled with carbon black collection
- ✓ Cost effective
- ✓ Manufacturable design

An important remark was that in some cases design geometry did not yield with what had to be accomplished. Therefore, flow dynamics on ideal gas behavior was used to accomplish the objectives without making any changes on the CAD-drawing. This is clearly seen from the fundamental understanding of the condensation process of carbon black. Cooling of the design takes advantage of the condensation process by implementing a focus point for forced deposition. This will prevent deposition further downstream were no cleaning device is available.

Numerical analyses were performed in Chapter 4 to dimension and further optimize the design. Calculation of the load torque showed that with the dimensions of the scraper, a torque of 0.017 Nm is required to remove a layer of carbon black. Static and dynamic analysis using FEA on the scraper concluded that, with a maximal stress of 11.8 MPa at the base of the scraper and the first modal frequency being at 192.62 Hz, both the mechanical properties and dynamic behavior of the structure will not fail for this application. Heat transfer analysis of the cooling using MATLAB<sup>®</sup> determined that the outgoing temperature of the gas was 598 K. The large temperature gradient between the cooled exhaust walls and the slightly cooled exhaust gas will enlarge the forced condensation phenomena. On the other hand, because the exhaust gasses are not cooled sufficiently, there will also be a temperature gradient further downstream after the cleaning mechanism which could cause deposition there and lead eventually to clogging. The exhaust gasses might also be too hot for some of the mechanical components. Therefore, the cooling system needs to be further optimized to lower temperatures in the exhaust after the cleaning mechanism.

Chapter 5 gives an overview of how the parts are manufactured and how the design is assembled.

The high work hardening tendency, low thermal conductivity and high ductility of Stainless steel caused high tool wear making it very hard to determine the right parameters, cutting conditions and toolpaths. For this reason, the manufacturing of the parts suffered an unforeseen delay which caused a chain reaction where the small problems that usually occur in the assembly phase of novel designs had to be fixed in a too short time-frame. This finally led to the retardation of the experimental phase, which could not get carried out to the fullest.

In Chapter 6, experimental research for an alternative powder to carbon black was conducted due to a closed of reactor cavity not being available at the STTL. Based on observations from a basic test and more in-depth research using an electron microscope, vanilla powder was found to be the most suitable out of the tested powders due to its small particle diameter (15  $\mu\text{m}$ ) and its similar shape and powder structure to carbon black. A test set-up was also developed that can be used to simulate the deposition process outside of the reactor. Gravitational settling is used to solve the lack of a gas flow and dispersion of the powder is reduced due to the partially closed-of testing environment. Both the powder and the test set-up were going to be used to experimentally test whether the developed cleaning mechanism was able to keep the exit port from clogging. However, due to the delay during the manufacturing phase it was not possible to do these experiments within the given time frame.

It is clear that research does not end here, but needs to continue to improve this novel design. This includes upscaling the model for larger reactors and higher temperatures, optimizing the cooling system to get maximal efficiency and protect mechanical components, and testing of the mechanism with various experiments to ensure its working and viability.





# Bibliography

- [1] N. Ozalp, M. Epstein, and A. Kogan, "Cleaner pathways of hydrogen, carbon nano-materials and metals production via solar thermal processing," *Journal of Cleaner Production*, vol. 18, no. 9, pp. 900–907, 2010. [Online]. Available: <http://dx.doi.org/10.1016/j.jclepro.2010.01.020>
- [2] D. Hirsch and A. Steinfeld, "Radiative transfer in a solar chemical reactor for the co-production of hydrogen and carbon by thermal decomposition of methane," *Chemical Engineering Science*, vol. 59, no. 24, pp. 5771–5778, 2004.
- [3] M.-J. Wang, C. Gray, S. Reznick, K. Mahmud, and Y. Kutsovsky, "Carbon black," in *Kirk-Othmer Encyclopedia of Chemical Technology*, Kirk-Othmer, Ed. Wiley, 2011, vol. 4, pp. 761–803. [Online]. Available: <http://www.springerreference.com/index/doi/10.1007/SpringerReference{-}208034>
- [4] International Carbon Black Association, "Carbon Black User ' s Guide," p. 36, 2016. [Online]. Available: <http://www.carbon-black.org/images/docs/2016-ICBA-Carbon-Black-User-Guide.pdf>
- [5] S. Rodat, S. Abanades, E. Grivei, G. Patrianakos, A. Zygianni, A. G. Konstandopoulos, and G. Flamant, "Characterisation of carbon blacks produced by solar thermal dissociation of methane," *Carbon*, vol. 49, no. 9, pp. 3084–3091, 2011.
- [6] D. Jaya Krishna and N. Ozalp, "Numerical investigation of particle deposition inside aero-shielded solar cyclone reactor: A promising solution for reactor clogging," *International Journal of Heat and Fluid Flow*, vol. 40, pp. 198–209, 2013. [Online]. Available: <http://dx.doi.org/10.1016/j.ijheatfluidflow.2012.12.004>
- [7] M. Kogan and A. Kogan, "Production of hydrogen and carbon by solar thermal methane splitting. i. the unseeded reactor," *International Journal of Hydrogen Energy*, vol. 28, no. 11, pp. 1187–1198, 2003.
- [8] A. Kogan, M. Kogan, and S. Barak, "Production of hydrogen and carbon by solar thermal methane splitting. ii. room temperature simulation tests of seeded solar reactor," *International Journal of Hydrogen Energy*, vol. 29, no. 12, pp. 1227–1236, 2004.

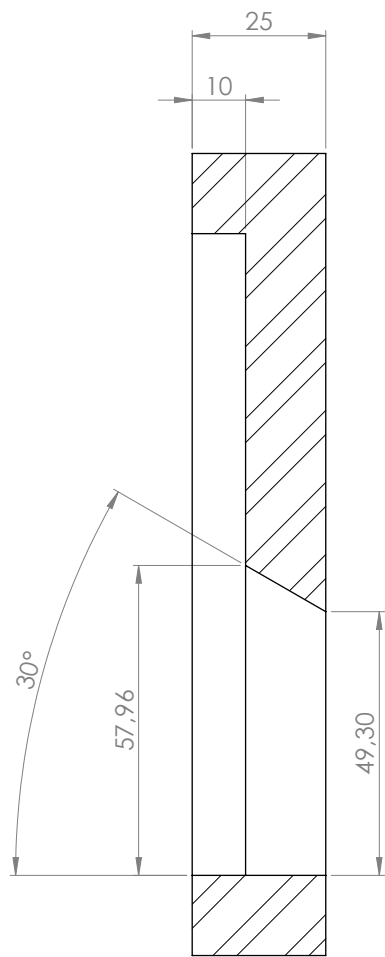
- [9] J.-P. Minier, "A general introduction to particle deposition," in *Particles in Wall-Bounded Turbulent Flows : Deposition , Re-Suspension and Agglomeration*, J.-P. Minier and J. Pozorski, Eds. Springer, 2016, ch. 1, pp. 1–36.
- [10] K. Kendall and C. Stainton, "Adhesion and aggregation of fine particles," *Powder Technology*, vol. 121, no. 2-3, pp. 223–229, 2001.
- [11] A. R. Razmavar and M. R. Malayeri, "A simplified model for deposition and removal of soot particles in an exhaust gas recirculation cooler," *Journal of Engineering for Gas Turbines and Power*, vol. 138, no. 1, p. 11505, 2016.
- [12] M. Abarham, T. Chafekar, J. W. Hoard, A. Salvi, D. J. Styles, C. Scott Sluder, and D. Assanis, "In-situ visualization of exhaust soot particle deposition and removal in channel flows," *Chemical Engineering Science*, vol. 87, pp. 359–370, 2013.
- [13] D. C. Hanselman, *Brushless permanent magnet motor design*, 2nd ed. Magna Physics Publishing, 2006.
- [14] T. Arvind and T. Shyam, *Handbook of Solar Energy*, H. R. Muhammad, Ed. Springer, 2016.
- [15] P. Hartley, G. Parfitt, and L. Pollack, "The role of the van der waals force in the agglomeration of powders containing submicron particles," *Powder technology*, vol. 42, no. 1, pp. 35–46, 1985.
- [16] N. Ozalp, "Hydrogen production with zero emissions footprint: Challenges and solutions towards commercialization," in *Black Sea Energy Resource Development and Hydrogen Energy Problems*, A. Veziroglu and M. Tsitskishvili, Eds. Springer, 2013, ch. 3, pp. 19–35.
- [17] N. Ozalp and V. Shilapuram, "Step-by-step methodology of developing a solar reactor for emission-free generation of hydrogen," *International Journal of Hydrogen Energy*, vol. 35, no. 10, pp. 4484–4495, 2010. [Online]. Available: <http://dx.doi.org/10.1016/j.ijhydene.2010.02.032>
- [18] J. B. Donnet, *Carbon Black: Science and Technology, Second Edition*. Taylor & Francis, 1993. [Online]. Available: <https://books.google.be/books?id=SPpx6MkRYwMC>
- [19] M. Abarham and J. Hoard, "Review of soot deposition and removal mechanisms in egr coolers," *SAE International Journal of Fuels and Lubricants*, vol. 3, no. 1, pp. 690–704, 2010. [Online]. Available: <http://saefuel.saejournals.org/content/3/1/690.short>
- [20] H. F. Lutro, "The effect of thermophoresis on the particle deposition on a cylinder," Master's thesis, Institutt for fysikk, 2012.
- [21] C. Henry, "Surface forces and their application to particle deposition and resuspension," in *Particles in WallBounded Turbulent Flows: Deposition, Re-Suspension and Agglomeration*, J.-P. Minier and J. Pozorski, Eds. Springer, 2016, ch. 5, pp. 209–261.
- [22] J.-P. Schermann, "Modelling," in *Spectroscopy and Modeling of Biomolecular Building Blocks*. Elsevier, 2008, pp. 1–57.

- [23] C. Henry, J. P. Minier, and G. Lefèvre, "Numerical study on the adhesion and reentrainment of nondeformable particles on surfaces: The role of surface roughness and electrostatic forces," *Langmuir*, vol. 28, no. 1, pp. 438–452, 2012.
- [24] J. Katainen, M. Paajanen, E. Ahtola, V. Pore, and J. Lahtinen, "Adhesion as an interplay between particle size and surface roughness," *Journal of Colloid and Interface Science*, vol. 304, no. 2, pp. 524–529, 2006.
- [25] C. Q. LaMarche, S. Leadley, P. Liu, K. M. Kellogg, and C. M. Hrenya, "Method of quantifying surface roughness for accurate adhesive force predictions," *Chemical Engineering Science*, vol. 158, no. August 2016, pp. 140–153, 2017. [Online]. Available: <http://dx.doi.org/10.1016/j.ces.2016.09.024>
- [26] R. Wilson, D. Dini, and B. Van Wachem, "The influence of surface roughness and adhesion on particle rolling," *Powder Technology*, vol. 312, pp. 321–333, 2017. [Online]. Available: <http://dx.doi.org/10.1016/j.powtec.2017.01.080>
- [27] F. W. Delrio, M. L. Dunn, B. L. Boyce, A. D. Corwin, and M. P. De Boer, "The effect of nanoparticles on rough surface adhesion," *Journal of Applied Physics*, vol. 99, no. 10, 2006.
- [28] B. P. Yung, H. Merry, and T. R. Bott, "The role of turbulent bursts in particle re-entrainment in aqueous systems," *Chemical Engineering Science*, vol. 44, no. 4, pp. 873–882, 1989.
- [29] M. Dromgool, "On coating stainless steel," *Journal of Protective Coatings and Linings*, vol. 27, no. 1, pp. 8–11, Jan. 2009.
- [30] J. Bartanen, "MIG," 2017.
- [31] H. Wittel, D. Muhs, D. Jannasch, and J. VoBiek, *Roloff/Matek machineonderdelen (Theorieboek)*, 5th ed., Heymans and Vanhove, Eds. Academic Service, 2013.
- [32] O. de Weck and K. Il Yong, "Finite Element Method," Massachusetts, 2004.
- [33] R. J. Roark, W. C. Young, and R. Plunkett, *Formulas for Stress and Strain*. McGraw-Hill, 1976, vol. 43. [Online]. Available: <http://appliedmechanics.asmedigitalcollection.asme.org/article.aspx?articleid=1403104>
- [34] P. Sas, W. Desmet, W. De Roeck, and D. Moens, "Dynamische Aspecten: Theorie."
- [35] Y. A. Cengel and A. J. Ghajar, *Heat and Mass Transfer: Fundamentals and Applications*, 5th ed. McGraw-Hill Education, 2011.
- [36] Y. Cengel, "Heat Transfer: A Practical Approach," *McGraw - Hill*, p. 932, 2002. [Online]. Available: <http://highered.mcgraw-hill.com/sites/dl/free/0073398128/835451/App1.pdf>
- [37] J. Pátek, J. Hrub, J. Klomfar, M. Součková, and A. H. Harvey, "Reference correlations for thermophysical properties of liquid water at 0.1 MPa," *Journal of Physical and Chemical Reference Data*, vol. 38, no. 1, pp. 21–29, 2009.

- [38] J. G. Hust and A. B. Lankford, "Thermal Conductivity of Aluminium, Copper, Iron, and Thungsten for temperatures from 1 K To the Melting Point," National Bureau of Standards, Colorado, Tech. Rep., 1984.
- [39] R. Jansson, "Measurement of thermal properties of metals at elevated temperatures," SP Swedish National Testing and Research Institute, Tech. Rep., 2004.
- [40] R. D. McCarty, J. Hord, and H. M. Roder, "Selected properties of hydrogen," *U.S. Department of Commerce*, 1981.
- [41] T. W and H. E. Robinson, "Thermal conductivity of a sample of type 316 stainless steel," *National Bureau of Standards Report*, 1963.
- [42] R. Koech, "Water density formulations and their effect on gravimetric water meter calibration and measurement uncertainties," *Flow Measurement and Instrumentation*, vol. 45, pp. 188–197, 2015.
- [43] M. Chase, "Thermochemical tables, 4th edition," National Institute of Standards and Technology, Tech. Rep., 1998. [Online]. Available: <http://www.nist.gov/pubs/books/jpcrd{-}books.html>
- [44] B. G. Kyle, "Property tables and charts," 1984.
- [45] M. Kaladhar, K. V. Subbaiah, and C. S. Rao, "Machining of austenitic stainless steels - a review," *International Journal of Machining and Machinability of Materials*, vol. 12, no. 1/2, p. 178, 2012. [Online]. Available: <http://www.inderscience.com/link.php?id=48564>

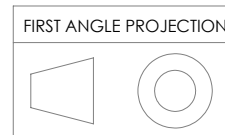
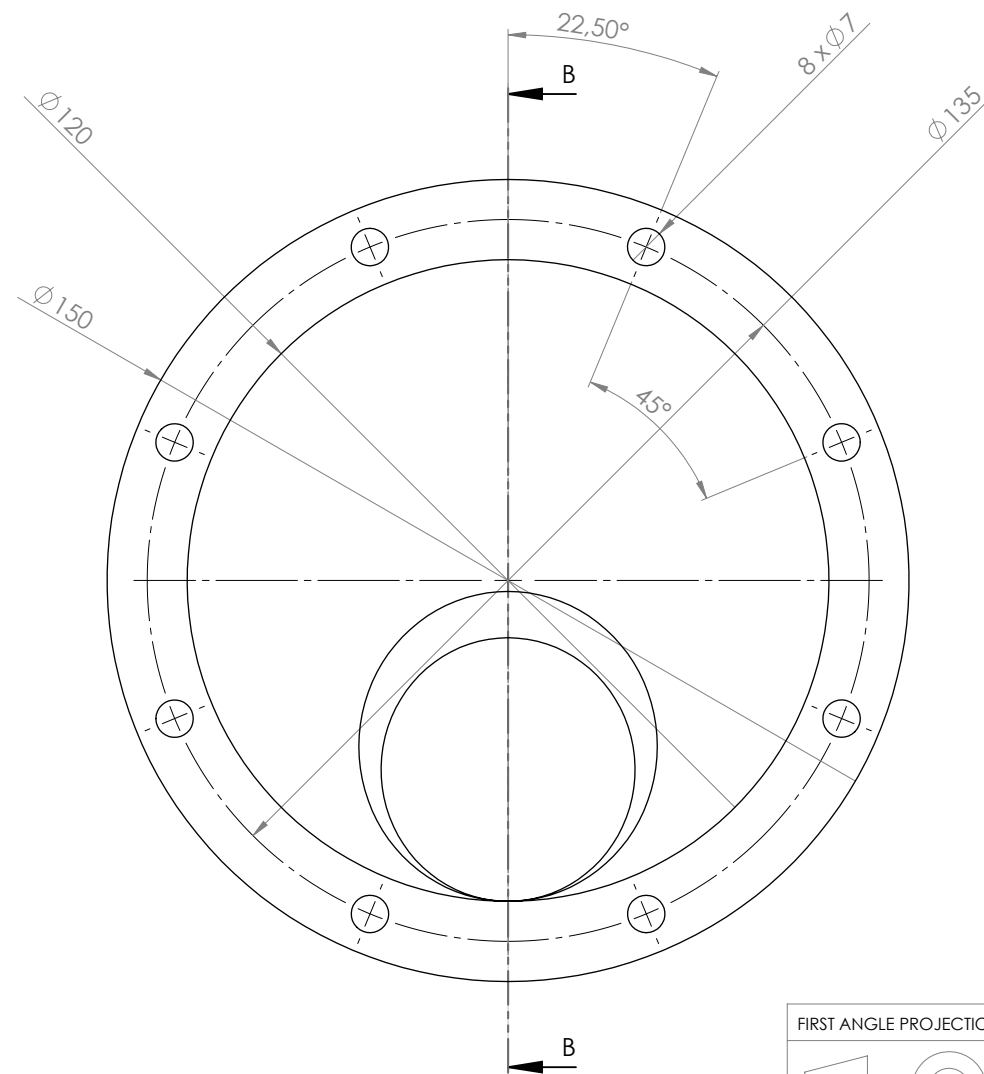
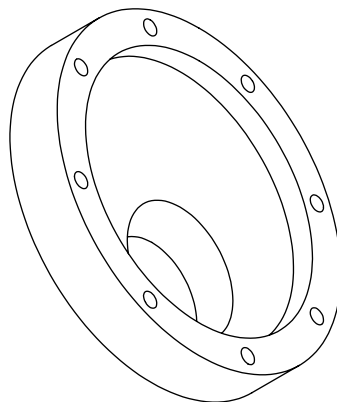
## **Appendix A**

# **Technical drawings**

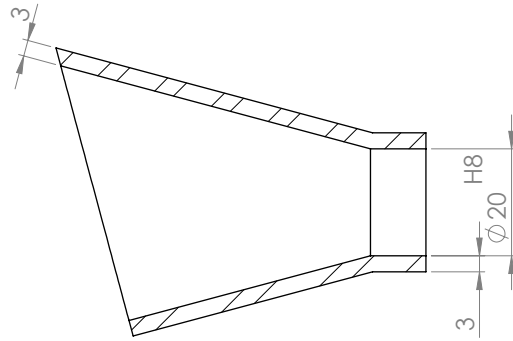
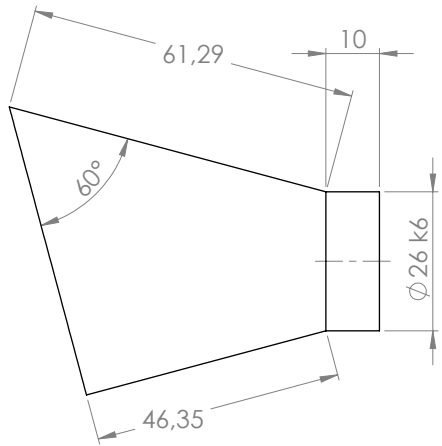


SECTION B-B

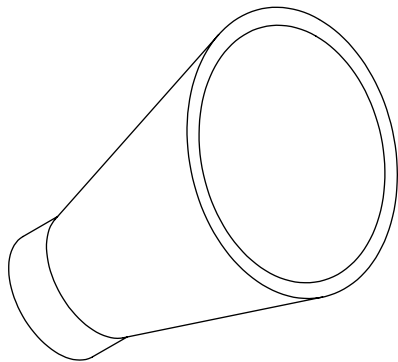
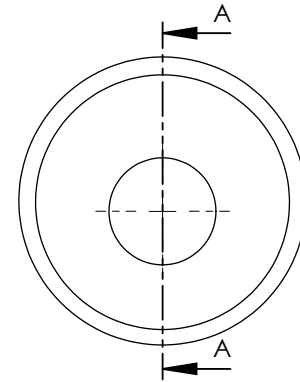
Scale 1:2



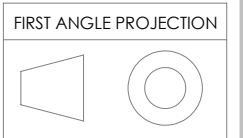
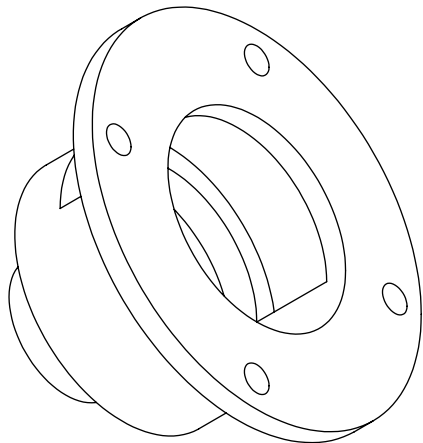
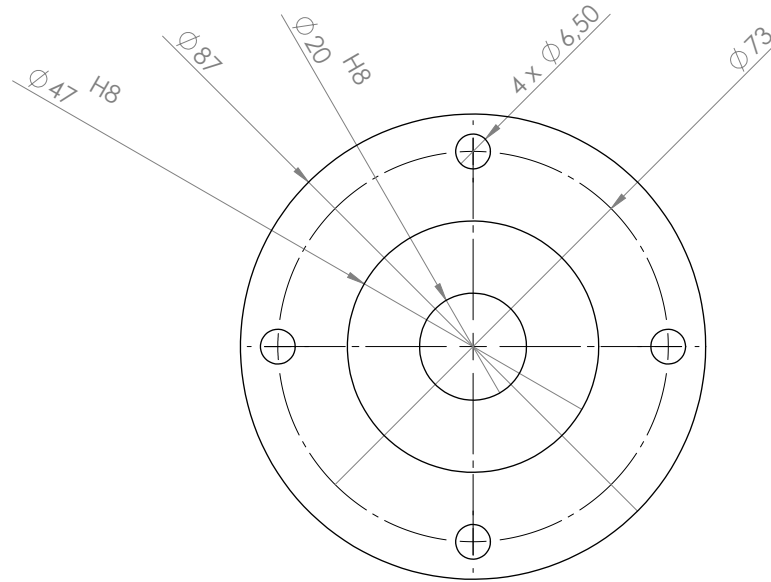
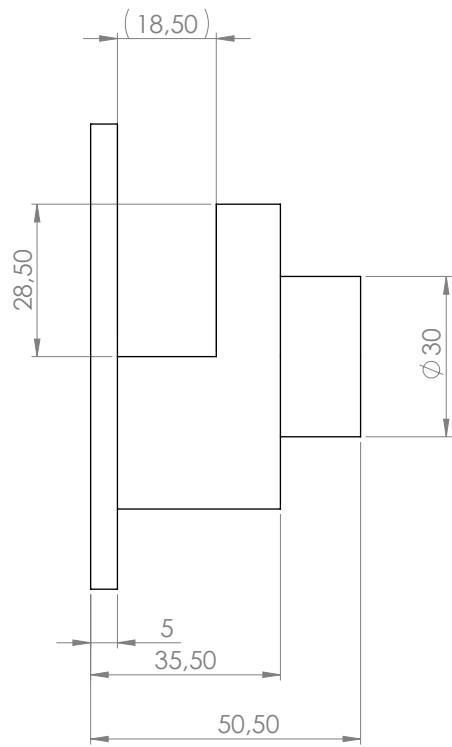
UNLESS OTHERWISE SPECIFIED: DIMENSIONS ARE IN MILLIMETERS SURFACE FINISH: TOLERANCES: LINEAR: ISO 2768-1:m ANGULAR: ISO 2768-2:K			FINISH: /		DEBURR AND BREAK SHARP EDGES		DO NOT SCALE DRAWING		REVISION		
DRAWN JENS VERSCHOREN			SIGNATURE		DATE		TITLE:		BACK-PLATE		
CHK'D JOPPE RITTEN					26/02						
APPV'D JOPPE RITTEN					27/02						
MFG											
Q.A							MATERIAL:		316L SS		DWG NO.
							WEIGHT: 2.3 kg		Drawing 1		A3
							SCALE:1:1		SHEET 1 OF 1		



SECTION A-A



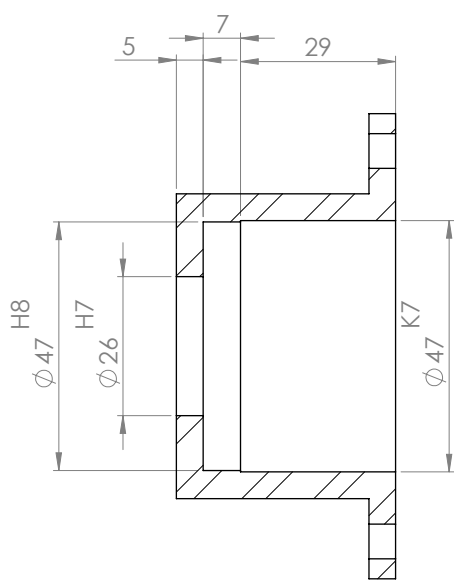
UNLESS OTHERWISE SPECIFIED: DIMENSIONS ARE IN MILLIMETERS SURFACE FINISH: / TOLERANCES: LINEAR: ISO 2768-1:m ANGULAR: ISO 2768-2:K				FINISH: /		DEBURR AND BREAK SHARP EDGES		DO NOT SCALE DRAWING		REVISION			
DRAWN Jens Verschoren								TITLE: Conical duct					
CHK'D Joppe Rutten													
APPV'D Joppe Rutten													
MFG													
Q.A								MATERIAL: 316L SS		DWG NO. Drawing2		A3	
								WEIGHT: 0.2 kg		SCALE: 1:1		SHEET 1 OF 1	



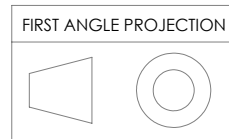
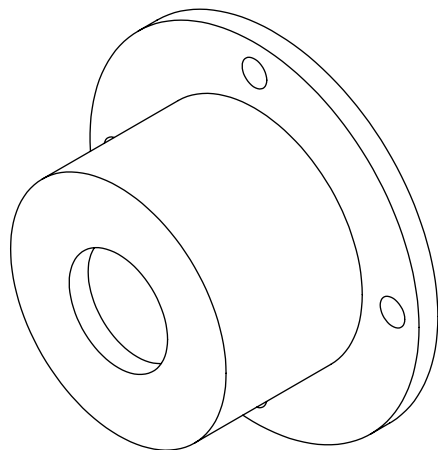
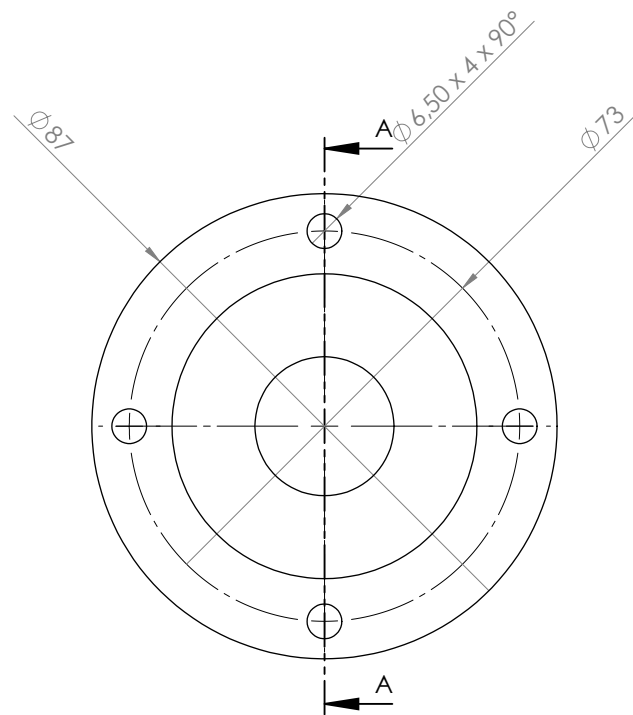
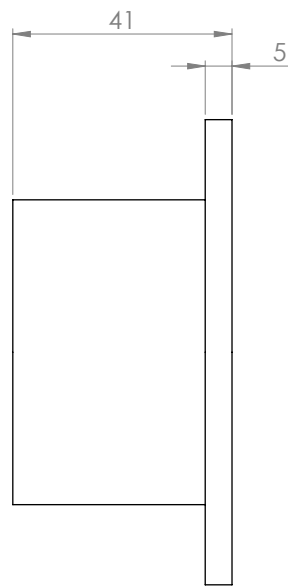
UNLESS OTHERWISE SPECIFIED: DIMENSIONS ARE IN MILLIMETERS SURFACE FINISH: / TOLERANCES: LINEAR: ISO 2768-1:m ANGULAR: ISO 2768-2:k			FINISH: /		DEBURR AND BREAK SHARP EDGES		DO NOT SCALE DRAWING		REVISION		
DRAWN		NAME		SIGNATURE		DATE		TITLE:			
CHK'D		JENS VERSCHOREN				28/02		RIGHT HUB			
APPV'D		JOPPE RUITEN				30/02					
MFG		JOPPE RUITEN				30/02					
Q.A								MATERIAL:		DWG NO.	
								316L SS		Drawing 3	
								WEIGHT: 0.4 kg		SCALE: 1:1	
										SHEET 1 OF 1	

A3

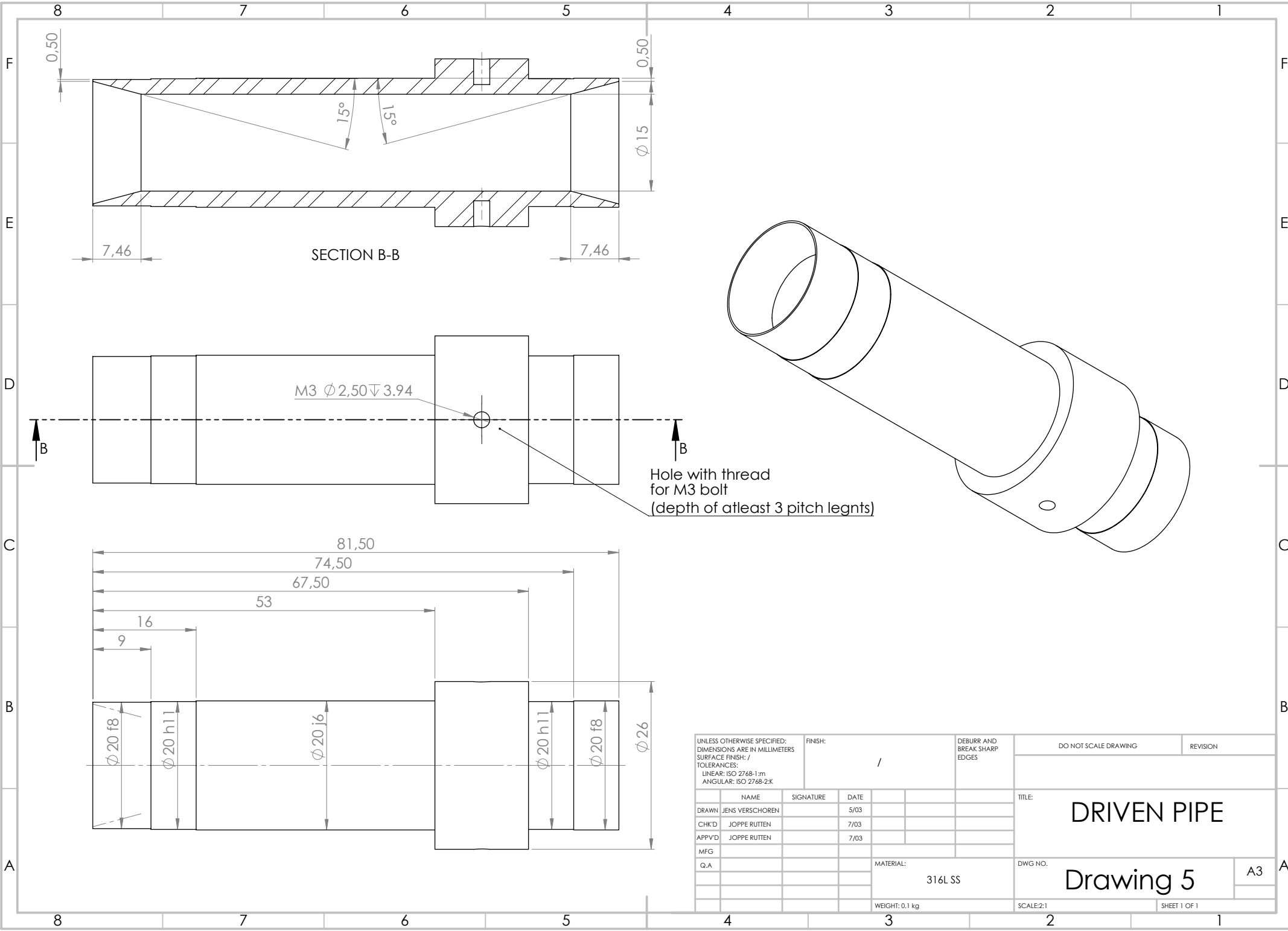




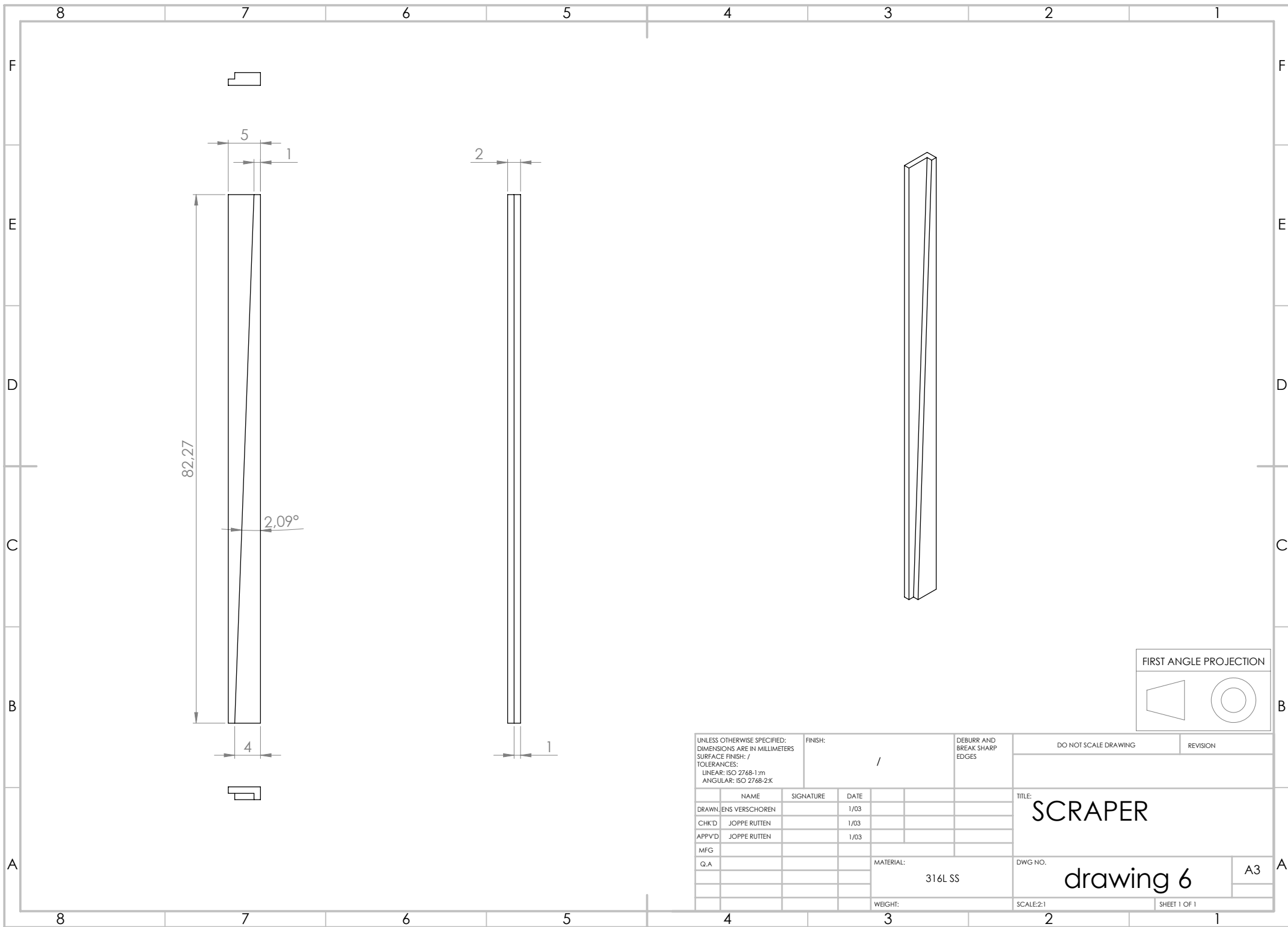
SECTION A-A



UNLESS OTHERWISE SPECIFIED: DIMENSIONS ARE IN MILLIMETERS SURFACE FINISH: / TOLERANCES: LINEAR: ISO 2768-1:m ANGULAR: ISO 2768-2:k			FINISH: /		DEBURR AND BREAK SHARP EDGES		DO NOT SCALE DRAWING		REVISION		
DRAWN JENS VERSCHOREN			SIGNATURE		DATE		TITLE:		LEFT HUB		
CHK'D JOPPE RUITEN					30/02						
APPV'D JOPPE RUITEN					30/02				Drawing 4		
MFG											
Q.A							MATERIAL:		DWG NO.		A3
							316L SS		SCALE:1:1		SHEET 1 OF 1
							WEIGHT: 0.45 kg				



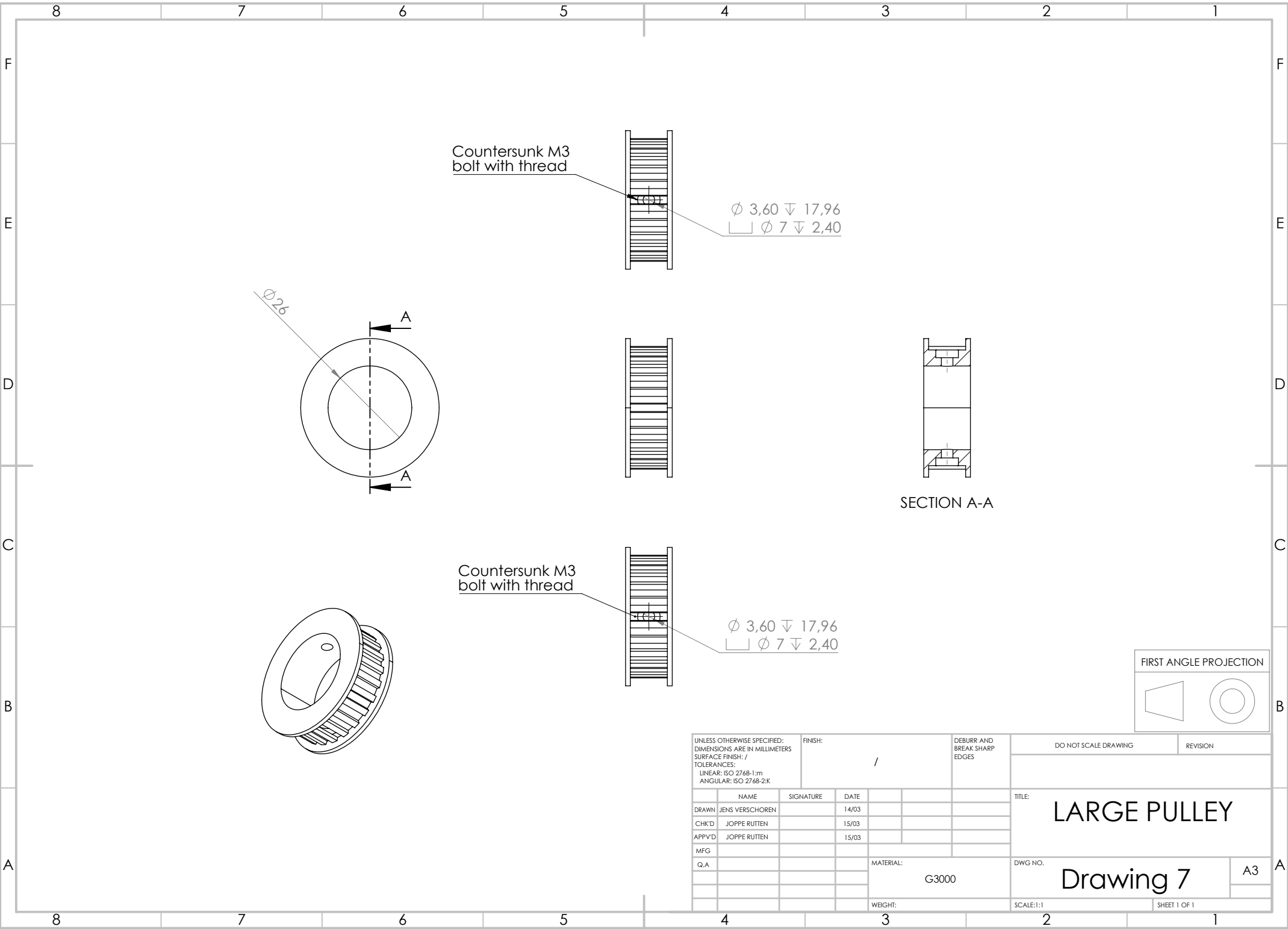
UNLESS OTHERWISE SPECIFIED: DIMENSIONS ARE IN MILLIMETERS SURFACE FINISH: / TOLERANCES: LINEAR: ISO 2768-1:m ANGULAR: ISO 2768-2:k			FINISH: /		DEBURR AND BREAK SHARP EDGES		DO NOT SCALE DRAWING		REVISION		
DRAWN JENS VERSCHOREN			SIGNATURE		DATE		TITLE:		DRIVEN PIPE		
CHK'D JOPPE RITTEN					7/03						
APPV'D JOPPE RITTEN					7/03						
MFG											
Q.A							MATERIAL:		316L SS		DWG NO.
							WEIGHT: 0.1 kg		SCALE: 2:1		A3
									SHEET 1 OF 1		



FIRST ANGLE PROJECTION

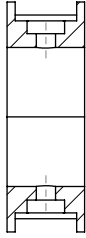
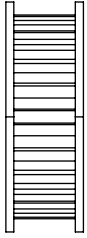
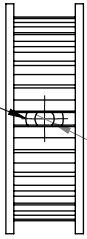
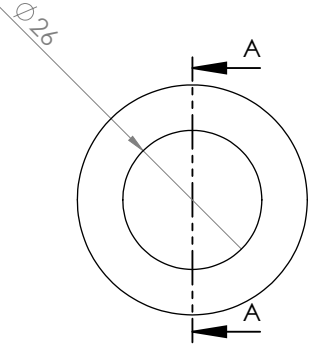


UNLESS OTHERWISE SPECIFIED: DIMENSIONS ARE IN MILLIMETERS SURFACE FINISH: / TOLERANCES: LINEAR: ISO 2768-1:m ANGULAR: ISO 2768-2:K			FINISH: /		DEBURR AND BREAK SHARP EDGES		DO NOT SCALE DRAWING		REVISION		
							TITLE: <b>SCRAPER</b>				
DRAWN: ENS VERSCHOREN		SIGNATURE		DATE							
CHK'D: JOPPE RUITEN				1/03							
APPV'D: JOPPE RUITEN				1/03							
MFG											
Q.A						MATERIAL: 316L SS		DWG NO.		A3	
						WEIGHT:		SCALE:2:1		SHEET 1 OF 1	
								drawing 6			



Countersunk M3  
bolt with thread

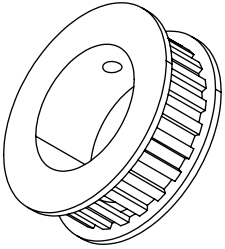
$\phi 3,60 \nabla 17,96$   
 $\square \phi 7 \nabla 2,40$



SECTION A-A

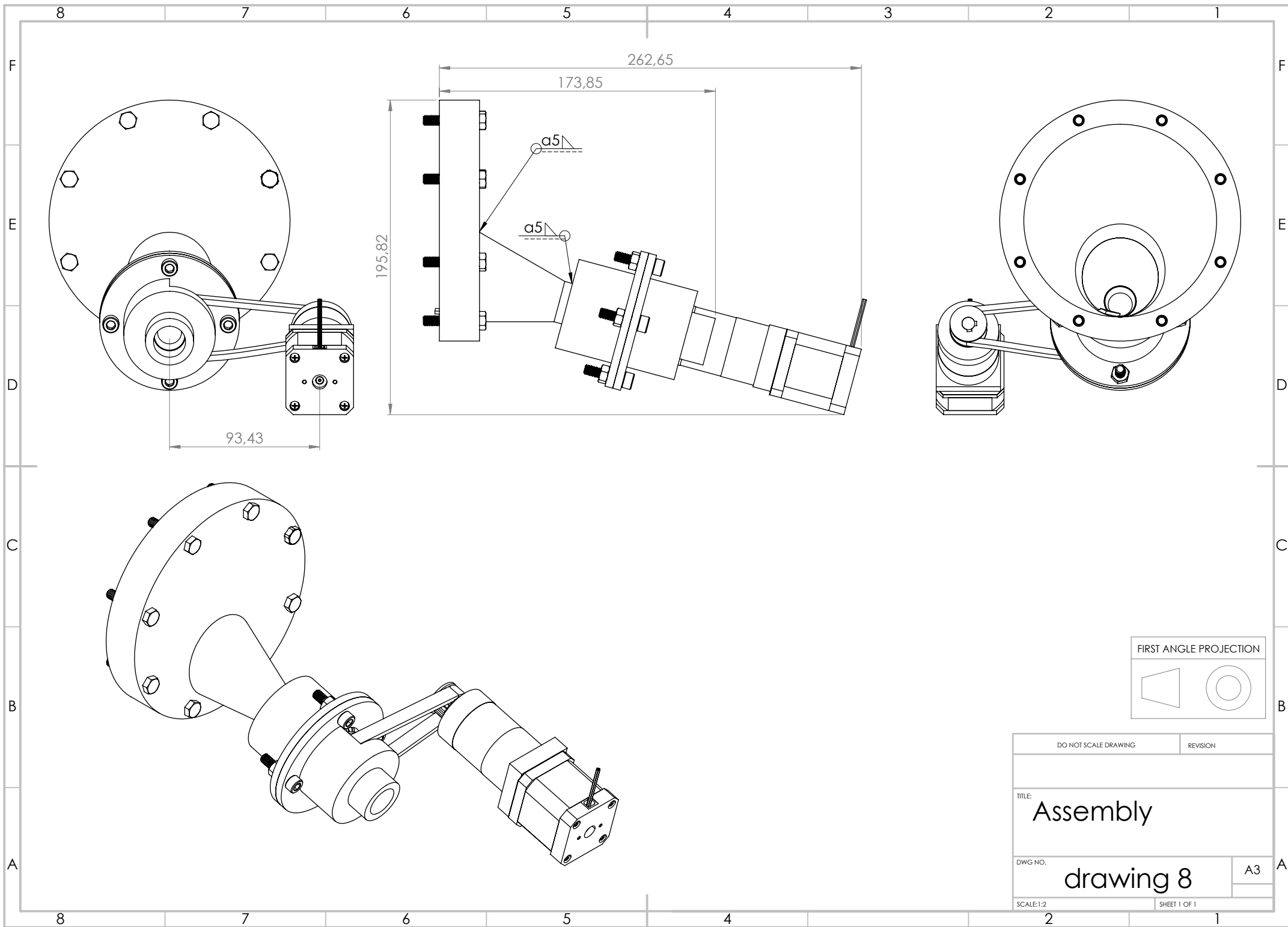
Countersunk M3  
bolt with thread

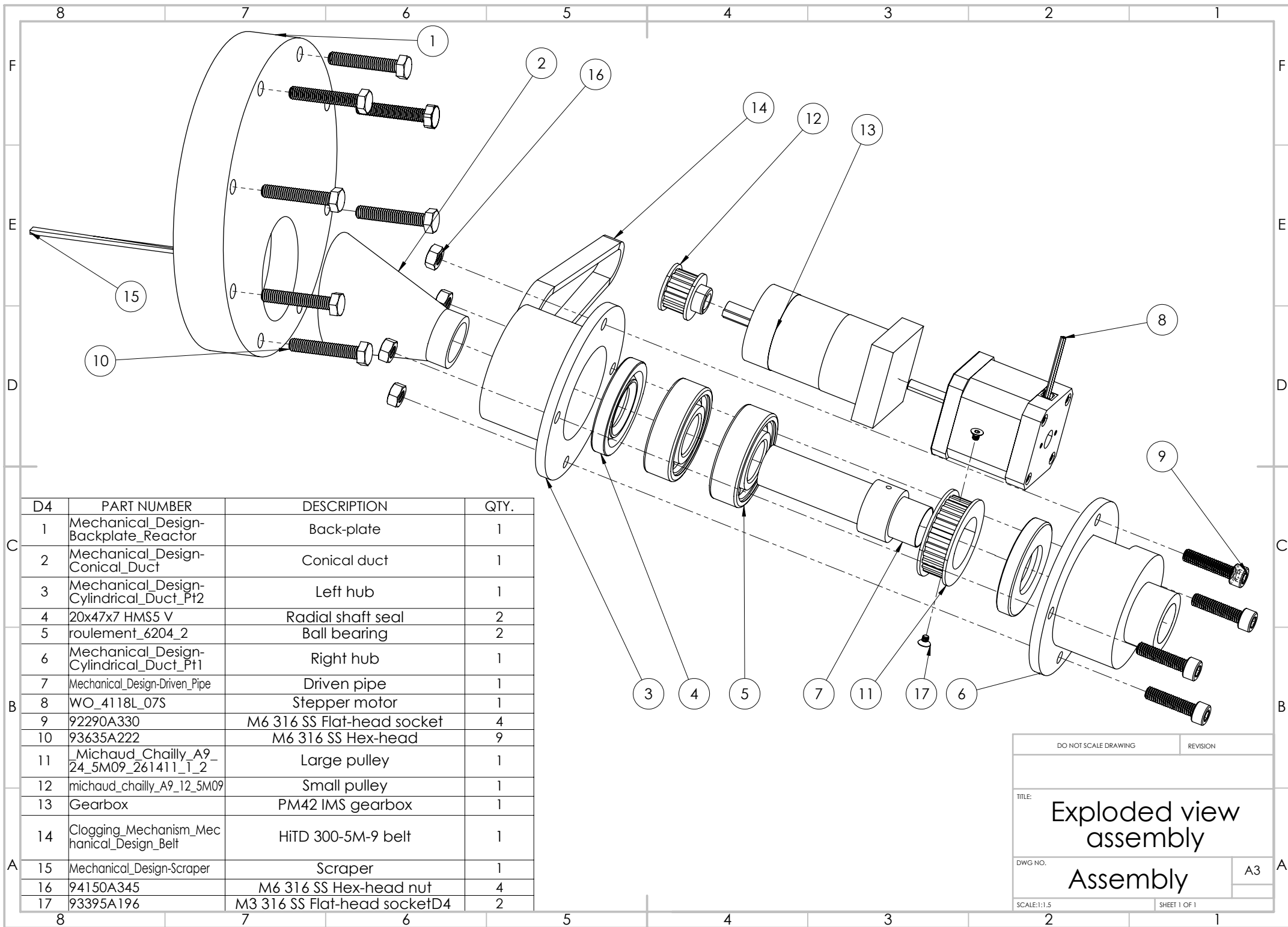
$\phi 3,60 \nabla 17,96$   
 $\square \phi 7 \nabla 2,40$



FIRST ANGLE PROJECTION

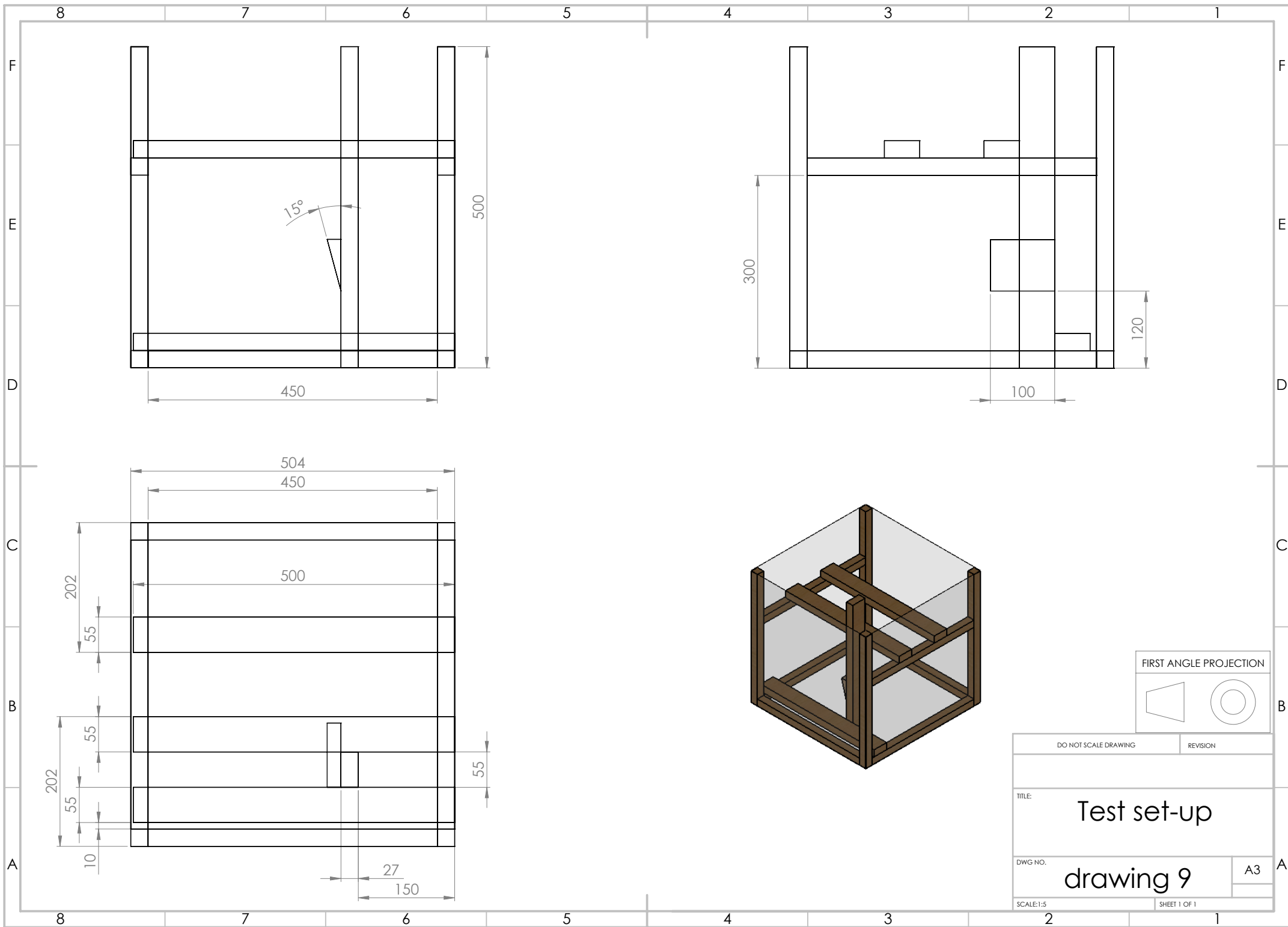
UNLESS OTHERWISE SPECIFIED: DIMENSIONS ARE IN MILLIMETERS SURFACE FINISH: / TOLERANCES: LINEAR: ISO 2768-1:m ANGULAR: ISO 2768-2:K			FINISH: /		DEBURR AND BREAK SHARP EDGES		DO NOT SCALE DRAWING		REVISION		
DRAWN JENS VERSCHOREN			SIGNATURE		DATE		TITLE:		LARGE PULLEY		
CHK'D JOPPE RUITEN					14/03						
APPV'D JOPPE RUITEN					15/03						
MFG											
Q.A							MATERIAL:		DWG NO.		A3
							G3000		Drawing 7		
							WEIGHT:		SCALE:1:1		SHEET 1 OF 1





D4	PART NUMBER	DESCRIPTION	QTY.
1	Mechanical_Design-Backplate_Reactor	Back-plate	1
2	Mechanical_Design-Conical_Duct	Conical duct	1
3	Mechanical_Design-Cylindrical_Duct_Pt2	Left hub	1
4	20x47x7 HMS5 V	Radial shaft seal	2
5	roulement_6204_2	Ball bearing	2
6	Mechanical_Design-Cylindrical_Duct_Pt1	Right hub	1
7	Mechanical_Design-Driven_Pipe	Driven pipe	1
8	WO_4118L_07S	Stepper motor	1
9	92290A330	M6 316 SS Flat-head socket	4
10	93635A222	M6 316 SS Hex-head	9
11	_Michaud_Chailly_A9_24_5M09_261411_T_2	Large pulley	1
12	michaud_chailly_A9_12_5M09	Small pulley	1
13	Gearbox	PM42 IMS gearbox	1
14	Clogging_Mechanism_Mechanical_Design_Belt	HiTD 300-5M-9 belt	1
15	Mechanical_Design-Scraper	Scraper	1
16	94150A345	M6 316 SS Hex-head nut	4
17	93395A196	M3 316 SS Flat-head socket	2

DO NOT SCALE DRAWING		REVISION
TITLE: <b>Exploded view assembly</b>		
DWG NO. <b>Assembly</b>		A3
SCALE:1:1.5	SHEET 1 OF 1	



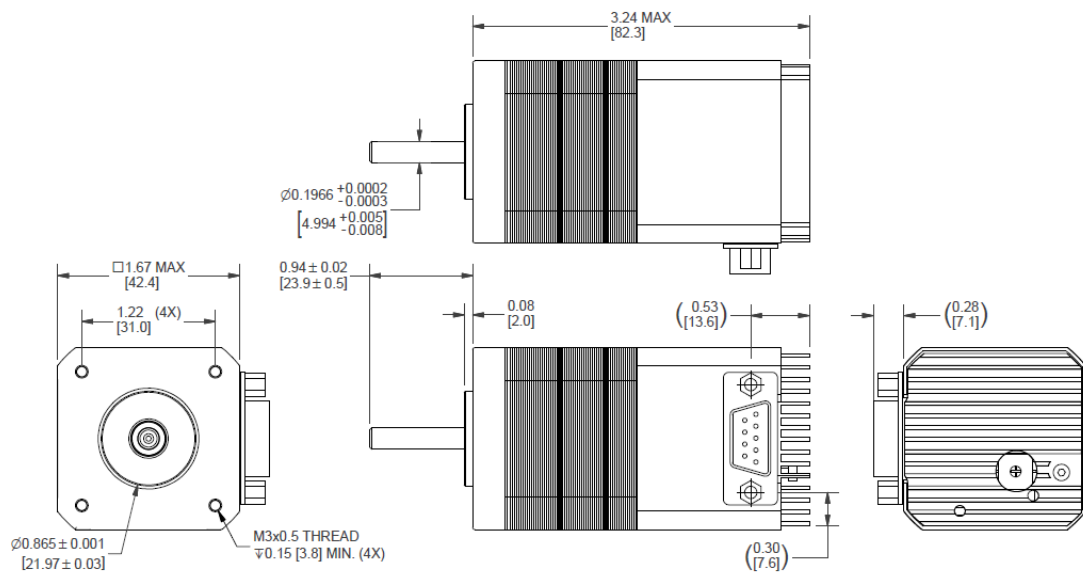




## Appendix B

# Motor and reduction

### B.1 Dimensions



## B.2 Motor Control

# SilverPak 17C/CE

## MOTOR + CONTROLLER + DRIVER

### MAIN FEATURES:

- Voltage: +12 to 40VDC
- Current: 0.2 to 2.0 Amps Peak, programmable in terms of percentage of max possible current
- Hold current: 0.2 to 1.0 Amps, programmable up to 50% of max possible run current
- Step resolution: 1x, 2x, 4x, 8x, 16x, 32x, 64x, 128x, 256x
- Speed: (max step frequency: 16.8MHz)
- Inputs: 2 I/O's, 1 input for homing to an opto sensor, 1 input for a switch closure to ground (Total of 2 I/O's and 2 inputs)
- RS485 communication
- Stand alone operation, can store programs on EEPROM and run upon power up
- NEW: Able to use inputs 1 & 2 as limit switches

### DETAILED FEATURES:

- Operating temperature: -20 to 50°C

### INCLUDED ACCESSORIES:

- 090-00022 cable for DB-9 cable comes with each unit (with a red 4-pin connector for the RS232-485 converter card)



- 090-00018 cable for motor comes with each unit (the other side is 4 flying lead wires)



### OPTIONAL ACCESSORIES:

(Available for an additional cost)

- Designer's kit: RS232-to-485 with push button, opto sensor, CD-ROM, cables (2)



- Designer's kit with USB485 converter card (USB485, push button, switch, CD, cables)



### CONNECTION SPECIFICATIONS:

Pin #	Color	Function	Input
1	Red	+V (Main power in)	
2	Black	I/O	1
3	Brown	RS485B (-)	
4	Black/White	RS485A (+)	
5	Orange	Switch Closure to GND (IN)	4
6	Green	GND (-V of main power in)	
7	White	Opto Sensor Phototransistor (IN)	3
8	Blue	I/O	2
9	Yellow	Opto Sensor LED (Power Out)	

### PROGRAMMING:

- Programming the R256 is simple and intuitive in HyperTerminal. Programs always begin with a forward slash "/", and address number, then one alpha character and then the value:

/1A5000R

This stands for Absolute position 5000, and will rotate 5000 steps

/1A5000A0R

This will rotate to position 5000, then back to position 0

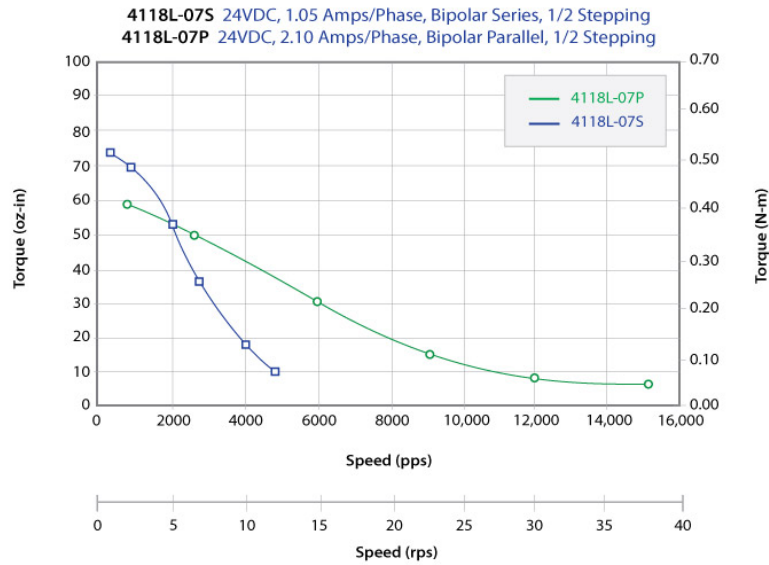
/1gA5000A0G5R

This will rotate to position 5000, then back to 0, looping 5 times (commands between the 'g' and 'G' will be repeated, or in a loop)

/1s0gA5000A0G5R

By typing 's0', this means to store the following commands in the EEPROM and run this program upon power up.

### B.3 Torque curve



### B.4 Gearbox

IMS.baseline

PM 42/LN

#### PM 42/LN Ø42 mm, Metal-Low-Noise

Parameter	1-stage	2-stage	3-stage
Perm. output torque $T_{out}$ (Appl. factor $C_s = 1.0$ )	3.0 Nm	7.5 Nm	15.0 Nm
Gearbox efficiency, approx.	0.80	0.75	0.70
Max. backlash	0.90 °DEC*	0.95 °DEC	1.00 °DEC
Recommended initial speed	3,000 U/min	3,000 U/min	3,000 U/min
Min. Operating temperature	-30 °C	-30 °C	-30 °C
Max. Operating temperature	+120 °C	+120 °C	+120 °C

\* LN: 1.30 °DEC. For plastic PL wheels only! Impact of 1st stage for 2-4 stage versions is negligible.

Output side with ball bearing (2RS)	1-stage	2-stage	3-stage
Max. load, radial (Middle output shaft)	160 N	230 N	300 N
Max. load, axial	50 N	80 N	110 N
Max. perm. fitting pressure	320 N	320 N	320 N
Weight approx.	275 g	385 g	500 g

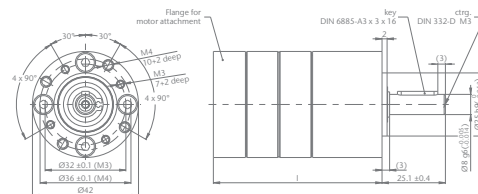
Gearbox length in mm	1-stage	2-stage	3-stage
Length l*	49.1 ± 0.5	62.2 ± 0.5	75.3 ± 0.5

\* The minimum length is only possible with an optimal attachment to the motor, the actual length we like to determine for you.

#### Current reduction ratios i rounded

1-stage		2-stage		3-stage	
PM	LN	PM	LN	PM	LN
4:1 (3.71)	4:1 (3.65)	14:1 (13.73)	14:1 (13.53)	51:1 (50.89)	50:1 (50.16)
4:1 (4.29)	5:1 (4.59)	16:1 (15.88)	16:1 (15.65)	59:1 (58.86)	58:1 (58.01)
5:1 (5.18)	5:1 (5.36)	18:1 (18.37)	17:1 (17.00)	68:1 (68.07)	67:1 (67.08)
7:1 (6.75)	7:1 (6.55)	19:1 (19.20)	19:1 (18.92)	71:1 (71.16)	70:1 (70.13)
	9:1 (8.63)	22:1 (22.21)	23:1 (22.96)	79:1 (78.72)	81:1 (81.11)
	*13:1 (13.20)	25:1 (25.01)	25:1 (24.65)	93:1 (92.70)	91:1 (91.36)
		27:1 (26.85)	28:1 (27.76)	95:1 (95.18)	98:1 (98.07)
		29:1 (28.93)	28:1 (28.05)	100:1 (99.51)	102:1 (101.89)
		35:1 (34.98)	34:1 (33.92)	107:1 (107.21)	106:1 (105.65)
		46:1 (45.56)	45:1 (44.69)	115:1 (115.08)	115:1 (114.77)
			58:1 (58.22)	124:1 (123.98)	123:1 (123.20)
			*68:1 (68.40)	130:1 (129.62)	128:1 (127.74)
			*89:1 (89.10)	139:1 (139.14)	137:1 (136.99)
				150:1 (149.90)	145:1 (145.36)
				169:1 (168.85)	166:1 (166.40)
				181:1 (181.25)	176:1 (175.75)
				195:1 (195.27)	192:1 (191.54)
				236:1 (236.10)	232:1 (231.59)
				308:1 (307.55)	302:1 (301.68)
					393:1 (392.98)
					*462:1 (461.70)
					*601:1 (601.43)

\* not all reduction ratios available ex-stock



All figures are approximate values. Variations are possible and may arise for example due to non-standardized inspection and measurement methods. For more detailed information, please contact us directly. The company always reserves the right to make technical modifications. For current status, please consult [www.imsagar.com](http://www.imsagar.com)



## **Appendix C**

# **Heat transfer analysis**

### C.1 Properties of Hydrogen

TABLE 2  
THERMODYNAMIC PROPERTIES OF PARAHYDROGEN (ISOBARS, SI UNITS)

.101325 MPA ISOBAR

TEMPERATURE K	VOLUME CU M/KG	ISOTHERM DERIVATIVE CU M-MPA/KG	ISOCHORE DERIVATIVE MPA/K	INTERNAL ENERGY KJ/KG-K	ENTHALPY KJ/KG	ENTROPY KJ/KG-K	CV KJ /	CP KG-K	VELOCITY OF SOUND M/S
* 13.835	.01298	1.1686	.9244	-308.9	-307.6	4.968	4.68	6.38	1263.
14.	.01300	1.1444	.9243	-307.8	-306.5	5.047	4.71	6.48	1254.
15.	.01314	1.0411	.9105	-301.1	-299.8	5.508	4.92	6.98	1216.
16.	.01330	.9750	.8926	-293.9	-292.6	5.974	5.12	7.43	1190.
17.	.01347	.9113	.8775	-286.3	-284.9	6.440	5.30	7.90	1166.
18.	.01365	.8502	.8630	-278.1	-276.7	6.906	5.47	8.41	1143.
19.	.01385	.7854	.8477	-269.5	-268.1	7.375	5.62	8.95	1119.
20.	.01406	.7222	.8305	-260.3	-258.8	7.848	5.75	9.52	1094.
* 20.268	.01413	.7053	.8253	-257.7	-256.2	7.977	5.78	9.66	1089.
* 20.268	.01433	.6675	.8058	113.6	189.3	29.967	6.50	12.15	355.
21.	.78035	.0715	.0055	118.8	197.9	30.383	6.44	11.89	363.
22.	.82689	.0768	.0052	125.9	209.7	30.929	6.37	11.52	374.
23.	.87260	.0820	.0049	132.8	221.2	31.442	6.33	11.43	385.
24.	.91769	.0876	.0046	139.6	232.5	31.925	6.31	11.29	395.
25.	.96226	.0919	.0044	146.3	243.8	32.383	6.29	11.17	404.
26.	1.00643	.0968	.0042	152.9	254.9	32.819	6.27	11.08	413.
27.	1.05025	.1015	.0040	159.5	265.9	33.236	6.26	11.00	422.
28.	1.09378	.1062	.0039	166.1	276.9	33.635	6.26	10.94	431.
29.	1.13705	.1109	.0037	172.6	287.8	34.018	6.25	10.88	439.
30.	1.18011	.1154	.0036	179.1	298.7	34.386	6.25	10.83	448.
31.	1.22297	.1200	.0034	185.6	309.5	34.741	6.24	10.79	456.
32.	1.26567	.1245	.0033	192.0	320.3	35.083	6.24	10.76	463.
33.	1.30822	.1290	.0032	198.4	331.0	35.413	6.23	10.72	471.
34.	1.35063	.1335	.0031	204.9	341.7	35.733	6.23	10.69	479.
35.	1.43512	.1424	.0029	217.6	363.0	36.343	6.23	10.65	493.
38.	1.51922	.1512	.0027	230.4	384.3	36.917	6.22	10.61	508.
40.	1.60300	.1599	.0026	243.1	405.5	37.461	6.22	10.58	521.
42.	1.68652	.1686	.0025	255.7	426.6	37.976	6.23	10.56	535.
44.	1.76982	.1772	.0024	268.4	447.7	38.467	6.23	10.54	547.
46.	1.85292	.1858	.0022	281.0	468.8	38.935	6.25	10.53	560.
48.	1.93587	.1943	.0021	293.7	489.9	39.384	6.26	10.53	572.
50.	2.01867	.2029	.0021	306.4	510.9	39.814	6.28	10.54	583.
52.	2.10135	.2114	.0020	319.1	532.0	40.228	6.31	10.56	595.
56.	2.29641	.2283	.0018	344.7	574.4	41.012	6.39	10.62	616.
60.	2.43113	.2452	.0017	370.7	617.0	41.748	6.50	10.71	636.
65.	2.63666	.2662	.0016	403.9	671.0	42.612	6.69	10.89	658.
70.	2.84187	.2872	.0015	438.1	726.0	43.427	6.94	11.13	679.
75.	3.04684	.3081	.0014	473.7	782.4	44.205	7.25	11.42	697.
80.	3.25161	.3290	.0013	510.9	840.4	44.953	7.60	11.77	714.
90.	3.66069	.3706	.0011	591.1	962.0	46.384	8.41	12.57	744.
100.	4.06933	.4122	.0010	679.6	1091.9	47.753	9.27	13.43	773.
110.	4.47765	.4537	.0009	776.6	1230.3	49.069	10.10	14.25	800.
120.	4.88574	.4952	.0008	881.5	1376.6	50.341	10.83	14.97	827.
130.	5.29365	.5366	.0008	992.9	1529.3	51.563	11.40	15.54	855.
140.	5.70143	.5780	.0007	1109.2	1686.9	52.731	11.82	15.96	883.
160.	6.51668	.6607	.0006	1350.5	2010.8	54.893	12.21	16.35	940.
180.	7.33165	.7434	.0006	1595.1	2338.0	56.820	12.19	16.32	998.
200.	8.14642	.8260	.0005	1836.7	2662.1	58.527	11.95	16.08	1054.
220.	8.96105	.9086	.0005	2072.5	2980.5	60.045	11.63	15.76	1110.
240.	9.77598	.9911	.0004	2302.1	3292.6	61.403	11.33	15.46	1163.
260.	10.59003	1.0737	.0004	2526.1	3599.1	62.630	11.07	15.20	1214.
280.	11.40442	1.1563	.0004	2745.5	3901.0	63.749	10.87	15.00	1263.
300.	12.21786	1.2387	.0003	2961.4	4199.4	64.778	10.72	14.85	1310.
350.	14.25342	1.4450	.0003	3491.4	4935.6	67.047	10.51	14.63	1419.
400.	16.28883	1.6513	.0003	4014.4	5664.9	68.996	10.43	14.55	1518.
450.	18.32416	1.8575	.0002	4534.7	6391.4	70.708	10.41	14.53	1611.
500.	20.35943	2.0638	.0002	5055.0	7117.9	72.238	10.40	14.52	1698.
550.	22.39466	2.2700	.0002	5575.0	7844.1	73.623	10.41	14.53	1780.
600.	24.42987	2.4762	.0002	6096.0	8571.3	74.887	10.42	14.55	1859.
700.	28.50024	2.8887	.0001	7140.9	10028.7	77.134	10.48	14.61	2006.
800.	32.57056	3.3011	.0001	8193.4	11493.6	79.089	10.57	14.70	2142.
900.	36.64086	3.7135	.0001	9256.7	12969.3	80.826	10.70	14.82	2268.
1000.	40.71114	4.1259	.0001	10333.9	14459.0	82.398	10.86	14.98	2386.
1200.	48.85168	4.9508	.0001	12544.2	17494.1	85.151	11.24	15.37	2601.
1400.	56.99233	5.7756	.0001	14837.2	20611.9	87.558	11.68	15.91	2795.
1600.	65.13445	6.6005	.0001	17220.5	23820.2	89.677	12.15	16.28	2974.
1800.	73.27628	7.4253	.0001	19714.9	27140.7	91.594	12.77	16.92	3135.
2000.	81.41790	8.2501	.0001	22393.8	30649.8	93.508	13.97	18.18	3277.
2200.	89.80607	9.0750	.0000	2533.9	3433.5	96.029	16.44	20.86	3393.
2400.	98.47087	9.8998	.0000	29215.1	39192.6	99.100	21.25	26.17	3491.
2600.	107.86410	10.7247	.0000	34370.5	45299.9	102.842	29.64	35.53	3588.
2800.	118.63048	11.5495	.0000	41829.7	53849.9	107.400	42.80	50.89	3702.
3000.	131.72066	12.3743	.0000	52805.4	66152.0	112.936	61.40	73.34	3839.

\* TWO-PHASE BOUNDARY

## C.2 Properties of air

884

APPENDIX 1

TABLE A-15

Properties of air at 1 atm pressure

Temp. $T, ^\circ\text{C}$	Density $\rho, \text{kg/m}^3$	Specific Heat $c_p, \text{J/kg}\cdot\text{K}$	Thermal Conductivity $k, \text{W/m}\cdot\text{K}$	Thermal Diffusivity $\alpha, \text{m}^2/\text{s}$	Dynamic Viscosity $\mu, \text{kg/m}\cdot\text{s}$	Kinematic Viscosity $\nu, \text{m}^2/\text{s}$	Prandtl Number Pr
-150	2.866	983	0.01171	$4.158 \times 10^{-6}$	$8.636 \times 10^{-6}$	$3.013 \times 10^{-6}$	0.7246
-100	2.038	966	0.01582	$8.036 \times 10^{-6}$	$1.189 \times 10^{-5}$	$5.837 \times 10^{-6}$	0.7263
-50	1.582	999	0.01979	$1.252 \times 10^{-5}$	$1.474 \times 10^{-5}$	$9.319 \times 10^{-6}$	0.7440
-40	1.514	1002	0.02057	$1.356 \times 10^{-5}$	$1.527 \times 10^{-5}$	$1.008 \times 10^{-5}$	0.7436
-30	1.451	1004	0.02134	$1.465 \times 10^{-5}$	$1.579 \times 10^{-5}$	$1.087 \times 10^{-5}$	0.7425
-20	1.394	1005	0.02211	$1.578 \times 10^{-5}$	$1.630 \times 10^{-5}$	$1.169 \times 10^{-5}$	0.7408
-10	1.341	1006	0.02288	$1.696 \times 10^{-5}$	$1.680 \times 10^{-5}$	$1.252 \times 10^{-5}$	0.7387
0	1.292	1006	0.02364	$1.818 \times 10^{-5}$	$1.729 \times 10^{-5}$	$1.338 \times 10^{-5}$	0.7362
5	1.269	1006	0.02401	$1.880 \times 10^{-5}$	$1.754 \times 10^{-5}$	$1.382 \times 10^{-5}$	0.7350
10	1.246	1006	0.02439	$1.944 \times 10^{-5}$	$1.778 \times 10^{-5}$	$1.426 \times 10^{-5}$	0.7336
15	1.225	1007	0.02476	$2.009 \times 10^{-5}$	$1.802 \times 10^{-5}$	$1.470 \times 10^{-5}$	0.7323
20	1.204	1007	0.02514	$2.074 \times 10^{-5}$	$1.825 \times 10^{-5}$	$1.516 \times 10^{-5}$	0.7309
25	1.184	1007	0.02551	$2.141 \times 10^{-5}$	$1.849 \times 10^{-5}$	$1.562 \times 10^{-5}$	0.7296
30	1.164	1007	0.02588	$2.208 \times 10^{-5}$	$1.872 \times 10^{-5}$	$1.608 \times 10^{-5}$	0.7282
35	1.145	1007	0.02625	$2.277 \times 10^{-5}$	$1.895 \times 10^{-5}$	$1.655 \times 10^{-5}$	0.7268
40	1.127	1007	0.02662	$2.346 \times 10^{-5}$	$1.918 \times 10^{-5}$	$1.702 \times 10^{-5}$	0.7255
45	1.109	1007	0.02699	$2.416 \times 10^{-5}$	$1.941 \times 10^{-5}$	$1.750 \times 10^{-5}$	0.7241
50	1.092	1007	0.02735	$2.487 \times 10^{-5}$	$1.963 \times 10^{-5}$	$1.798 \times 10^{-5}$	0.7228
60	1.059	1007	0.02808	$2.632 \times 10^{-5}$	$2.008 \times 10^{-5}$	$1.896 \times 10^{-5}$	0.7202
70	1.028	1007	0.02881	$2.780 \times 10^{-5}$	$2.052 \times 10^{-5}$	$1.995 \times 10^{-5}$	0.7177
80	0.9994	1008	0.02953	$2.931 \times 10^{-5}$	$2.096 \times 10^{-5}$	$2.097 \times 10^{-5}$	0.7154
90	0.9718	1008	0.03024	$3.086 \times 10^{-5}$	$2.139 \times 10^{-5}$	$2.201 \times 10^{-5}$	0.7132
100	0.9458	1009	0.03095	$3.243 \times 10^{-5}$	$2.181 \times 10^{-5}$	$2.306 \times 10^{-5}$	0.7111
120	0.8977	1011	0.03235	$3.565 \times 10^{-5}$	$2.264 \times 10^{-5}$	$2.522 \times 10^{-5}$	0.7073
140	0.8542	1013	0.03374	$3.898 \times 10^{-5}$	$2.345 \times 10^{-5}$	$2.745 \times 10^{-5}$	0.7041
160	0.8148	1016	0.03511	$4.241 \times 10^{-5}$	$2.420 \times 10^{-5}$	$2.975 \times 10^{-5}$	0.7014
180	0.7788	1019	0.03646	$4.593 \times 10^{-5}$	$2.504 \times 10^{-5}$	$3.212 \times 10^{-5}$	0.6992
200	0.7459	1023	0.03779	$4.954 \times 10^{-5}$	$2.577 \times 10^{-5}$	$3.455 \times 10^{-5}$	0.6974
250	0.6746	1033	0.04104	$5.890 \times 10^{-5}$	$2.760 \times 10^{-5}$	$4.091 \times 10^{-5}$	0.6946
300	0.6158	1044	0.04418	$6.871 \times 10^{-5}$	$2.934 \times 10^{-5}$	$4.765 \times 10^{-5}$	0.6935
350	0.5664	1056	0.04721	$7.892 \times 10^{-5}$	$3.101 \times 10^{-5}$	$5.475 \times 10^{-5}$	0.6937
400	0.5243	1069	0.05015	$8.951 \times 10^{-5}$	$3.261 \times 10^{-5}$	$6.219 \times 10^{-5}$	0.6948
450	0.4880	1081	0.05298	$1.004 \times 10^{-4}$	$3.415 \times 10^{-5}$	$6.997 \times 10^{-5}$	0.6965
500	0.4565	1093	0.05572	$1.117 \times 10^{-4}$	$3.563 \times 10^{-5}$	$7.806 \times 10^{-5}$	0.6986
600	0.4042	1115	0.06093	$1.352 \times 10^{-4}$	$3.846 \times 10^{-5}$	$9.515 \times 10^{-5}$	0.7037
700	0.3627	1135	0.06581	$1.598 \times 10^{-4}$	$4.111 \times 10^{-5}$	$1.133 \times 10^{-4}$	0.7092
800	0.3289	1153	0.07037	$1.855 \times 10^{-4}$	$4.362 \times 10^{-5}$	$1.326 \times 10^{-4}$	0.7149
900	0.3008	1169	0.07465	$2.122 \times 10^{-4}$	$4.600 \times 10^{-5}$	$1.529 \times 10^{-4}$	0.7206
1000	0.2772	1184	0.07868	$2.398 \times 10^{-4}$	$4.826 \times 10^{-5}$	$1.741 \times 10^{-4}$	0.7260
1500	0.1990	1234	0.09599	$3.908 \times 10^{-4}$	$5.817 \times 10^{-5}$	$2.922 \times 10^{-4}$	0.7478
2000	0.1553	1264	0.11113	$5.664 \times 10^{-4}$	$6.630 \times 10^{-5}$	$4.270 \times 10^{-4}$	0.7539

Note: For ideal gases, the properties  $c_p$ ,  $k$ ,  $\mu$ , and Pr are independent of pressure. The properties  $\rho$ ,  $\nu$ , and  $\alpha$  at a pressure  $P$  (in atm) other than 1 atm are determined by multiplying the values of  $\rho$  at the given temperature by  $P$  and by dividing  $\nu$  and  $\alpha$  by  $P$ .

Source: Data generated from the EES software developed by S. A. Klein and F. L. Alvarado. Original sources: Keenan, Chao, Keyes, Gas Tables, Wiley, 1984; and Thermophysical Properties of Matter, Vol. 3: Thermal Conductivity, Y. S. Touloukian, P. E. Liley, S. C. Saxena, Vol. 11: Viscosity, Y. S. Touloukian, S. C. Saxena, and P. Hestermans, IFI/Plenum, NY, 1970, ISBN 0-306067020-8.

## C.3 Conductivity of glass wool

84

**High-density glass wool**

	<b>Th.Conductivity</b>	<b>Th.Diffusivity</b>	<b>Spec.Heat</b>
<i>20°C, Kapton 9,719 mm</i>			
Measure 1	0,047	0,40	0,12
Measure 2	0,044	0,32	0,14
Measure 3	0,045	0,35	0,13
Measure 4	0,047	0,50	0,09
Mean value	<b>0,046</b>	<b>0,39</b>	<b>0,119</b>
C.O.V. (%)	<b>3,5</b>	<b>20,1</b>	<b>15,8</b>
<i>150°C, Mica 9,719 mm</i>			
Measure 1	0,085	0,68	0,12
Measure 2	0,077	0,36	0,21
Measure 3	0,076	0,36	0,21
Mean value	<b>0,079</b>	<b>0,47</b>	<b>0,184</b>
C.O.V. (%)	<b>5,9</b>	<b>40,0</b>	<b>28,1</b>
<i>200°C, Mica 9,719 mm</i>			
Measure 1	0,082	0,34	0,24
Measure 2	0,082	0,36	0,23
Measure 3	0,083	0,36	0,23
Mean value	<b>0,082</b>	<b>0,36</b>	<b>0,232</b>
C.O.V. (%)	<b>0,4</b>	<b>2,8</b>	<b>2,5</b>
<i>300°C, Mica 9,719 mm</i>			
Measure 1	0,10	0,50	0,20
Measure 2	0,10	0,55	0,18
Measure 3	0,10	0,70	0,15
Mean value	<b>0,100</b>	<b>0,58</b>	<b>0,175</b>
C.O.V. (%)	<b>1,9</b>	<b>17,4</b>	<b>14,8</b>
<i>500°C, Mica 9,719 mm</i>			
Measure 1	0,15	1,45	0,11
Measure 2	0,18	1,47	0,12
Measure 3	0,16	2,01	0,08
Mean value	<b>0,163</b>	<b>1,65</b>	<b>0,102</b>
C.O.V. (%)	<b>9,0</b>	<b>19,4</b>	<b>21,9</b>



## C.4 Conductivity of copper

Table 2.4.1. Thermal Conductivity Values for Copper Calculated from Eq. 1.1.3 at Selected Temperatures and RRR Values.

T (K)	$\lambda (\text{W}\cdot\text{m}^{-1}\cdot\text{K}^{-1})$				
	RRR = 30	RRR = 100	RRR = 300	RRR = 1000	RRR = 3000
1	46	156	471	1574	4726
2	91	312	942	3147	9434
3	137	468	1413	4710	14044
4	183	624	1880	6243	18380
5	228	779	2343	7715	22170
6	274	933	2796	9075	25084
7	319	1085	3232	10260	26834
8	365	1235	3642	11197	27328
9	409	1380	4015	11836	26756
10	454	1520	4343	12172	25496
12	541	1778	4844	12127	22264
14	624	2002	5144	11544	19150
16	703	2186	5267	10725	16398
18	777	2324	5231	9771	13924
20	843	2408	5054	8727	11683
25	960	2381	4215	6135	7271
30	999	2119	3245	4151	4573
35	970	1784	2436	2859	3028
40	900	1467	1841	2047	2122
45	814	1205	1423	1531	1568
50	731	1002	1135	1196	1216
60	597	740	799	824	832
70	513	601	634	647	651
80	465	526	549	557	560
90	437	485	502	508	510
100	421	461	475	480	482
150	396	419	426	429	430
200	391	407	413	414	415
250	388	401	405	407	407
300	386	397	400	401	402
400	383	391	393	394	394
500	379	385	387	388	388
600	374	379	381	381	381
700	368	372	374	374	374
800	362	365	367	367	367
900	356	359	360	360	360
1000	350	352	353	353	354
1100	344	347	347	348	348
1200	339	341	342	342	342
1300	335	337	337	338	338

## C.5 Matlab code

**Listing C.1:** Optimazation function that is repeated for every ring

```

1 close all
2 clear all
3 clc
4 format shortE
5
6 global Tgi;
7 global Tfi;
8 global De;
9 global W;
10 global result;
11 global error;
12 Tgi = 773;
13 Tfi = 283;
14 result = [];
15 error = [];
16 rings = 7;
17 W = 0.0447707/rings;
18 De = 0.04932 - (W*tand(15));
19
20 for i = 1:rings
21
22     disp(De)
23     %Minimize function
24     est = [Tgi-20, Tfi+1];
25     options = optimset('TolFun', 1e-1, 'MaxFunEvals', 50, '
        OutputFcn', @outfun);
26     z = fminsearch('ringIteration', est, options);
27     disp(z)
28
29     %Initialization next iteration
30     Tgi = z(1);
31     Tfi = z(2);
32     De = De - (2*0.0017137);
33
34 end

```

**Listing C.2:** Calculates the outgoing temperatures from one ring

```

1 function [y] = ringIteration(x)

```

```

2
3 global Tgi;
4 global Tfi;
5 global De;
6 global W;
7 global result;
8 global error;
9
10 Tgo = x(1);
11 Tfo = x(2);
12
13 %Design parameters exhaust
14 delta = 0.003;           % [m]
15 de = De-(2*delta);      % [m]
16
17 %Design parameters tube
18 Dt = 0.006;             % [m]
19 Xt = 0.0006;           % [m]
20 dt = Dt-(2*Xt);        % [m]
21
22 %Design parameters bond
23 b = dt;                 %Has to be chosen arbitrarily
24 Xb = dt/2;             %Has to be chosen arbitrarily
25
26 %Thermal conductivities of solids
27 ke = (0.1333+(0.1727*(((Tgi+Tfi)/2)-273)/1000)) - (0.04334*(((
    Tgi+Tfi)/2)-273)/1000)^2)...
28     +(0.0332*(((Tgi+Tfi)/2)-273)/1000)^3))*100;           % [W/
    mK]
29 KB = xlsread('Copper conductivity');
30 kb = interp1(KB(:,1),KB(:,2),(Tgi+Tfi)/2);                 % [W/mK]
31 kt = interp1(KB(:,1),KB(:,2),(Tgi+Tfi)/2);                 % [W/mK]
32
33 %Exhaust gas parameters
34 Vg = 1.66666667e-4;                                         % [m3/s] = 10 l/
    min
35 cpg = ((29.11) + (-0.1916e-2*Tgi) + (0.4003e-5*Tgi^2)...
    + (-0.8704e-9*Tgi^3))/(2.016e-3);                         % [J/kgK]
37 RHO = xlsread('Hydrogen density');
38 rhog = interp1(RHO(:,1),RHO(:,2),Tgi);                     % [kg/m3]
39

```

```

40 %Cooling fluid parameters
41 Vf = 5e-5;                                %[m3/s] = 3 l/
      min
42 cpf = ((-203.6060)+(1523.290*(Tfi/1000))+(-3196.413*(Tfi/1000)
      ^2)+(2474.455*(Tfi/1000)^3)...
43       +(3.855326/(Tfi/1000)^2))/18.01528e-3; %[J/kgK]
44 rhof = 999.8438 * ((1+(1.4639386*((Tfi-273)/100))+(-0.0155050*((
      Tfi-273)/100)^2)+...
45       (-0.0309777*((Tfi-273)/100)^3))/(1+(1.4572099*((Tfi-273)
      /100))...
46       +(0.0648931*((Tfi-273)/100)^2));    %[kg/m3]
47
48 %Convective heat transfer coefficients
49 hg = intConvExhaust(Vg, de, Tgi, cpg, rhog);
50 hf = intConvTube(Vf, dt, Tfi, cpf, rhof);
51
52 %Thermal resistances
53 Lc1 = pi*((De+de)/2);
54 rg = (1/(Lc1*W*hg))+(delta/(Lc1*W*ke));
55
56 Lc2 = ((De/2)+(Xb/2))*pi;
57 rb = Xb / (b*Lc2*kb);
58
59 Lc3 = ((De/2)+Xb+(Dt/2))*pi;
60 Amw = (Dt-dt) / log(Dt/dt);
61 rt = Xt / (pi*Amw*Lc3*kt);
62
63 rf = 1 / (pi*dt*Lc3*hf);
64
65 %Optimization objective
66 Tb1 = (Vg*rhog*cpg*(Tgi-Tgo)*(-rg*3))+((Tgi+Tgo)/2);
67 Tb2 = (Vf*rhof*cpf*(Tfo-Tfi)*(rb+rt+rf))+((Tfi+Tfo)/2);
68 result = [result; [x, Tb1, Tb2]];
69
70 y = abs(Tb1-Tb2);
71 if Tgo>Tgi || Tfo<Tfi
72     y = Inf;
73 end
74 error = [error; y];
75
76 end

```

**Listing C.3:** Convection coefficient of forced internal convection in the exhaust

```

1 function [h] = intConvExhaust(V,d,T, cpG, rhoG)
2
3 %Constants from Excel tables
4 MU = xlsread('Hydrogen viscosity');
5 mu = interp1(MU(:,1),MU(:,2),T);           %kg/ms
6 K = xlsread('Hydrogen conductivity');
7 k = interp1(K(:,1),K(:,2),T);           %W/mK
8
9 %Dimensionless numbers
10 Re = (4*rhoG*V)/(mu*d*pi);
11
12 if Re < 3000
13     h = (4.36*k)/d;
14 else
15     f = ((0.792*log(Re)) - 1.64) ^ (-2);
16     Pr = (mu*cpG)/k;
17     Nu = ((f/8)*Re*Pr) / (1.07+(12.7*(f/8)^0.5)*(Pr^(2/3)-1));
18
19     h = (Nu*k)/d;
20 end
21 end

```

**Listing C.4:** Convection coefficient of forced internal convection in the cooling channel

```

1 function [h] = intConvTube(V,d,T, cpf, rhoF)
2
3 %Dynamic viscosity temperature dependent formula
4 mu = ((280.68*(T/300)^(-1.9))+(511.45*(T/300)^(-7.7))+(61.131*(T
5     /300)^(-19.6))...
6     +(0.45903*(T/300)^(-40)))*1e-6;           %kg/ms
7
8 %Thermal conductivity temperature dependent formula
9 k = (0.80201*(T/300)^(-0.32))+(-0.25992*(T/300)^(-5.7))
10     +(0.10024*(T/300)^(-12))...
11     +(-0.032005*(T/300)^(-15));           %W/mK
12
13 %Dimensionless numbers
14 Re = (4*rhoF*V)/(mu*d*pi);
15
16 if Re < 3000
17     h = (4.36*k)/d;

```

```

16 else
17     f = ((0.792*log(Re)) - 1.64) ^ (-2);
18     Pr = (mu*cpf)/k;
19     Nu = ((f/8)*Re*Pr) / (1.07+(12.7*(f/8)^0.5)*(Pr^(2/3)-1));
20
21     h = (Nu*k)/d;
22 end
23 end

```

**Listing C.5:** External natural convection on the outside of the insulation

```

1 function [h] = extConvIns(Tb,D,Ta)
2
3 %Properties of air @293K
4 rho = 1.204;           %kg/m3
5 mu = 1.825e-5;        %kg/ms
6 cp = 1007;            %J/kgK
7 k = 0.02514;          %W/mK
8 beta = 1/293;         %1/K
9
10 %Dimensionless numbers
11 Pr = (mu*cp)/k;
12 Gr = (9.81*beta*(Tb-Ta)*D^3) / ((mu/rho)^2);
13 Ra = Gr*Pr;
14 Nu = 0.6 + ((0.387*Ra^(1/6)) / ((1+(0.559/Pr)^(9/16))^(8/27)));
15
16 %Convective heat transfer coefficient
17 h = (Nu*k)/D;
18
19 end

```

**Listing C.6:** Plotting of the resulting graphs

```

1 function stop = outfun(x, optimValues, state)
2
3 global result;
4 global error;
5
6 stop = false;
7 hold on;
8
9 set(0, 'defaulttextinterpreter', 'Latex');
10

```

```
11 subplot(2,2,1)
12     plot(result(:,1))
13     grid on
14     grid minor
15     xlabel('Iterations [-]')
16     ylabel('$T_{go}$ [K]')
17     title('Temperature outgoing gas')
18 subplot(2,2,2)
19     plot(result(:,2))
20     grid on
21     grid minor
22     xlabel('Iterations [-]')
23     ylabel('$T_{fo}$ [K]')
24     title('Temperature outgoing fluid')
25 subplot(2,2,3)
26     plot(result(:,3))
27     hold on
28     plot(result(:,4))
29     grid on
30     grid minor
31     xlabel('Iterations [-]')
32     ylabel('$T_{b}$ [K]')
33     title('Temperature outside exhaust cone')
34 subplot(2,2,4)
35     plot(error)
36     grid on
37     grid minor
38     xlabel('Iterations [-]')
39     ylabel('Error [-]')
40     title('Convergence of the error')
41
42 drawnow
```





## Appendix D

# Bill of Material (BOM)

Part	Description	Quantity
Mechanical_Design_Backplate_reactor	Back-plate	1
Mechanical_Design_Conical_Duct	Conical duct	1
Mechanical_Design_Cylindrical_Duct_Pt2	Left hub	1
20x47x7 HMS5 V	Radial shaft seal	2
roulement_6204_2	Ball bearing	2
Mechanical_Design_Cylindrical_Duct_Pt1	Right hub	1
Mechanical_Design_Driven_Pipe	Driven pipe	1
WO.4118L.07S	Stepper motor	1
92290A330	M6 316 SS Flat-Head socket	4
93635A222	M6 316 SS Hex-Head	9
_Michaud_Chailly_A9_24_5M09_261411_1_2	Large pulley	1
michaud_chailly_A9_12_5M09	Small puley	1
Gearbox	PM42 IMS gearbox	1
Clogging_Mechanism_Mechanical_Design_Belt	HiTD 300-5M-9 belt	1
Mechanical_Design_Scraper	Scraper	1
94150A345	M6 316 SS Hex-Head nut	4
93395A196	M3 316 SS Flat-Head socket	2



N.V./S.A.

# Offerte

**NON-FERRO METALEN  
BEVESTIGINGSSYSTEMEN**

**METAUX NON-FERREUX  
SYSTEMES DE FIXATION**

Jacobsveldweg 12 - BE 2160 WOMMELGEM

Tel: 03/355.20.60 - Fax: 03/355.20.61 - E-mail: info@testas.be - HRA: 287.394 - BTW: BE 413.723.905

Uw Referentie: Mail Joppe Rutten  
Uw Klantnummer: 11547

Offertenummer: XJ/1022578  
5/03/2018

Facturatieadres

Leveradres

KU LEUVEN - FAKTURENBUREAU  
Krakenstraat 3  
BE 3000 LEUVEN

KU LEUVEN - FAKTURENBUREAU  
Krakenstraat 3  
BE 3000 LEUVEN

Wij danken U voor uw prijsaanvraag en bieden U als volgt aan:

E180481	Ronde Staaf Inox 316L ø90 WG IM 1 x 300mm	1 St	147€/St	in voorraad
F000110	Kosten voor het zagen INCL.	1 St	0€/St	
E180780	Ronde Staaf Inox 316L ø150 WG 1 x 30mm	1 St	75€/St	in voorraad
F000110	Kosten voor het zagen INCL.	1 St	0€/St	

Transportkosten: 15,00 €

Betaling: 30 dagen einde maand

Geldigheid van deze offerte: 48u, voor ongedeelde opdracht

Met vriendelijke groeten

Commercieel medewerker: Xavier Janssens

Uw contactpersoon binnendienst: Vincenzo Vollero



Afrikalaan 29A  
5232 BD 's-Hertogenbosch  
The Netherlands

Tel. +31 (0)85 4859 607  
Fax. +31 (0)85 0435 451

IBAN NL15RABO 0109 253 795  
VAT number NL 8207.74.029.B01  
Chamber of Commerce 17251872

info@lagertechnik.nl  
www.lagertechnik.nl

## Proforma Invoice

To  
KU Leuven  
Krakenstraat 3  
3000 LEUVEN  
BELGIE

Ship to  
KU Leuven  
Technologiecampus De Nayer  
lok 00.E002 Ophoff Ce'dric  
Jan De Nayerlaan 5  
2860 SINT-KATELIJNE-WAVER BELGIE"

Our order number : 10048589

Order date : 14-03-2018

Customer identity : 108545

Contact person : Bart Wuyts

Terms of delivery : UPS Standard

Your reference : 4501106093

Terms of payment : Pay in advance

Your VAT number : BE0419052173

Line	Code	Description	Quantity	Price	Discount	Line value
1	10012174	SKF Groefkogellager W 6204-2Z	2	53,06	0,00%	106,12
2	10016333	SKF oliekeerring CR 20X47X7 HMSA10 V (viton)	2	13,88	0,00%	27,76
3	10029814	SKF HiTD tandriem 300-5M-9	1	3,31	0,00%	3,31
4	10029001	SKF tandriemschijf 24-5M-09F ongeboord	1	3,97	0,00%	3,97
5	10028993	SKF tandriemschijf 12-5M-09F ongeboord	1	2,60	0,00%	2,60

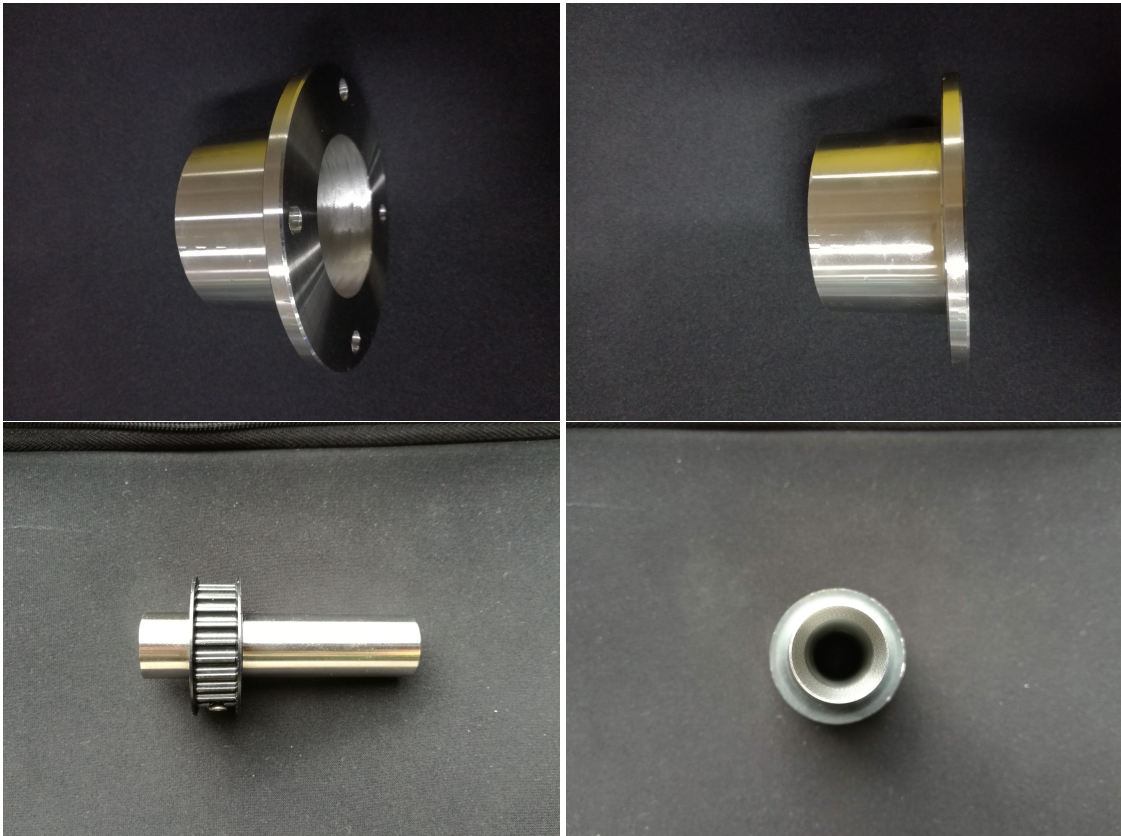
Order value	Order discount	Base of VAT	VAT %	VAT amount	Currency	Total amount
143,76		143,76	0,00%	VERLEGD	EUR	143,76



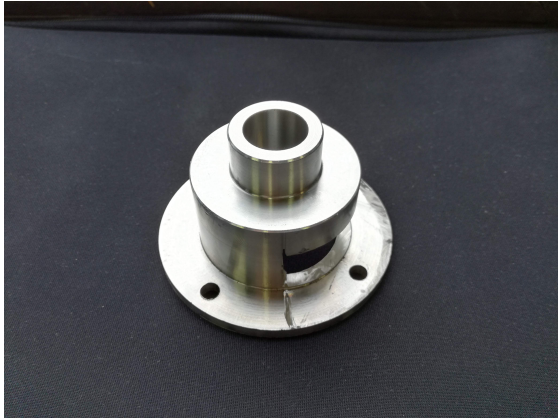
## Appendix E

# Manufacturing and assembly

### E.1 Manufacturing of the parts









## E.2 Assembly of the mechanism



FACULTY OF ENGINEERING TECHNOLOGY  
DE NAYER (SINT-KATELIJNE-WAVER) CAMPUS  
Jan De Nayerlaan 5  
2860 SINT-KATELIJNE-WAVER, België  
tel. + 32 16 30 10 30  
fet.denayer@kuleuven.be  
[www.fet.kuleuven.be](http://www.fet.kuleuven.be)

